Large Eddy Simulation of a cavity with a synthetic stochastic thick turbulent inflow

University of Leicester

Manuele Monti

Department of Engineering

University of Leicester

A thesis submitted for the degree of

Doctor of Philosophy

2012

Large Eddy Simulation of a cavity with a synthetic stochastic thick turbulent inflow

Manuele Monti

Department of Engineering

University of Leicester

A thesis submitted for the degree of
Doctor of Philosophy

2012

The flow dynamics of a rectangular cavity with a thick incoming boundary layer at low Mach numbers is investigated by Large Eddy Simulation (LES) and parallel CFD, as a simplified model of automobile bodywork recesses.

The cavity inflow is generated by means of synthetic stochastic time-dependent methods in a precursor simulation, in order to identify and analyze quantitatively the streaks in the spatially developing boundary layer approaching the cavity.

In the cavity flow model, no self-sustained oscillation is found, due to the high value of the boundary layer thickness. The influence of the approaching boundary layer turbulent scales on the cavity instabilities is examined. The intermittent cavity flow behaviour is related to the injection and ejection of vortex structures across the cavity opening and downstream edge. The space and time resolution of the LES enables to identify the flow dynamics of vortical instabilities and of the three-dimensional structures in the cavity shear layer. Cavity noise sources are identified by correlation and spectral analysis. In the upstream region of the cavity, the streaks break down into smaller and less coherent structures, as shown by the reduction of the integral length scale. In the rearmost region of the cavity, a spanwise negative velocity correlation is interpreted as a dipole-type noise source, which is likely to reduce the radiated noise level with respect to a two-dimensional cavity flow. The velocity spectra show broadband amplification of modes related to the dominant scales in the cavity, as opposed to the selective mode amplification of cavities with a thin boundary layer inflow.

A novel multivariate non-dimensional analysis of the CFD parameters is presented, that explicits the modelling process for a cavity flow test case. This is used for estimating the simulation cost and the spatial and temporal resolution trade-off in the cavity flow simulation.

To Licia and to my parents.
Actually, to my family.

Acknowledgements

possible, I am even more thankful to them now, than I had been for my MSc thesis at the University Roma Tre.

These years, this experience abroad, my life, would not have been the same without Licia D'Amico. I am deeply grateful for her support and (nearly always) patience. She has been the motivation to complete this work, the lifeline to overcome sleepless nights in front of the laptop. Many thanks to all my family. Tiziana, Carlo, Maurizio, Nicolò, Holly. They are the everlasting picture of serenity in my mind.

Contents

List of Figures

List of Tables

Nomenclature

Roman characters

A Integration constant for the outer region velocity profile

B Logarithmic law constant

C Courant number

c Speed of sound

C_f Skin friction coefficient $C_f = \tau_w / 0.5 \rho U_\infty^2$

$Cost$ Simulation complexity

C_s Smagorinsky coefficent

D Cavity depth

d Distance from the nearest wall

DS Computational domain length

e Internal energy

e_0 Total energy

$\mathbf{F}$ Inviscid fluxes

f Characteristic frequency

$f = 0$ Function describing the integration surface

h Enthalpy

$H(f)$ Heavy-side function, $H(f) = 0$ for $f < 0$ and $H(f) = 1$ for $f \geq 0$

$\mathbf{I}$ Identity matrix

k Wavenumber

$\bar{k}$ Average turbulent kinetic energy

k_{max} Cut-off wave number

k_T thermal conductivity

L Cavity length

l_s Subgrid length scales

M Mach number

m Synthetic mode order

$\mathbf{n}$ Unit outward normal vector to $f = 0$

N_{RK} Runge-Kutta order

N_c Number of mesh points/cells

N_d Spectral width $N_d := k_{max}/k_{min}$

N_P Number of processors

p Pressure

p' Pressure fluctuation, $p' = p - p_\infty$

Pr Prandtl number

$\mathbf{q}$ Heat flux vector

Q Second invariant of the velocity gradient tensor $Q = -0.5\nabla\mathbf{U} : \nabla\mathbf{U}$

$\mathbf{q}_t$ Turbulent heat flux vector

r Ratio of successive gradients

Re Reynolds number, $Re = u_\infty L/\nu$

r_τ Average non-dimensional mesh spacing near walls

$\mathbf{S}$ Rate-of-strain tensor

s Entropy

S_P Speed-up on N_P processors

St Stroual number, $St = fL/u_\infty$

$\mathbf{t}$ Reynolds stress tensor

T Absolute temperature

T_0 Scalar operation time on single processor

$\mathbb{T}$ Lighthill stress tensor with component

T_P Parallel operation time on N_P processors

$\mathbf{U}$ Conservative variable vector

$\mathbf{u}$ Fluid velocity vector

$\mathbf{v}$ Source surface velocity vector

W Cavity span

Greek characters

β Sweby limiter parameter

$\delta(f)$ Dirac delta function

Δ Cut-off filter width

δ Boundary layer thickness

ϵ Mesh stretching ratio

η Outer layer non-dimensional coordinate, $\eta = y/\delta$

η_K Kolmogorov length scale

γ Specific heat ratio

Λ Integral length scale

λ Wavelength

ν Kinematic viscosity

$\mathbf{\Omega}$ Vorticity tensor, $\mathbf{\Omega} = 0.5(\nabla\mathbf{U} - (\nabla\mathbf{U}^T))$

ω Wave angular frequency

ϕ Flux limiter function, limiting the gradient ratio: $\phi(r)$

Π Wake parameter

ρ Density

ρ' Acoustic density fluctuation

τ Viscous stress tensor

θ Momentum thickness

Superscripts

$\bar{()}$ Time average

$\cdot$ Time derivative of

$+$ Inner layer scaling

$\prime$ Fluctuation about the time-mean value

T   Transpose operator

Subscripts

b Boundary cell or ghost cell

c cavity domain parameter

i Variable number

∞ Free stream condition

inl cavity inflow domain parameter

j Generic direction in space

out cavity outflow domain parameter

phy First interior cell

ret Quantity evaluated at retarded time

0 Stagnation condition

w Wall condition

x Observer reference system

y Source reference system

Other Symbols

$\frac{D}{Dt}$ Material derivative of, $\frac{D}{Dt} := \frac{\partial}{\partial t} + \mathbf{u} \cdot \nabla$

Δt Time step

δV Cell volume

δ_v Vorticity thickness

:   Tensor scalar product

$\otimes$ Dyadic product

μ_l Dynamic viscosity

μ_P Parallelization efficiency

μ_t Eddy viscosity

∇ Gradient operator

$\rho_{u'u'}$ Two-point spatial correlation function of the generic u' velocity fluctuations

R_{uu} Two-point auto-correlation function of the generic u velocity component

u^+ Normalized velocity, $u^+ = u/u_\tau$

u_τ Friction velocity, $u_\tau = \sqrt{\tau_{wall}/\rho}$

Acronyms

CFD   Computational Fluid Dynamics

DES   Detached Eddy Simulation

DNS   Direct Numerical Simulation

FT   Flow trough (time)

HPC   High Performance Computing

LDV   Laser Doppler Velocimentry

LES   Large Eddy Simulation

PDE   Partial Differential Equations

PIV   Particle Image Velocimetry

PPW   Point per wavelength

PSD   Power Spectral Density

RANS Reynolds Averaged Numerical Simulation

RDD   Recursive domain decomposition

SDD   Single domain decomposition

SFS   Sub-filter Scales

SGS   Sub-grid Scales

SMT   Simultaneous Multithrading

SPL   Sound Pressure Level

TDSS Time-Dependent Synthetic Stochastic

TVD   Total Variation Diminishing

WM-LES Wall modelled Large Eddy Simulation

WR-LES Wall resolved Large Eddy Simulation

Chapter 1

Introduction

1.1 Context

The development of Computational Fluid Dynamic algorithms for aeroacoustic applications has grown rapidly during the last two decades due to a rising interest in aerodynamic noise phenomena, driven by public demand for quieter vehicles and a more silent and comfortable travel experience (ICAO, 2005; UK Department for Transport, 2003). The industrial, aeronautical and automotive communities have shown a growing interest in simulating and controlling the noise generated by unsteady turbulent flows like cavity flows. While precision laser cutting and computer aided manufacturing (CAM) has improved the quality of the vehicle outer shell, some gaps in the surface are unavoidable, for instance, to allow the opening of doors and hatches. The flow unsteadiness past these gaps increases aerodynamic drag, structural vibration and cabin and airframe noise, leading to a reduced passenger comfort. Rectangular cavities with an approaching thick boundary layer have been used as a simplified geometry testcase to model the noise and drag from automobile bodywork recesses by FIAT. Cavity flows with a value $L/\theta < 80$ are defined as thick boundary layer cavities. Haigermoser (2009) studied by tomographic PIV a rectangular cavity to replicate the investigation of a real automobile cavity conducted by Ribaldone *et al.* (2005). In this configuration, at a typical highway cruise speed (140 Km/h), the cavity amplifies the energy modes throughout in the incoming boundary layer structure. The unsteady flow interaction with the cavity walls radiates noise to the far-field. Haigermoser (2009) showed that this mechanism differs from the traditional Rossiter instability mode, typical of cavities

with a thin inflow boundary layer, and requires resolving the eddies in the thick inflow inner sub-layer to capture their amplification across the cavity opening. A conventional Reynolds Averaged (RANS) approach to model the complex turbulent structures embedded in such a flow is not feasible, as the essential flow physics depends on resolving the inflow disturbances that generate noise by interaction with the cavity walls.

Unsteady Reynolds Averaged (URANS) approach requires the separation of energy length scales between the unresolved motion by URANS and the background of random noise modelled by the turbulence closure model. This approach was therefore not appropriate for this application, due to the absence of a spectral peak over a background of low energy in the spectra of a cavity with a thick boundary layer.

The turbulent scales can be resolved with a Large Eddy Simulation (LES) or a Direct Numerical Simulation (DNS) that can run only on High Performance Computing (HPC) platforms, given the stringent mesh requirements near the solid walls. From a computational point of view, one of the main challenges for CFD in HPC is to use efficiently the parallel architecture by accessing the CPU resources in an efficient way. To do so, an accurate forecast of the simulation computing costs and cluster load is required. Furthermore, a successful model of a cavity flow involves reproducing the flow physics with adequate accuracy, given the available computational resources. These two issues can be tackled simultaneously by sizing the CFD problem via dimensional analysis, separating the effects of the geometry of the enclosure, the boundary layer resolution, the turbulence model and the numerical scheme order of accuracy. This analysis, presented by the author in the body of the thesis, is a useful tool to obtain design trade-offs by a multivariate optimization in cavity flow CFD and for estimating the order of magnitude of the computational resources required by the simulations (Rona & Monti, 2011).

The generation of unsteady inflow data for spatially developing turbulent flows is another challenge that must be addressed to enable the application of LES to cavity flows with thick boundary layer. Since in LES the unsteady energy-carrying eddies are resolved, the velocity field specified at the inflow of the computation domain should represent the contribution from the turbulent structures embedded in the incoming boundary layer. Without this information at the inflow, turbulent eddies are generated from a condition that is either absent or incorrect, and the results of the predictions cannot be expected to be accurate.

1.2   Aims and objectives

Although a rectangular cavity geometry is fairly simple, the flow it generates hosts a broad range of fluid dynamic phenomena, like an unsteady shear layer developing from the leading edge, vortex shedding, re-circulation zones and the amplification of flow instabilities. The latter is particularly important for cavity flow with a thick incoming boundary layer, where the amplification of the boundary layer instabilities constitutes an important noise source. Haigermoser *et al.* (2008) investigated by PIV a rectangular cavity with a thick subsonic inflow boundary layer. The investigation shows the presence of discrete scales in the cavity, which alters the growth of the shear-layer that spans the cavity opening with respect to a classic equilibrium turbulence shear layer, implicit in a two-equation turbulence closure model. The shear layer growth rate influences the mechanisms of momentum transfer into and out of the cavity, which is important for cavity noise generation (Zhang *et al.*, 1998), as well as for convective heat transfer.

The main aim of this thesis is to investigate by CFD the dynamics of a length to depth ratio $L/D = 4$ cavity flow with a thick incoming boundary layer ($\delta/D \simeq 2.2$) at low mach numbers ($M \approx 0.126$). LES and time dependent inflow conditions (Pirozzoli *et al.*, 2008; Sandham *et al.*, 2003) are presented and the numerical model predictions are compared with experimental results from Haigermoser *et al.* (2008). LES enables the study of the full three-dimensional flow and of the dynamics of turbulent structures in space and time with a level of detail that is difficult to obtain with experimental techniques. In fact, conventional PIV is not sufficient to resolve in time the evolution of the cavity flow structures, mainly due to the relatively low acquisition rate of the conventional PIV measurements. Time-resolved PIV techniques are becoming available for acquiring in-plane velocity fields in the kHz range. A greater temporal resolution is offered by Laser Doppler Velocimetry (LDV), which is however limited to single-point measurement and requires phase averaging to generate space and time velocity maps. As the rectangular cavity flow instability and shear layer structures evolve both in space and time, numerical modelling by LES was selected as the most appropriate investigative approach for the unsteady flow past a rectangular cavity, in agreement with the simulation cost forecast provided by the multivariate dimensional analysis model.

The CFD work of this thesis aims to produce corroborative numerical evidence of the turbulent instabilities amplification mechanism for thick boundary layer cavity flows. To date, only experimental evidence has been published in literature by Haigermoser *et al.* (2008).

The objectives to pursue this final aim are:

1. To explicit the modelling process for a cavity flow test case through a multivariate dimensional analysis model of the CFD parameters (Rona & Monti, 2011). This model enables to estimate *a priori* the computational cost and the spatial and temporal resolution trade-off in cavity flow LES;

2. To set up an optimized LES rectangular cavity flow model to match the experiments of Haigermoser *et al.* (2008);

3. To optimize the efficiency of the MPI version of the CFD code low-order explicit scheme to tackle the cavity flow LES test-case;

4. To generate a time-resolved boundary layer inflow by means of synthetic-stochastic inflow techniques (Pirozzoli *et al.*, 2008; Sandham *et al.*, 2003), validating its mean and time dependent parameters, as well as the predicted flow physical features (streaks, structures correlation) against the literature;

5. To investigate the influence of the flow structures produced by the LES inflow generation techniques on the instabilities in the cavity enclosure;

6. To compare qualitatively the flow structures and validate the cavity flow mean velocity field and its statistics against the PIV experiments of Haigermoser *et al.* (2008; 2009);

7. Taking advantage of the 3D spatial and temporal resolution of the CFD simulations, to determine the growth rate of individual convected vortex structures over the shear layer, and to study their evolution and coherence;

8. To relate the resolved motion of individual vortex structures to cavity noise generation at the downstream cavity edge, by frequency analysis and correlation analysis.

The improved understanding of this flow mechanics is an important scientific output of significant potential impact for industry. Specifically, this research allows to identify and comprehend the range of fluid dynamics mechanisms that are ascribed for the noise generation. This offers the opportunity for reducing the time-scales of a typical industrial design by optimizing the vehicle bodywork cavities for low drag and low noise at the design stages for an enhanced passenger comfort.

1.3   Thesis outline

This thesis is divided into six chapters. The first chapter introduces the context, the aims and objectives of this work, and the expected outcomes. The first chapter also contains a literature review of cavity flow modelling, LES techniques, and time- dependent inflow boundary conditions for LES.

In Chapter 2 the methodology and the numerical techniques adopted are described and their parallel coding for modern HPC platforms is detailed. Chapter 3 presents the method for regressing the size and cost of cavity flow test cases. The method is then used in Chapter 5 to predict the computational cost of the cavity flow simulations. This method has enabled to make a formal numerical model design of the cavity flow simulations, which is an innovative contribution of this thesis. Chapter 4 concerns the spatially developing boundary layer test case that is used as a precursor simulation to provide the inlet flow for the time dependent LES cavity simulation. Chapter 5 presents the test case of a cavity with a thick inflow boundary layer. For both models the computational domain, the parallelisation performance, the numerical predictions and their comparison against the experimental work of Haigermoser (2009); Haigermoser *et al.* (2008) are presented. Chapter 6 reports the conclusions from this work, the scientific research achievements, the limitations of the work, and reports the open issues that could be addressed in future work.

1.4   Literature review

1.4.1   Cavity flows

Cavities are generally classified according to their streamwise length-to-depth ratio, L/D, and streamwise length-to-width ratio, L/W. A cavity is said to be deep if $L/D \ll 1$ and shallow if $L/D \gg 1$ (Rockwell & Naudascher, 1978), two-dimensional if $L/W \ll 1$ and three-dimensional if $L/W \gg 1$.

A cavity simulation not including the three-dimensional effect of the trailing vortices induced by the presence of the cavity side walls is referred as to a *pseudo-two dimensional* cavity flow simulation. This simulation is usually less computationally demanding than a *three-dimensional* cavity flow simulation, which requires grid refinement near the side walls of the cavity domain. A sketch of the *pseudo-two dimensional* cavity flow and the *three-dimensional* cavity flow spatial domains are shown in Figure 1.1(a) and Figure 1.1(b), respectively.

Cavity flows in which the shear layer spans across the entire cavity are "open " (Charwat *et al.*, 1961). An open cavity flow is characterized by a main re-circulation within the enclosure and one or two secondary re-circulations on the cavity floor. The flow separates at the cavity leading edge and reattaches at the trailing edge. In a closed cavity, the flow separates at the cavity leading edge and reattaches on the cavity floor. It then separates from the cavity floor further downstream and reattaches on the downstream wall. The upstream separation and reattachment points delimit an upstream region of flow re-circulation.

The high speed flow over an open cavity at certain inflow conditions produces complex unsteady interactions that generate an intense acoustic radiation. The flow approaching the cavity separates at the upstream edge, forming a shear layer, as shown in Figure 1.1. A typical turbulent free shear layer is visualized in Figure 1.2. The presence of the cavity walls influences the shear layer dynamics. The resulting flow comprises of both broadband small-scale fluctuations, typical of a turbulent shear layer, and discrete resonances, the frequency and amplitude of which depend upon the cavity geometry and the external flow conditions. The size range of the turbulent structures in the near-field region varies from the large-scale structures contained in the shear layer and within the unsteady re-circulating region inside a cavity to small-scale random
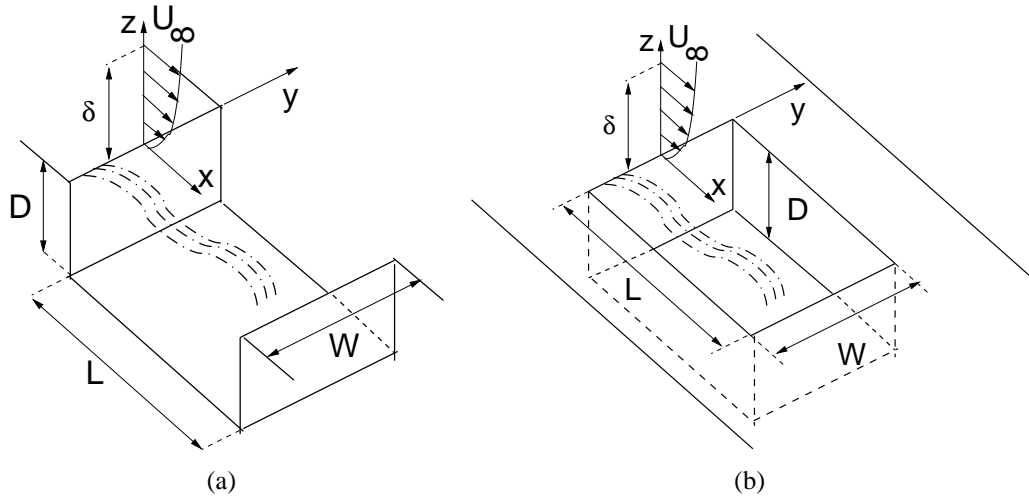
Figure 1.1: Sketch of a *pseudo-two dimensional* cavity (a) and *three dimensional* cavity (b).
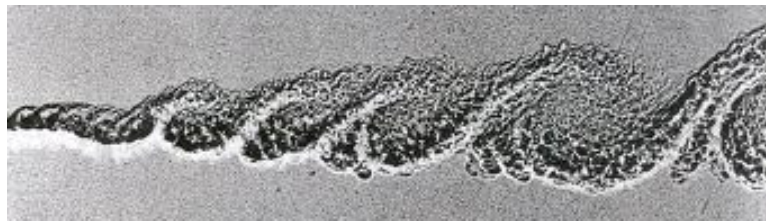
Figure 1.2: turbulent free shear layer visualization

fluctuations embedded in the approaching boundary layer (Murray & Ukeiley, 2004; Rossiter, 1964).

The development of turbulent modelling and simulation techniques for cavity flows has proven to be very valuable to gain an understanding of the generation of the main structures and of the main flow instability processes. Specifically, turbulence models enabled to investigate the effect of the small-scale random fluctuations on the onset, growth and saturation of the large-scale instabilities that often characterize a cavity flow. A comprehensive review of computational and experimental studies on cavity aerodynamics was conducted by Grace (2001). Several cavity flow predictions were obtained using RANS turbulence models in the past. RANS was used for its computational affordability and prediction accuracy in attached flow regions, but generally failed to capture in full the dynamics of the complex flow structures embedded in the

separated regions inside and above the enclosure. Techniques such as Direct Numerical Simulation (DNS) (Bres & Colonius, 2007; Gloerfelt *et al.*, 2002b; Hamed *et al.*, 2001; Moon *et al.*, 2003; Rowley *et al.*, 2002; Yao *et al.*, 2004) and Large Eddy Simulation (LES) (Chang *et al.*, 2006; Gloerfelt *et al.*, 2002a; Larchevêque *et al.*, 2004a,b, 2007; Rizzetta & Visbal, 2003; Suponitsky *et al.*, 2005) gave a more accurate representation of the complex flow in the separated region; however the main constraint, due to their high computational cost, is their limitation to low Reynolds number flows. DES have been widely used in cavity flow simulations to combine the good behaviour of RANS in the attached regions and LES in the separated regions (Arunajatesan & Sinha, 2001, 2003; Arunajatesan *et al.*, 2002; Basu *et al.*, 2005, 2006; Chang & Park, 2004; Hamed *et al.*, 2003, 2004; Shieh & Morris, 2001). Evidence of the sensitivity of the turbulence closure approach on the numerical results is given in literature by the works of Basu and Chang (Basu *et al.*, 2004, 2005, 2006; Chang & Park, 2004).

Colonius & Lele (2004) examined the more recent applications of LES and DNS to cavity flows and concluded that these techniques can give quality predictions of the time-averaged statistics, the pressure spectra, and the large-scale structures. A classification of the cavity modes based on the non-dimensional parameters was also proposed by Colonius (2001). At relatively high Mach numbers ($0.4 < M < 1.2$), the shear layer mode is driven by an acoustic feedback mechanism due to pressure oscillations generated from impinging vortical structures at the forward facing step. At lower Mach numbers, the flow oscillations are not driven by an acoustic feedback mechanism but by periodic oscillations, which are convected downstream the cavity shear layer and that cause periodic inflow into and outflow out from the cavity.

Colonius (2001) highlighted the importance of the inflow boundary layer thickness in determining the oscillating flow modes and mapped the variation of the dominant mode number with the thickness of the boundary layer at the cavity leading edge, defined by the ratio L/θ, where θ is the upstream boundary layer momentum thickness. Cavity flows with a value $L/\theta < 80$ are defined as thick boundary layer cavities and usually show the existence of peaks in the pressure spectra. Specifically, the value $L/\theta = 80$ was found to be a lower limit for cavity self-sustained oscillations to take place (Gharib & Roshko, 1987). In recent experiments of a cavity flow at low Mach number with a thick inflow boundary layer (Haigermoser *et al.*, 2008) was shown that the flow is highly intermittent, due to the presence of turbulent structures embedded

in the boundary layer, and mechanisms of regular self-sustained oscillations were not found, due to the high value of the vorticity thickness of the shear layer in the cavity opening. This experiment extended the understanding of the cavity flow physics to the case of relatively low values of L/θ at low Mach numbers and founds the basis for the numerical work of this thesis.

1.4.2   Large Eddy Simulations review

Turbulence closure models are used in CFD to obtain a reduced order model description of the fluid dynamics by windowing the wavenumber spectrum. DNS techniques resolve the full spectrum of the turbulent scales down the Kolmogorov length scale. This approach is extremely demanding in terms of time and computational capability and therefore it is not often available for common CFD applications. To overcome this limitation of DNS a coarser representation of the scales was introduced in form of LES.

The application of LES to a turbulent flow involves three separate steps (Ghosal & Moin, 1995). First, to obtain a coarser level description of the scales of motion, a spatial cut-off filter Δ is defined to remove the small scales. Sub-grid scales (SGS) are any scale that is smaller than the cut-off filter width Δ. The resulting equation that describes the space-time evolution of the large eddies contains the SGS tensor that accounts for the effect of the unresolved small scales on the resolved large scales. The second step is the replacement of the SGS tensor by a model. The final step is the numerical integration of the equations for the large scales on a numerical grid small enough to capture the dynamics of the large eddies but much larger than the Kolmogorov length scale. The process of sizing the numerical simulation is described in detail in Section 3.2.

The unresolved scales can be subdivided into two groups: the resolved sub-filter scales (SFS) and the sub-grid scales (SGS). The resolved sub-filter scales represent the scales with wavenumbers larger than the cut-off wavenumber k_{max}, but whose effects are dampened by the filter. Resolved sub-filter scales only exist when filters that are non-local in wave-space are used, such as a top hat or a Gaussian filter. These resolved sub-filter scales can be modelled using filter reconstruction. The numerical resolution of SFS is outside of the main objectives of this thesis.

Two classes of SGS models exist: the functional models and the structural models. The structural models aim at predicting the sub-grid scales directly, rather than recovering their effect on the resolved scales through the use of a forcing term. Functional models, also called Eddy-Viscosity models, are normally simpler than structural models, as they focus only on representing the SGS energy cascade by an artificial eddy viscosity approach. From a physical viewpoint, the effects of turbulent kinetic energy cascading to higher wavenumbers are lumped into an eddy viscosity term with a molecular-diffusion-like dissipation of the length scale kinetic energy. These models are easy to be implemented and able to predict the exact behaviour of the modelled quantities, but often fail in *a posteriori* tests to evaluate the models ability to accurately predict the interaction between the modelled and the resolved quantities.

Several SGS models have been developed for turbulence modelling since the first pioneering works by Smagorinsky (1963), and Deardorff (1970). The Smagorinsky-Lilly model (Smagorinsky, 1963) is the first SGS model developed and successfully applied to an LES simulation. It is a fully viscosity-based model in which the sub-grid scale viscosity μ_{sgs} is function of the rate-of-strain tensor S_{ij}, the density ρ, the filter width Δ, and a model closure coefficient that is constant in space and time, the Smagorinsky coefficient C_s. The main theoretical weakness of the Smagorinsky model is that it is purely dissipative: the energy flows only in one direction from resolved to sub-grid scales. This is also the major numerical strength, as it greatly enhances the numerical stability of the modelling procedure. On the other hand, the presence of the backscatter energy transport from sub-grid to resolved scales is neglected. Moreover, the Smagorinsky model requires *a priori* knowledge of the flow in order to define the coefficient C_s, which might not be valid for all parts of the flow in case of complex flow geometries.

The Wall-Adapting Local Eddy-viscosity (WALE) model by Nicoud & Ducros (1999) is another viscosity-based SGS model that introduces a near wall grading functions that acts as a turbulent kinetic energy limiter. In a preliminary assessment of the cavity inflow of the work of this thesis it was shown that, as long as the mesh is fine enough near the solid walls of the computational domain and the velocity profile is monotonic, then WALE and LES Smagorinsky models give similar results.

The Algebraic Dynamic model by Germano *et al.* (1991) is based on the Smagorinsky formulation of the sub-grid scale viscosity but allows the coefficient C_s to vary in

space and time. The local calculation of C_s is obtained at each time step by filtering the flow variables through a test filter and trying to determine the local value of the model constant at the grid filter. This technique overcomes the limitations of the purely viscosity based and Smagorinsky models at the expense of an increased computational cost. The modification of the dynamic model by Lilly (1992) derives the coefficient C_s from a least squares method, making the former version more stable.

A detailed overview of SGS models can be found in Sagaut (2002) and Wagner *et al.* (2007). Other popular SGS models are the model based on Re-normalization Group Theory developed by Yakhot *et al.* (1992), the Localized Dynamic model by Kim & Menon (1995), and the Dynamic Global-Coefficient model by You & Moin (2007).

1.4.3 Time-dependent inflow conditions for Large Eddy Simulations

The development of time dependent inflow conditions for spatially developing flow simulations is a stimulating CFD research field that has followed the application of DNS and LES to increasingly complex flows. A comprehensive review and comparison of the existing inflow condition for LES was published by Keating *et al.* (2004). Since DNS and LES techniques resolve the three-dimensional energy-carrying eddies, the specification of the inflow velocity should represent the statistical information of these structures, specifically, the first and second moments, the mode amplitude and the phase information between modes. Moments and mode amplitudes are relatively easy to be matched with stochastic methods, while phase information requires additional effort as this is strongly dependent on the particular type of flow that is modelled.

Early simulations of spatially developing turbulent flows used inflow conditions obtained as a modification of periodic conditions, by the addition of source terms to transform the governing equations into a self-similar coordinate frame (Spalart, 1988; Spalart & Watmuff, 1993). A more versatile approach was the recycling-rescaling method developed by Lund *et al.* (1998). This method is based on the similarity laws of an equilibrium turbulent boundary layer: the law of the wall in the inner part and the defect law in the outer part of the boundary layer. It provides an equilibrium turbulent boundary inflow of arbitrary thickness δ, wall shear stress ρu_τ^2 and free stream turbulence intensity. The method consists of extracting at each time-step from a recycling

station downstream of the inlet the inner and outer layer velocity profiles separately, and rescaling these profiles according the value of y^+ and y/δ, respectively, to match inflow target values of u_τ and δ. This provides a complete (inner, outer, logarithmic) profile at the inlet. Fluctuations are rescaled from the recycling station to produce target root-mean-square (rms) values at the inlet. The main limitation of this method is the introduction of "spurious "periodicity due to the non-physical initial condition of the flow that is recycled over a long transient. This often leads to a decreased inlet wall shear stress. Another limitation is that the method can apply only to an equilibrium boundary layer region that is not always available in complex flows. The recycling-rescaling method was initially tested for the generation of the time-dependent boundary layer cavity inflow but, as expected, it required a long transient to vanish the "spurious "periodicities. Moreover, it was found complex to control in time the values of the recycling station key parameters u_τ and C_f. This approach was therefore abandoned.

A modification of this method is to generate an inflow condition by running a separate precursor simulation of an equilibrium boundary layer flow by use of periodic boundary conditions and to store at each time step a surface normal plane of data to be used as inflow condition subsequently (Li *et al.*, 2000). This workaround enables the control of the integral momentum transport, leading to an improved wall shear stress at the computational cost of an extra simulation.

Another class of inflow generation methods is based on the generation of synthetic turbulence. The most basic technique to generate a turbulent inflow is taking a mean velocity profile with superimposed random fluctuations without any spatial or temporal correlations. The energy generated is also uniformly spread over all wavenumbers and the pseudo turbulence is quickly dissipated since the low wavenumbers do not contain the correct energy ratio. A contribution to the development of such techniques was initially brought by Le *et al.* (1997) who detected in the lack of phase information of the turbulent eddies a primary source of decaying turbulence. In the work by Batten *et al.* (2004), the turbulent eddies were synthesized by the superposition of sinusoidal modes with random frequencies and wavenumbers, with amplitudes fitting a prescribed inlet turbulent energy spectrum. In this approach, only low-order statistics were described, leading to a rapid decay of Reynolds stresses. In particular, the $\langle v'v' \rangle$ component is under-predicted and the simulation requires an inlet of considerable length so that the turbulence production has time to correct $\langle v'v' \rangle$ to levels more

representative of measured values in a turbulent boundary layer. To overcome this problem, Spille & Kaltenbach (2001) suggested adding a source term to the discretised governing equations at different control planes in the simulation domain, to reproduce a target Reynolds stress. Another contribution to the class of synthetic methods is the work by Jarrin *et al.* (2006), in which each eddy is represented by specific shape functions of position and time that describes its spatial and temporal characteristics. This method was able to reproduce specific first and second order one point statistics as well as auto-correlation functions of the velocity components.

Sandham *et al.* (2003) developed a variation of the synthetic turbulence inflow method for modelling the time-dependent inflow velocity in LES. The basic idea is to consider a mean turbulent boundary layer profile with synthetic fluctuations that mimic the organized motions in the inner and the outer parts of the boundary layer (lifted streaks and large eddies, respectively). This approach has been extensively tested in the literature, and shown to yield a fast transition to a fully developed turbulent state. Li & Coleman (2010) subsequently extended this method to supersonic flows. In order to break any remaining symmetry due to the deterministic specification of inlet disturbances, divergence-free random velocity fluctuations with prescribed mean and maximum amplitude have been added within the boundary layer, following the work of Pirozzoli *et al.* (2008).

A combination of the method of Sandham *et al.* (2003) with the improvement by Pirozzoli *et al.* (2008) was selected in this thesis to model the spatially developing time-dependent cavity inflow for its simplicity, robustness and elegance. Given the MPI structure of the CFD solver, it also improved the computation efficiency for providing at each time-step a full set of inflow information without requiring any additional running parameter from the inner computational domain, which should have introduced MPI time barriers.

Chapter 2

Numerical methods

2.1 Governing equations

2.1.1 Direct numerical simulation

A non-reactive adiabatic Newtonian flow under no external force is governed by the time-dependent Navier-Stokes equations:

$$\frac{\partial}{\partial t}\mathbf{U} + \nabla \cdot (\mathbf{F}_c + \mathbf{F}_v) = 0 \qquad (2.1)$$

where $\mathbf{U}$ is the conservative variable vector, $\mathbf{F}$ the inviscid flux vector, and $\mathbf{F}_v$ the viscous flux vector. These are defined as:

$$\mathbf{U} = \begin{pmatrix} \rho \\ \rho\mathbf{u} \\ \rho e_0 \end{pmatrix}, \quad \mathbf{F}_c = \begin{pmatrix} \rho\mathbf{u} \\ \rho\mathbf{u} \otimes \mathbf{u} + p\mathbf{I} \\ \rho\mathbf{u}\,(e_0 + p/\rho) \end{pmatrix}, \quad \mathbf{F}_v = \begin{pmatrix} 0 \\ -\tau \\ -\tau \cdot \mathbf{u} + \mathbf{q} \end{pmatrix} \qquad (2.2)$$

where $\mathbf{u}$ is the fluid velocity vector with Cartesian components u_i, e_0 is the total energy, e is the internal energy, p is the static pressure, ρ is the density, $h = e + p/\rho$ is the enthalpy, $\mathbf{q}$ is the conductive heat flux vector, τ is the viscous stress tensor, $\otimes$ is the dyadic product, and $\mathbf{I}$ is the identity matrix. In Equation (2.2), the rows relate to the conservation of mass, momentum, and energy, respectively.

The total energy e_0 is related to the fluid temperature T and velocity $\mathbf{u}$ by

$$e_0 = \frac{1}{\gamma - 1}RT + \frac{1}{2}\mathbf{u} \cdot \mathbf{u} \qquad (2.3)$$

R being the specific gas constant. In this work, air is assumed a perfect gas and temperature, pressure and density are related by the equation of state:

$$p = \rho RT \qquad (2.4)$$

The viscous stress tensor $\tau = \mu_l (\nabla\mathbf{u} + \mathbf{u} \otimes \nabla - 2/3\mathbf{I}\nabla \cdot \mathbf{u})$, where μ_l is the molecular viscosity. The conductive heat flux vector $\mathbf{q} = -k_T\nabla T$, where k_T is the thermal conductivity and T is the absolute temperature. If $\mathbf{F}_v = 0$, Equation (2.1) becomes the time-dependent inviscid Euler equations.

Auxiliary algebraic relations for the molecular viscosity and the thermal conductivity are introduced to solve the system of second-order partial differential equations (2.1):

$$\mu_l = 1.458 \times 10^{-6}\frac{T^{3/2}}{(T + 110.4)} \quad [\text{kg/ms}] \qquad (2.5)$$

$$k_T = \frac{\gamma R\mu_l}{(\gamma - 1)Pr_l} \quad [\text{W/mK}] \qquad (2.6)$$

where $\gamma = C_p/C_v$ is the specific heat ratio, $R = C_p - C_v$, and Pr_l is the Prandtl number.

2.1.2   Large Eddy Simulation

Direct numerical simulations (DNS) of high Reynolds number flows can be extremely demanding in terms of computational requirements. A complete cavity flow simulation cost analysis is presented in Chapter 3. Although modern HPC platforms and parallel computation algorithms enables to tackle challenging DNS of complex flows, the adoption of a turbulence closure model is still the most cost-effective choice for solving external flows in most industrial applications. To introduce a turbulence model, the time and space varying flow state variables of DNS $\mathbf{u}$ are split into two components, an averaged one $\overline{\mathbf{u}}$ and a fluctuating one $\mathbf{u}'$, so that

$$\mathbf{u} = \overline{\mathbf{u}} + \mathbf{u}' \qquad (2.7)$$

In LES, the average is obtained by the convolution of the continuous variable $\mathbf{u}(\mathbf{y}, t)$ with a time-invariant filtering kernel $\mathbf{G}(\mathbf{x}_i - \mathbf{y})$:

$$\overline{\mathbf{u}}(\mathbf{x}_i, t) = \int_{Vol} \mathbf{G}(\mathbf{x}_i - \mathbf{y}) \, \mathbf{u}(\mathbf{y}, t) \, \mathrm{d}\mathbf{y} \tag{2.8}$$

A sub-grid scale model (SGS) is then introduced to model the effects of the flow state fluctuation $\mathbf{u}'$ on the averaged flow. Usually, in CFD of industrial applications, the filtering kernel is matched to the computational grid. The Yoshizawa (1986) one-equation LES model assumes this match to resolve the large scales of motion. In such case, $\mathbf{G}$ is defined as the top-hat filter (Liu *et al.*, 2008) and is given by:

$$\mathbf{G}(\mathbf{x}_i - \mathbf{y}) = \frac{1}{\Delta_i} H\left(\frac{\Delta_i}{2} - |\mathbf{x}_i - \mathbf{y}|\right) \tag{2.9}$$

where H is the heavy-side function, Δ_i is the characteristic length of cell i, $\mathbf{x}_i$ is the cell centre position and $\mathbf{y}$ is the position vector. In the Yoshizawa one-equation LES model, Δ_i is the cubic root of the cell volume V_i, $\Delta = \sqrt[3]{V_i}$.

Applying the average in Equation (2.7) to Equations (2.1) gives the space averaged Navier-Stokes equations

$$\frac{\partial \overline{\rho}}{\partial t} + \nabla \cdot (\overline{\rho}\overline{\mathbf{u}}) \quad = 0 \tag{2.10}$$

$$\frac{\partial (\overline{\rho}\overline{\mathbf{u}})}{\partial t} + \nabla \cdot \left(\overline{\rho}\overline{\mathbf{u}} \otimes \overline{\mathbf{u}} + \overline{p}\mathbf{I} + \overline{\rho\mathbf{u}' \otimes \mathbf{u}'} - \overline{\tau}\right) \quad = 0 \tag{2.11}$$

$$\frac{\partial \left(\overline{\rho}\overline{e} + \frac{1}{2}\overline{\rho}\overline{\mathbf{u}' \cdot \mathbf{u}'}\right)}{\partial t} + \nabla \cdot \left(\overline{\rho}\overline{\mathbf{u}}\overline{h} + \frac{1}{2}\overline{\rho}\overline{\mathbf{u}}\overline{\mathbf{u}' \cdot \mathbf{u}'}\right) \quad =$$
$$\nabla \cdot \left[\overline{\mathbf{u}} \cdot \left(\overline{\tau} - \overline{\rho\mathbf{u}' \otimes \mathbf{u}'}\right) - k_T \nabla \overline{T} - \overline{\rho\mathbf{u}'h'}\right] \tag{2.12}$$

In Equation (2.12), $1/2\overline{\mathbf{u}' \cdot \mathbf{u}'}$ is the space averaged turbulent kinetic energy $\overline{k}$. In Equations (2.11) and (2.12), $\overline{\rho\mathbf{u}' \otimes \mathbf{u}'}$ is the Reynolds stress tensor, which is modelled by the Boussinesq approximation (Townsend, 1976) with analogy to viscous stress tensor as:

$$\overline{\mathbf{t}} = -\overline{\rho\mathbf{u}' \otimes \mathbf{u}'} = \mu_t \left(\nabla \overline{\mathbf{u}} + \overline{\mathbf{u}} \otimes \nabla - \frac{2}{3}\mathbf{I}\nabla \cdot \overline{\mathbf{u}}\right) - \frac{2}{3}\mathbf{I}\overline{\rho}\overline{k} \tag{2.13}$$

In Equation (2.12), $\overline{\rho\mathbf{u}'h'}$ is the turbulent transport of heat flux vector and it is modelled

to be proportional to the temperature gradient (Wilcox, 2002):

$$\bar{\mathbf{q}}_t = \overline{\rho \mathbf{u}' h'} = -\frac{\mu_t C_p}{Pr_t} \nabla \bar{T} \tag{2.14}$$

where Pr_t is the turbulent Prandtl number. To close the system of equations (2.10)-(2.12), an additional equation is required to relate the extra variable $\bar{k}$ to the other averaged variables. The derivation for $\bar{k}$ is obtained from the scalar product of the Navier-Stokes conservation of momentum vector equations multiplied by the fluctuating velocity vector $\mathbf{u}'$. Averaging this product by Equation (2.8), the transport equation for $\bar{k}$ is:

$$\frac{\partial \left(\bar{\rho} \bar{k} \right)}{\partial t} + \nabla \cdot \left(\bar{\rho} \bar{\mathbf{u}} \bar{k} - \overline{\mathbf{t} \cdot \mathbf{u}'} + \frac{1}{2} \overline{\rho \mathbf{u}' \mathbf{u}' \cdot \mathbf{u}'} + \overline{p' \mathbf{u}'} \right) \quad = $$
$$-\overline{\rho \mathbf{u}' \cdot \mathbf{u}'} \nabla \cdot \bar{\mathbf{u}} - \overline{\mathbf{t} : \mathbf{u}' \otimes \nabla} - \overline{\mathbf{u}' \cdot \nabla p'} + \overline{p' \nabla \cdot \mathbf{u}'} \tag{2.15}$$

Dahlström & Davidson (2003) proposed a one-equation SGS model for Equation (2.15), which is applicable to incompressible flows ($\nabla \cdot \bar{\mathbf{u}} = 0$):

$$\frac{\mathrm{D} \left(\bar{\rho} \bar{k}_{SGS} \right)}{\mathrm{D}t} = \bar{\mathbf{t}} : \bar{\mathbf{u}} \otimes \nabla - C_d \frac{\bar{\rho} \bar{k}_{SGS}^{3/2}}{\Delta} + \nabla \cdot \left[\left(\mu_l + \sigma_k \mu_{t,LES} \right) \nabla \bar{k}_{SGS} \right] \tag{2.16}$$

where $\mathrm{D}/\mathrm{D}t$ is the material operator $\mathrm{D}/\mathrm{D}t = \partial/\partial t + \bar{\mathbf{u}} \cdot \nabla$ and $\bar{\mathbf{t}}$ is the turbulent stress tensor, given by:

$$\bar{\mathbf{t}} = \mu_{t,LES} \left(\nabla \bar{\mathbf{u}} + \bar{\mathbf{u}} \otimes \nabla - \frac{2}{3} \mathbf{I} \nabla \cdot \bar{\mathbf{u}} \right) - \frac{2}{3} \bar{\rho} \bar{k}_{SGS} \mathbf{I} \tag{2.17}$$

The eddy viscosity $\mu_{t,LES}$ is given by:

$$\mu_{t,LES} = \bar{\rho} l_{sgs} \sqrt{\bar{k}_{SGS}} \tag{2.18}$$

where the sub-grid length scales l_{sgs} accounts for the modelled part of the total Reynolds stress tensor.

In the standard Smagorinsky SGS model, the sub-grid scale viscosity is defined as:

$$\mu_{t,LES} = \rho l_{smag}^2 \sqrt{2 \mathbf{S} : \mathbf{S}} \tag{2.19}$$

where the Smagorinsky lengthscale is $l_{smag} = C_{smag}\Delta$, C_{smag} is a model constant, the strain rate tensor $\mathbf{S}_{ij} = 1/2\,(\nabla\bar{\mathbf{u}} + \bar{\mathbf{u}} \otimes \nabla)$ and : is the double scalar product. In the numerical scheme of this work, a limiter is introduced to model the constraint in l_{smag} due to the presence of a solid wall:

$$l_s = \min\left(C_{smag}\Delta, \kappa y\right) \tag{2.20}$$

where $\kappa = 0.41$ is the Von Kármán constant. This can be interpreted as performing a similar operation to van Driest damping which reduces the length scale to zero near to the wall (McMullan & Page, 2011).

In Equations (2.16), (2.20) and (2.18), C_s and C_d are the Yoshizawa constants and are related to the Smagorinsky constant by:

$$C_{smag} = \left(\frac{C_s^3}{C_d}\right)^{0.25} \tag{2.21}$$

The Smagorinsky constant typically ranges from 0.065 to 0.2 and in this work $C_{smag} = 0.02$. The corresponding Yoshizawa constants used in this model are $C_s = 0.008$, $C_d = 1.05$, and $\sigma_k = 1.0$. The low value of the C_{smag} in this work was used to stop over-damping and to reduce the re-laminarization of the flow in the cavity boundary layer inflow. This value effectively makes the simulation close to an Implicit Large Eddy (ILES).

Equations (2.10), (2.11), (2.12) and (2.16) can be rearranged in the compact form:

$$\frac{\partial}{\partial t}\mathbf{U} + \nabla \cdot (\mathbf{F}_c + \mathbf{F}_v) + \mathbf{S} = 0 \tag{2.22}$$

where the conservative variable vector $\mathbf{U}$, the convective flux vector $\mathbf{F}_c$, the turbulent flux vector $\mathbf{F}_v$ and the turbulent source term vector $\mathbf{S}$ are given by Chen-Chuan Fan (2002) as:

$$\mathbf{U} = \begin{pmatrix} \bar{\rho} \\ \bar{\rho}\bar{\mathbf{u}} \\ \bar{\rho}\left(\bar{e} + \bar{k}\right) \\ \bar{\rho}\bar{k} \end{pmatrix} \tag{2.23}$$

$$\mathbf{F}_c = \begin{pmatrix} \bar{\rho}\bar{\mathbf{u}} \\ \bar{\rho}\bar{\mathbf{u}} \otimes \bar{\mathbf{u}} + \bar{p}\mathbf{I} \\ \bar{\rho}\bar{\mathbf{u}}\left(\bar{e} + \bar{p}/\bar{\rho} + \bar{k}\right) \\ \bar{\rho}\bar{\mathbf{u}}\bar{k} \end{pmatrix} \tag{2.24}$$

$$\mathbf{F}_v = \begin{pmatrix} 0 \\ -\left(\bar{\mathbf{t}} + \bar{\tau}\right) \\ +\bar{\mathbf{q}} + \bar{\mathbf{q}}_t - \left(\bar{\mathbf{t}} + \bar{\tau}\right) \cdot \bar{\mathbf{u}} - \left(\mu_l + \sigma_k\mu_t\right)\nabla\bar{k} \\ -\left(\mu_l + \sigma_k\mu_{t,LES}\right)\nabla\bar{k} \end{pmatrix} \tag{2.25}$$

$$\mathbf{S} = \begin{pmatrix} 0 \\ \mathbf{0} \\ 0 \\ C_d\bar{\rho}\bar{k}^{3/2}/\Delta - \bar{\mathbf{t}} : \nabla\bar{\mathbf{u}} \end{pmatrix} \tag{2.26}$$

2.2   Spatial discretization

In a structured finite volume discretisation, the physical domain is mapped to an assembly of topologically rectangular control volumes V_i, where subscript i indicates the ith control volume in the non-uniform mesh.

Integrating Equation (2.22) over each control volume V_i gives

$$\int_{V_i}\frac{\partial\mathbf{U}}{\partial t}\mathrm{d}V + \int_{V_i}\nabla\cdot\left(\mathbf{F}_c + \mathbf{F}_v\right)\mathrm{d}V + \int_{V_i}\mathbf{S}\mathrm{d}V = 0 \tag{2.27}$$

Assuming a stationary of computational domain and applying the Gauss divergence theorem, Equation (2.27) can be re-written as:

$$\frac{\partial}{\partial t} \int_{V_i} \mathbf{U} dV + \oint_{S_i} \mathbf{F}_c \cdot \mathbf{n} dS + \oint_{S_i} \mathbf{F}_v \cdot \mathbf{n} dS = 0 \tag{2.28}$$

where S_i is the closed boundary of V_i and $\mathbf{n}$ its inwards normal. Let

$$\mathbf{U}_i = \frac{1}{V_i} \int_{V_i} \mathbf{U} dV \tag{2.29}$$

$$\oint_{S_i} \mathbf{F}_c \cdot \mathbf{n} dS = \sum_{k=1}^{N_{faces}} \mathbf{F}_{c,k} \cdot \mathbf{n}_{i,k} S_{i,k} \tag{2.30}$$

$$\oint_{S_i} \mathbf{F}_v \cdot \mathbf{n} dS = \sum_{k=1}^{N_{faces}} \mathbf{F}_{v,k} \cdot \mathbf{n}_{i,k} S_{i,k} \tag{2.31}$$

$$\mathbf{S}_i = \frac{1}{V_i} \int_{V_i} \mathbf{S} dV \tag{2.32}$$

where N_{faces} is the number of faces of the control volume V_i, $S_{i,k}$ is the kth face of V_i and $\mathbf{n}_{i,k}$ is its inwards normal. Equation (2.28) can be written in a compact form as:

$$V_i \frac{\partial \mathbf{U}_i}{\partial t} + \mathbb{R}_i = 0 \tag{2.33}$$

where $\mathbf{U}_i$ is the space-averaged value of the conservative variable vector over the cell volume V_i and $\mathbb{R}_i$ is the residual generated from the discretised terms and it is equal to the sum of three terms:

$$\mathbb{R}_i = \sum_{k=1}^{N_{faces}} \mathbf{F}_{c,k} \cdot \mathbf{n}_{i,k} S_{i,k} + \sum_{k=1}^{N_{faces}} \mathbf{F}_{v,k} \cdot \mathbf{n}_{i,k} S_{i,k} + V_i \mathbf{S}_i \tag{2.34}$$

To solve the system of non-linear equations (2.33), the residual operator $\mathbb{R}_i$ in Equation (2.34) needs a linearised flux vector $\mathbf{F}_c$. Using the Godunov method, or Flux Difference Splitting, interface fluxes normal to the finite-volume unit cell boundaries are estimated by an approximate Riemann solver based on Roe (1981). The Roe approximate Riemann solver is first-order accurate in space, since the solution is projected on each cell as a piecewise constant state (Hirsch, 1988). To reduce the excessive artificial dissipation of the first order method, Van Leer *et al.* (1987) replaced the piecewise con-

stant state assumption with a quadratic reconstruction, leading to a higher order spatial reconstruction, the Monotone Upwind Scheme for Conservation Laws (MUSCL) interpolation. Following Manna (1992), the coefficients in the reconstruction are chosen to give a third-order accurate reconstruction of the spatial gradients in regions of smooth flow. This reconstruction uses four contiguous cells in the direction of the reconstruction, thus to connect two computational blocks at least two layers of ghost cells are required to make the flow solver block independent.

A flux limiter is then introduced to achieve a monotonic behaviour in regions of model flow discontinuities. Considering the ratio of successive gradients on the solution mesh

$$r_i = \frac{u_i - u_{i-1}}{u_{i+1} - u_i} \tag{2.35}$$

Sweby (1984) proved that to achieve a numerically stable scheme, this needs to be Total Variation Diminishing (TVD) and the flux limiter function ϕ_r must respect the following conditions:

$$\phi(r) = 0 \qquad\qquad \forall \quad r \leq 0 \tag{2.36}$$

$$r \leq \phi(r) \leq \min[1, 2r] \qquad \forall \quad 0 < r \leq 1 \tag{2.37}$$

$$1 \leq \phi(r) \leq \min[2, r] \qquad \forall \quad r > 1 \tag{2.38}$$

This means that the limiting function must be designed such that it passes through a certain region of the $\phi(r)$ versus r plane, known as the TVD region which, for second-order TVD schemes, is shown in the Sweby (1984)'s diagram reproduced in Figure 2.1. Different limiters have been tested in this work to compare their oscillatory behaviour and eventually select the best limiter to resolve the large scale cavity flow motion in the LES simulation. These are the SuperBee and MinMod limiters by Roe (1986), Equations (2.39) and (2.40), and the Sweby (1984) limiter of Equation (2.41):

$$\phi_{sb}(r) = \max\left[0, \min\left(2r, 1\right), \min\left(r, 2\right)\right]; \quad \lim_{r \to \infty} \phi_{sb}(r) = 2 \tag{2.39}$$

$$\phi_{mm}(r) = \max\left[0, \min\left(1, r\right)\right]; \quad \lim_{r \to \infty} \phi_{mm}(r) = 1 \tag{2.40}$$

$$\phi_{sw}(r) = \max\left[0, \min\left(\beta r, 1\right), \min\left(r, \beta\right)\right], \quad (1 \leq \beta \leq 2); \quad \lim_{r \to \infty} \phi_{sw}(r) = \beta \tag{2.41}$$
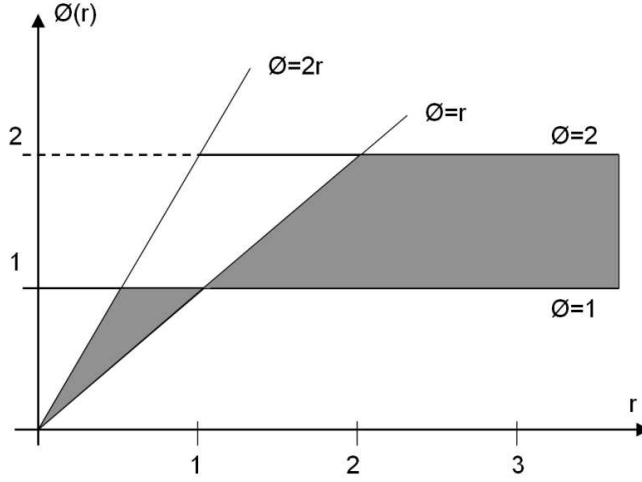
Figure 2.1: Region of stable operation of a second-order TVD scheme, from Sweby (1984).

All the above limiters exhibit the symmetry property

$$\frac{\phi(r)}{r} = \phi\left(\frac{1}{r}\right) \tag{2.42}$$

that ensures that the limiting actions for forward and backward gradients operate in the same way. Equations from (2.39) to (2.41) are plotted in Figure 2.2. For sake of clarity, two curves with different Sweby limiter coefficients are plotted, with $\beta = 1.3$ and $\beta = 1.6$.

Further details of the implementation of these limiter functions in the CFD scheme used are given in El-Dosoky (2009).

At the computational domain boundaries, a frame of one ghost cell deep is used to preserve the second-order accurate reconstruction in the domain interior.

To discretize the viscous fluxes, an estimate of the velocity vector gradients is required. For computing this, a staggered grid is built across the cell interfaces where these gradients are estimated. The flow state at the surface boundary of the new control volume and the surface boundary unit normal vector are obtained from the mesh geometry and then the velocity vector gradient is estimated using the Gauss divergence theorem. This gives up to a second-order accurate reconstruction of the velocity gradients (Manna, 1992).
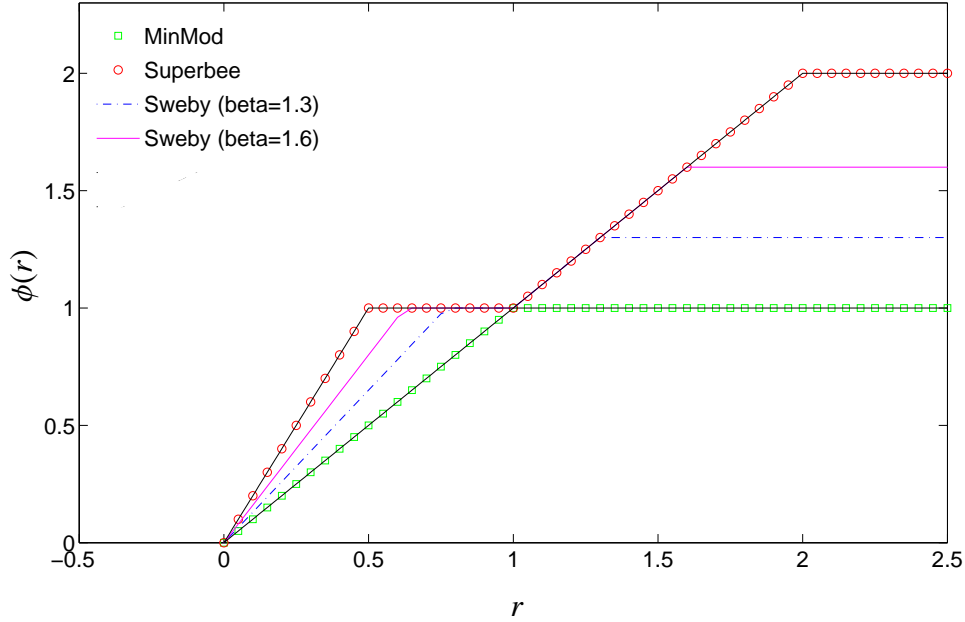
Figure 2.2: Limiter functions MinMod, Superbee, and Sweby ($\beta = 1.3$ and $\beta = 1.6$). For all limiters $\phi(r < 0) = 0$ and $\phi(r > 2) = \phi(r = 2)$

It is important to notice that the present model is driven by a mesh-based eddy viscosity μ_t related to the cell volume by the definition of **G** in Equation (2.9).

In the present thesis, the Sweby limiter was used for LES, as the right candidate, and the parameter β was selected by testing a range of preliminary wall-developing boundary layer simulations with $\beta = (1.05, 1.25, 1.3, 1.35, 1.6)$, among which the best results were obtained with $\beta = 1.3$. The parameter $\beta = 1.3$ is also used for the cavity flow model.

Among CFD practitioners it is a common practice to de-activate limiters to introduce enough dissipation so that the computational stability is dissipation controlled. Due to the upwind nature of the CFD scheme used in this thesis, this would have turn the scheme into an unstable finite-volume central scheme. In order to ensure a a stable behaviour of the CFD scheme, in this thesis limiters are alternatively working in place of the Smagorinsky constant to dissipate the correct amount of resolved turbulent kinetic energy.

2.3   Temporal integration

To solve the discrete ordinary differential vector Equation (2.33), an explicit multi-stage Runge-Kutta time step integration is used. This scheme is numerically cheap, requires a small computational memory and is designed to preserve the TVD properties of the spatial differentiation scheme. It is implemented as follows:

$$\mathbf{U}_i^0 = \mathbf{U}_i^n$$

$$\text{FOR } k = 1, RK$$

$$\mathbf{U}_i^k = \mathbf{U}_i^0 - \frac{\alpha_{RK}\Delta t}{V(RK-k+1)}\mathbb{R}^{k-1} \tag{2.43}$$

$$\text{END}$$

$$\mathbf{U}_i^{n+1} = \mathbf{U}_i^{RK}$$

where RK denotes the number of stages of the Runge-Kutta scheme and n the time level. The Runge-Kutta coefficients at the different stages of the integration are $\alpha_{RK} = 1$, $\alpha_{RK-1} = 0.5$, $\alpha_{RK-2} = 1/3$, and $\alpha_{RK-3} = 1/4$.

The stability of this scheme is restricted by the Courant, Friedrichs & Lewy (1928) condition which is $C = u\Delta t/\Delta x \leq C_{max}$ for an incompressible code, and $C = (u + c)\Delta t/\Delta x \leq C_{max}$ for a characteristic based code. In this thesis $C_{max} = 0.4$. The use of a pressure based code in this work could have brought a speed-up factor of about 10 with respect to using a characteristic based code.

2.4   Boundary conditions

The CFD scheme used is a multi-block solver that allows the computational domain to be divided into independent blocks. A schema of the computational domain for the LES cavity simulation, showing the first level multi-block decomposition is given in Figure 2.3.

Each block is fully rinded using ghost cells that are generated by mirroring the first interior cell at the boundary plane along the external boundaries. Along inter-block boundaries, the first and the second interior cell geometries of the abutting block define the ghost cell rind, that is two cells deep along an inter-block boundary. Boundary flow
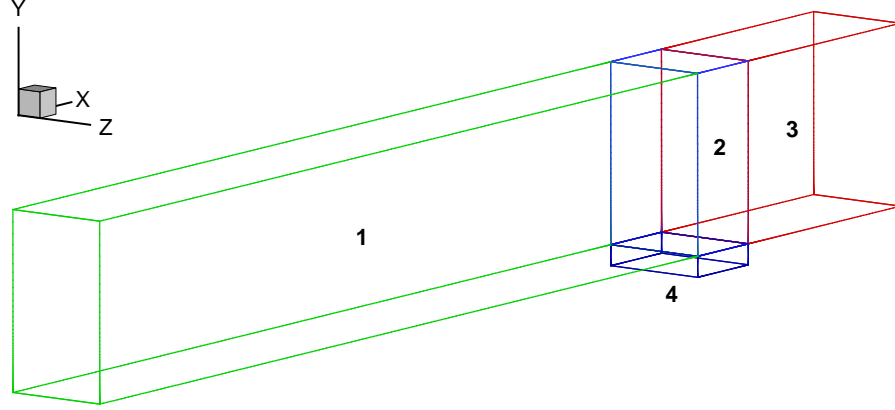
Figure 2.3: Independent blocks of the cavity model computational domain.

states are imposed in the ghost cells. The non-slip adiabatic condition is used for the solid walls of the domain, extrapolation from the inner cells is imposed at the outflow boundary, a non-reflecting condition is applied at the upper boundary, opposite to the flat plate wall, to minimize spurious reflections of disturbances, and periodic boundary conditions are used at the lateral boundaries in the spanwise direction of the domain. A formal description of these boundary conditions can be found in Grottadaurea (2009). A new Time-Dependent Synthetic-Stochastic (TDSS) inlet boundary condition is used in this work, which is novel in the context of cavity flow simulations. This method is based on the original work by Sandham *et al.* (2003), subsequently extended to supersonic flow by Li & Coleman (2010).

In this approach, the organized motions of the inner and outer part of the inflow boundary layer (lifted streaks and large eddies, respectively) are modelled by synthetic modes that are superimposed as velocity fluctuations on a mean turbulent boundary layer velocity profile. The choice of this approach against other conventional synthetic methods is justified in Section 1.4.3. The mean velocity profile, in terms of normalized streamwise velocity $u^+ = u/u_\tau$ is the one derived by Rona & Monti (2012)

$$u^+ = \frac{1}{\kappa} \ln y^+ + B + \frac{1}{k}\eta^2 (1 - \eta) + 2\frac{\Pi}{\kappa}\eta^2 (3 - 2\eta) \tag{2.44}$$

where $y^+ = yu_\tau/\nu_l$ is the inner scaling non-dimensional wall-normal distance, $\eta = y/\delta$

is the outer scaling non-dimensional wall-normal distance, $\kappa = 0.41$ the von Kármán constant, $B = 5.0$ the logarithmic law constant and the wake parameter is determined by Coles (1956) as:

$$\Pi = \kappa/2 \left(u_\infty^+ - \kappa^{-1} \ln Re_\tau - B \right) \tag{2.45}$$

The derivation of Equation (2.44) is detailed in Appendix A. A comparison of the analytical velocity profile from Equation (2.44) with profiles obtained by the successive complementary expansion method from Cousteix & Mauss (2007) is also presented in Rona & Monti (2012) for zero, low and moderate adverse pressure gradients. Velocity fluctuations about the mean velocity profile are obtained in space and time by superimposing five synthetic modes m according to

$$\left.\begin{aligned}
\tilde{u}(x,y,z,t) &= \sqrt{\rho_w/\bar{\rho}(y)}\; u_\infty \sum_{m=1}^{5} a_m U_m(y)\; \sin[\omega_m\,(x/u_{c_m} - t)] \cos\left(2\pi\, z/\lambda_{z_m} + \phi_m\right) \\
\tilde{v}(x,y,z,t) &= \sqrt{\rho_w/\bar{\rho}(y)}\; u_\infty \sum_{m=1}^{5} b_m V_m(y) \sin[\omega_m\,(x/u_{c_m} - t)] \cos\left(2\pi\, z/\lambda_{z_m} + \phi_m\right)
\end{aligned}\right\} \tag{2.46}$$

where

$$U_m(y) = (y/\hat{y}_m)\; e^{-y/\hat{y}_m} \quad , \quad V_m(y) = (y/\hat{y}_m)^2\; e^{(-y/\hat{y}_m)^2}. \tag{2.47}$$

Each synthetic mode has a prescribed convection velocity u_{c_m}, angular frequency ω_m, spanwise wavelength λ_{z_m}, spanwise phase angle ϕ_m, and amplitudes (a_m, b_m) in the streamwise and wall-normal directions, respectively. The inner-layer disturbances of the first mode ($m = 1$) are relative to streaks and streamwise vortices with maximum amplitude at $y^+ = 12$, propagating at a speed $12u_\tau$, with spanwise spacing $\lambda_z^+ \approx 120$ and a streamwise wavelength $\lambda_x^+ \approx 500$. Outer-layer oscillations ($m = 2, ..., 5$) mimic large vortical structures moving with a convection velocity $0.9u_\infty$ and amplitudes (a_m, b_m) as to match the distribution of the Reynolds stresses found in canonical fully developed boundary layers (Sandham *et al.*, 2003). In order to break the symmetries deriving from the deterministic specification of the inlet fluctuations, divergence-free random

m	$\hat{y_m}$	a_m	b_m	ω_m	$u_{c\,m}$	$\lambda_{c\,m}$	$\phi_{c\,m}$
1	$12.0\delta_v$	1.2	-0.25	$0.12u_\tau/\delta_v$	$10u_\tau$	$120\delta_v$	0.0
2	$0.25\delta_0$	0.32	-0.06	$1.2u_\tau/\delta_0$	$0.9u_\infty$	$L_z/3$	0.1
3	$0.35\delta_0$	0.2	-0.05	$0.6u_\tau/\delta_0$	$0.9u_\infty$	$L_z/4$	0.2
4	$0.5\delta_0$	0.08	-0.04	$0.4u_\tau/\delta_0$	$0.9u_\infty$	$L_z/5$	0.3
5	$0.6\delta_0$	0.04	-0.03	$0.2u_\tau/\delta_0$	$0.9u_\infty$	$L_z/6$	0.4

Table 2.1: Synthetic inlet forcing parameters for Equation (2.46)

velocity noise with a maximum amplitude $u'_{rms}/u_\infty < 4\%$ is superimposed on the synthetic disturbances. The third velocity disturbance component in the spanwise direction is determined assuming that the synthetic fluctuation velocity field is solenoidal, i.e. $\nabla \cdot \tilde{\mathbf{u}} = 0$.

The prescribed values used for the synthetic inlet forcing are reported in Table 2.1. These values were obtained by an iterative modification of the amplitude values (a_m, b_m) from the original values of Bernardini (2008), in a preliminary set of cavity inflow simulations. Hence sensitivity analysis of the related boundary layer mean velociti profile values respect the analytical formulation by Musker (1979) enabled to select the best combination of (a_m, b_m) parameters. A comparison with the results obtained using the original values by Sandham *et al.* (2003) was also performed before defining the definitive parameters for the cavity inflow and cavity flow simulations of this work.

2.5   Parallelization strategy

High Performance Computing (HPC) has become increasingly used for running computationally demanding CFD simulations such as LES and DNS. Any medium ($\leq 20 \times 10^6$ cells) and large ($> 30 \times 10^6$ cells) CFD test case is currently intractable without an HPC facility.

Message Passing Interface (MPI) is a message passing library standard that is widely used for parallel computations. The CFD scheme described in this chapter has been recently recoded for MPI. In the present thesis, the MPI version of the solver was optimized for LES applications and tested on two distributed-memory HPC clusters.

The first cluster is the IBM-SP6 of the CINECA HPC centre in Bologna, Italy. This is a cluster dedicated to massive parallel applications and special High-End projects. It is a 168 Power6 with 575 compute nodes, each with 32 cores/node, for a total of 5376 cores and a peak performance of just over 100 Tflops. The second cluster used is the ALICE HPC cluster of the University of Leicester, Great Britain. It is made of 256 standard compute nodes, each with a pair of quad-core 2.67GHz Intel Xeon X5550 CPUs and 12GB of RAM, for a total of 2048 CPU cores.

In a Single Domain Decomposition (SDD), each zone of computational domain, given the number of processors available in the cluster, is sliced into blocks along a single direction k of the domain. This introduces a large memory consumption and interblock communication over-head, which makes the algorithm unsuitable for multi-block massive CFD.

The CFD solver used in this thesis uses a Recursive Domain Decomposition (RDD) parallelisation algorithm (Grottadaurea, 2009). The computational domain is built by an assembly of three-dimensional topologically orthogonal zones (i, j, k), similarly to SDD, and each zone is considered as an independent unit that is allocated to a selected group (or sub-cluster) of processors. Each unit is then sliced over k planes and thus distributed to each processor in this sub-cluster. By doing so, the memory allocation benefits from the sub-division of the computational domain in these units. Specifically, the sub-cluster communication runs independently from the communication between abutting zones.

The numerical integration is performed asynchronously on each sub-cluster of processors between updates of zone interface data. The I/O is performed from the master node. Further details on the algorithm, the optimization of the load balance, and description of the MPI communicators can be found in Grottadaurea (2009).

The RDD MPI algorithm was re-coded and optimized for the SSTD method and the specific geometry and mesh constraints of this work by the author. Alternative techniques were considered, such as MPI - Open MP hybrid algorithms which lends to less tuning and customization than the RDD MPI algorithm. These approach could be further investigated in a computational research framework for future works.

The parallelisation performance of the test cases for the wall-developing boundary layer inlet and the cavity flow is reported in Chapter 3.

Chapter 3

Numerical model design

3.1 Introduction

A successful model of a high Reynolds number cavity-flows involves reproducing the flow physics with adequate accuracy, given the available computational resources. Basu *et al.* (2006) studied the dependence of the simulation cost on the turbulence closure approach and on the spatial and temporal discretisation for a unique cavity-flow model, but this dependence has never been quantified parametrically for a broader class of unsteady cavity-flows with different geometrical characteristics and flow parameters. The process of planning high Reynolds number cavity-flow simulations is systematically reviewed to extract the dependence of different programmer's choice on the CFD mesh size and on the cost of the computation. This process has been broken down into five phases: i) description of the problem in the continuous domain, ii) problem order reduction by turbulence modelling, iii) discretisation in space and time, iv) integration of the governing equations, v) costing the numerical operations of the flow solver. This chapter examines the influence of each phase on the spectral width and the grid density that are the key CFD indicators that determine the cost of the computation. A dimensional analysis was conducted to separate the effects of the geometry of the enclosure, the boundary layer resolution, the turbulence model, and the numerical scheme order of accuracy. Regression analysis on the non-dimensional groups of published cavity CFD simulations determined the range of practical values used by current state-of-the-art computations. This analysis is a useful tool to obtain design trade-offs by a

multivariate optimization of cavity-flow CFD and for estimating the order of magnitude of the computational resources required by the simulations.

An extended explanation of this modelling process can be found in Rona & Monti (2011). This analysis is applied to obtain approximate *a priori* cost estimates and optimize the computational cost of the cavity-flow test case presented in Chapter 5.

3.2 Turbulent flow sizing

The process of modelling and discretising a turbulent flow is shown in the flow chart of Figure 3.1.
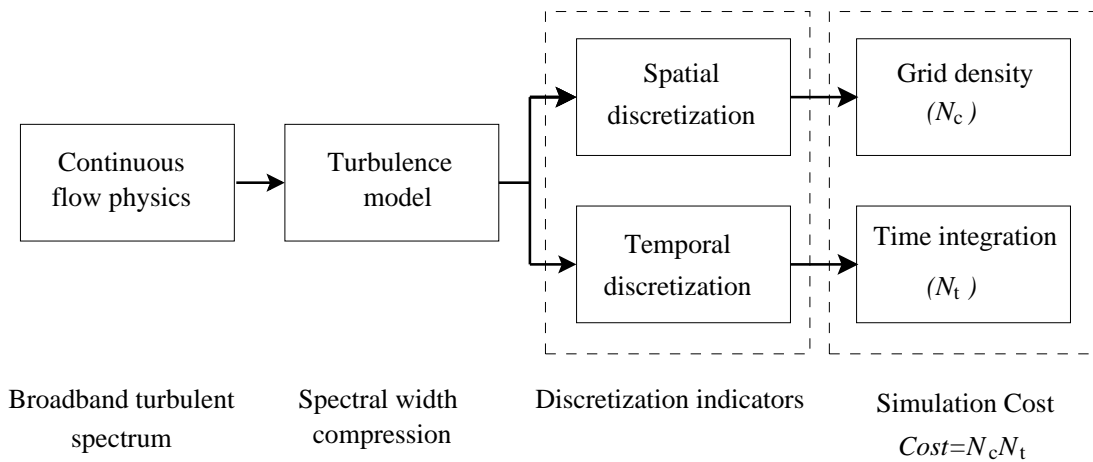
Figure 3.1: Modelling and discretisation process of a turbulent flow.

Consider a flow evolving in a physical flow domain of size L over a time interval T. The turbulence model represents the first element for reducing the dimensionality of the problem by considering only the time-space scales of interest in the flow (Sagaut, 2002). The time scales of the averaged problem are intrinsically related to the characteristic space scales. Therefore, an appropriate level of time resolution is required to represent the entire temporal evolution of the smallest pertinent scale of the averaged problem.

The discrete-spatial computational mesh introduces a further approximation to the flow model. The choice of the discretisation step Δx is reflected into two main indicators of the spatial discretisation in a generic j-direction: the spectral width of the simulation in

the wavenumber domain $N_{d,j}$, and the grid density, $N_{c,j}$. The spectral width $N_{d,j}$ gives the effective size range of turbulent structures of practical interest in the continuous flow in the j direction:

$$N_{d,j} := \frac{k_{j,\max}}{k_{j,\min}} = \frac{\lambda_{j,\max}}{\lambda_{j,\min}} \tag{3.1}$$

where $\lambda_{j,\max}$ and $\lambda_{j,\min}$ are respectively the wavelengths of the largest and smallest structures of interest in the flow, with corresponding wavenumbers $k_{j,\min}$ and $k_{j,\max}$. $N_{c,j}$ is the number of mesh points in j:

$$N_{c,j} = \frac{\lambda_{j,\max}}{\Delta x_{j,\min} \mathfrak{I}_j} \tag{3.2}$$

where $\Delta x_{j,\min}$ is the smallest unit cell length in j and $\mathfrak{I}_j (s_1(\xi_i), s_2(\xi_i), ..., s_n(\xi_i))$ is a functional that accounts for the different mesh stretching functions $s(\xi_i)$ adopted along j. Given the minimum number of points per wavelength (PPW) that the solver in the numerical scheme can work with, an average mesh spacing $\overline{\Delta x_j}$ for the first PPW points of a stretched mesh is $\overline{\Delta x_j} = PPW^{-1} \sum_{j=1}^{PPW} \Delta x_j$. From $\lambda_{j,\min} = \Delta x_{j,\min} PPW$ a uniform mesh equivalent $N_{c,j}$ is obtained

$$N_{d,j} = \frac{DS_j}{PPW \overline{\Delta x_j}} = \frac{N_{c,j}}{PPW} \tag{3.3}$$

where DS_j is the computational domain length in j. The derivation of Equation (3.3) is given in Appendix B.

The total number of mesh points N_c in a single block conformal computational domain is the product of the grid density in each direction:

$$N_c = \prod_j N_{c,j} \tag{3.4}$$

To integrate the unsteady equations of motion over a time proportional to the integral timescale of the motion, T, discrete-time integration methods are used that advance the solution N_t times over a number of time steps Δt. The time steps required to time march the equations of motion must be multiplied for the number of time step sub-iterations, such as in a multi-stage Runge-Kutta scheme (i.e. Runge-Kutta order, N_{RK}), to obtain the total number of iterations N_T used to time-advance a computation. The

total simulation cost (complexity) is measured by the product of the total number of mesh points and the number of discrete time steps:

$$Cost = N_c N_T = N_c N_t N_{RK} \tag{3.5}$$

where N_c is a function of the dynamic range of the simulation, which is measured by the Reynolds number, Re. The time step dimension is linked to the dimension of the smallest eddy via the Courant Friedrichs Lewy (CFL) condition, hence N_t can also be expressed as a function of Re to obtain

$$Cost = N_c\,(Re)\,N_t\,(Re)\,N_{RK} \tag{3.6}$$

where N_{RK} is taken as constant for a constant multi-step Runge-Kutta time integration scheme. This shows the strong dependence of the total cost of a CFD simulation on the Reynolds number.

In turbulent flow simulations of separated flows, the mesh resolution requirements for DNS are determined by $\Lambda/\eta_K \propto Re_\Lambda^{3/4}$, where η_K is the smallest dynamically active scale, the Kolmogorov length scale, and Λ is the characteristic length of the most energetic scale, the integral length scale. The total number of grid points N_c required to perform DNS of isotropic turbulence in a box of volume Λ^3 scales as $Re_\Lambda^{9/4}$. The minimum number of time steps is $T_\Lambda/T_\eta \propto Re_\Lambda^{1/2}$, hence the minimum complexity of the simulation is of the order of $Re_\Lambda^{9/4} Re_\Lambda^{1/2} \approx Re_\Lambda^3$.

Wall-bounded flows introduce more restrictive discretisation constraints (Piomelli & Balaras, 2002) as the relevant scales in the inner layer are of the order of the viscous length scale, $l_s = \nu/u_\tau$. The number of grid points in each direction scales as:

$$N_{c,j} = \frac{\Lambda}{\Delta x_j} = \frac{\Lambda}{\Delta x_j^+ \nu/u_\tau} \simeq \frac{\Lambda U_\infty Re_\Lambda^{-\alpha/2}}{\nu} \propto Re_\Lambda^{1-\alpha/2} \tag{3.7}$$

where α is the Reynolds number scaling of τ_w and $0.2 \leq \alpha \leq 0.25$ for a turbulent boundary layer (White, 1991) with free-stream velocity U_∞.

The proportionality factor in Equation (3.7) is given by the coefficient $1/\Delta x_j^+$, where Δx_j^+ is the mesh size in viscous wall units, typically between $1 - 5\,l_s$ in the wall-normal direction for WR-LES ($30 - 50\,l_s$ for WM-LES), and $100 - 300\,l_s$ elsewhere. The total

number of grid points N_c for a three-dimensional wall-bounded simulation is:

$$N_c \propto Re_\Lambda^{3(1-\alpha/2)} \approx Re_\Lambda^{2.7} \tag{3.8}$$

For DNS, the size of the time step Δt and the characteristic time of large events scale as $(\Lambda/u_\tau)\,Re_\Lambda^{-1/2}$ and Λ/U_∞, respectively. The estimated number of time steps is therefore of the order of $Re^{\alpha+1/2}$ and the overall computation cost from Equation (3.5) is:

$$Cost \propto Re_\Lambda^{3.5-\alpha/2}N_{RK} \simeq Re_\Lambda^{3.4}N_{RK} \tag{3.9}$$

For wall-resolved LES a constant spacing grid in the streamwise and spanwise direction must be used to resolve the inner-layer streaks. Taking $\Delta x^+ \simeq 100$ and $\Delta z^+ \simeq 20$ (Chapman, 1978), the number of points to resolve the viscous sub-layer is

$$N_c \propto C_f Re_\Lambda^2 \approx Re_\Lambda^{2-\alpha} \approx Re_\Lambda^{1.8} \tag{3.10}$$

where $C_f = \tau_w/0.5\rho U_\infty^2$.

From the CFL stability condition, $\Delta t \sim \Delta x/U_\infty$. The governing equations must be integrated over a number of time steps $N_t \sim T/\Delta t \approx N_c^{1/3}$, which leads to estimating the overall computational cost for a WR-LES as

$$Cost \propto Re_\Lambda^{4/3(2-\alpha)}N_{RK} \simeq Re_\Lambda^{2.4}N_{RK} \tag{3.11}$$

In WM-LES, DES and RANS, the resolution requirements depend on the inner-layer treatment and Equation (3.7) has shown not to be appropriate for turbulence modelling techniques such as WM-LES, in which the inner-layer is modelled, or DES, in which the whole boundary layer is modelled by using a RANS approach. An alternative formulation of the problem can be implemented using an approach similar to the one adopted by Chapman (1978).

3.3 Cavity flow sizing

3.3.1 Spectral width

In this section the aim is to characterize a cavity simulation size and cost by the spatial and temporal discretisation indicators N_c, N_d and N_t. A dimensional analysis enables to regress from the cavity-flow CFD works published in literature typical values to obtain *a priori* cost estimates.

In a cavity-flow simulation, the shortest wavelength is the one related to the wall-normal direction, $\lambda_{\min,W-N}$, to resolve the inner-layer near solid walls. To resolve at least one acoustic wavelength $\bar{\lambda}_{ac}$ of the dominant cavity tone, the wall-normal dimension of the computational domain DS_{W-N} is so that $\bar{\lambda}_{ac} \approx 0.66 DS_{W-N}$. From Equation (3.1) the wavenumber spectral width in the computation is

$$N_d \approx N_{d,W-N} = DS_{W-N}/\lambda_{\min,W-N} \tag{3.12}$$

The next step is to relate N_d to the cavity geometry, inflow conditions and turbulence closure model. The flow inside a cavity depends on the cavity geometry parameters L, D, W, inflow velocity U_∞, inflow boundary layer thickness δ, laminar viscosity ν, density ρ, gravitational acceleration g, and speed of sound c. By restricting the analysis to low speed aerodynamic flows, the effects of g and c are neglected. By application of the Buckingham Π theorem on the remaining variables, the following non-dimensional groups are obtained: L/D, L/W, δ/D, Re_L, PPW, which accounts for the numerical scheme order,

$$n_{D,j} = \frac{DS_{j,\max}}{D} \tag{3.13}$$

which expresses in non-dimensional form the extent of the computational domain boundaries, and

$$r_\tau = \frac{\overline{\Delta x_j}}{\nu/u_\tau} \tag{3.14}$$

which expresses the average mesh spacing near the walls introduced by Equation (3.3) as multiple of the viscous length ν/u_τ. This gives eight independent non-dimensional groups.

With simple algebraic manipulations and by introducing the principle of orthogonality, Rona & Monti (2011) show that it is possible to consider the quantity N_d as the product

of six independent non-dimensional groups, each with its own exponent:

$$N_d = (L/D)^{\alpha_1}\,(\delta/D)^{\alpha_2}\,n_{D,W-N}^{\alpha_3}r_\tau^{\alpha_4}Re_L^{\alpha_5}PPW^{\alpha_6} \tag{3.15}$$

The exponents α_1 to α_6 in Equation (3.15) are determined using the smallest numerical wavenumber $k_{W-N,\min} = 2\pi/DS_{W-N,\max}$ and the highest resolved numerical wavenumber $k_{W-N,\max} = 2\pi/\lambda_{W-N,\min}$ where $\lambda_{W-N,\min} = \left(PPW\overline{\Delta x_{W-N}}\right)$.

In order to explicit the influence of the Reynolds number on N_d, all non-dimensional variables except Re_L can be factorized into a single non-dimensional parameter C_1.

$$N_d = C_1\,(L/D, \delta/D, n_{D,W-N}, r_\tau, PPW)\,Re_L^{1-\alpha/2} \tag{3.16}$$

$$C_1 = \frac{n_{D,W-N}\,(D/\delta)^{\alpha/2}}{PPW\,(L/D)^{1-\alpha/2}\,r_\tau} \tag{3.17}$$

Therefore, the single non-dimensional parameter C_1 includes the information of the turbulence model approach, the domain shape, the boundary layer thickness and the average computational mesh clustering near the solid walls. This is a new simulation parameter that enables to identify and class *ceteris paribus* the quality of a simulation in representing the correct spectral width, given the geometry, mesh, flow and turbulence modelling parameters.

The spectral width of published cavity-flow simulations is presented in Figure 3.2, where the parameter $LN_d = \log_{10} N_d$ has been estimated by Equation (3.12). In Figure 3.2, the number of decades of the spectral width LN_d is plotted against the Reynolds number Re_L. Each past simulation in the graph is identified by a tag associated to its bibliography reference in Table 3.3. The symbols mark the effective spectral width of the simulations, allowing for the use of stretching functions. The C_1 isolines are plotted following Equation (3.16).

The DNS data is clustered on the left hand side in Figure 3.2, towards to the top of the LN_d scale, showing a larger spectral width than LES and DES, as all the scales of motion are resolved directly. Nonetheless, most of the LES and DES simulations present a number of decades comparable with that of a DNS simulation at a lower Re_L. The reason is that WR-LES and DES methods use stringent requirements in the viscous sub-layer. For a WR-LES simulation, the computational mesh density
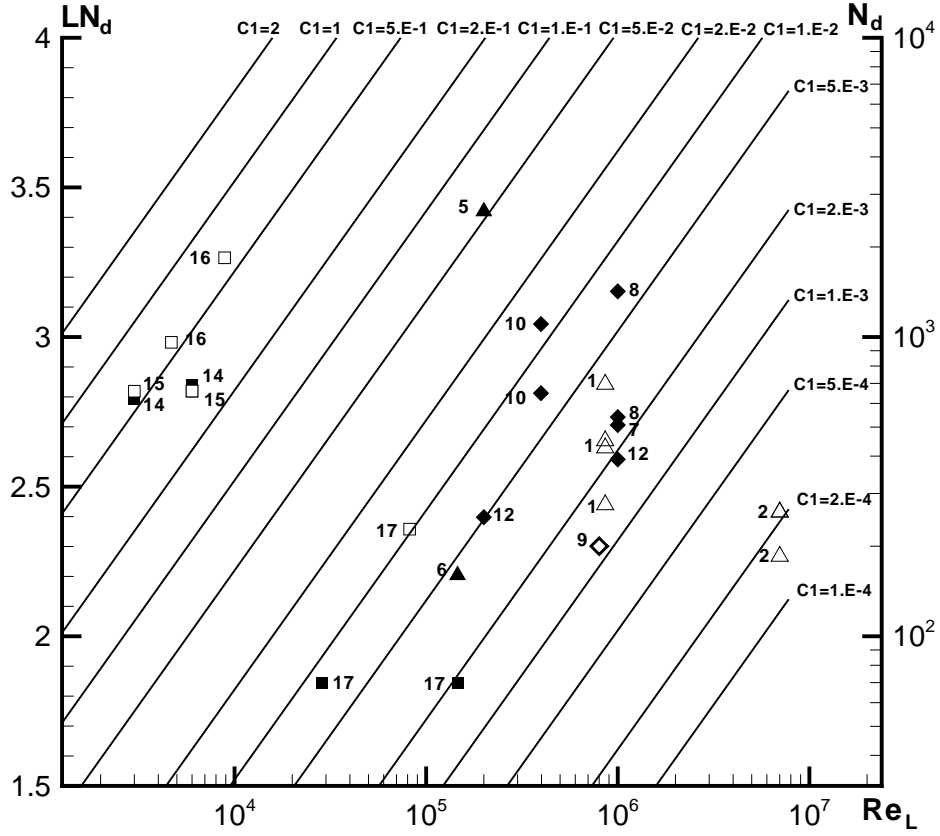
Figure 3.2: Spectral width of cavity-flow simulations versus Re_L for different turbulence models (■ 3D and pseudo-3D DNS; □ 2D DNS; ▲ WR-LES; △ WM-LES; ♦ DES; ◇ WM-DES).

	DNS	DES	Coarse WR-LES	Medium WR-LES	Fine WR-LES	WM-LES
r_τ	$2-140$	$80-200$	>180	<180	$10-14$	$600-1200$
r_τ (analysis)	4	$80-120$	$20-50$	$10-20$	10	700

Table 3.1: Mesh size to viscous length ratio for cavity-flows: range of values obtained from published work.

required to resolve the inner-layer requires onerous computational capabilities already at moderate Reynolds numbers and wall-modelling methods to bypass the *wall layer* are required to perform high Reynolds number cavity LES, such as simulations 5 and 6. The less severe spatial discretisation requirements of Wall-Modelled LES give a lower number of decades LN_d even at high Reynolds numbers compared to WR-LES and DNS.

The bunch of DES of cavity-flow models is centred in the region $2 \times 10^5 \leq Re_L \leq 10^6$ with a typical number of logarithmic decades between 2.4 and 2.8. More spatially refined simulations like 8 and 10 have a spectral width greater than 3 logarithmic decades. In order to reproduce approximately 2.7 logarithmic decades of turbulent structures, DNS computations are constrained to Re_L less than 10^4, whereas WM-LES and DES have shown able to model up to a Re_L of the order of 10^6. Three-dimensional DNS simulations have the same high spatial resolution requirements in all three directions, thus most of the published works is limited to planar two-dimensional computations.

A range of values for the parameter r_τ has been extracted from the cavity-flow simulations in literature by fitting Equations (3.16) and (3.17) to the mesh size data. These results are presented in Table 3.1. The r_τ values are obtained by minimizing the mean square error of N_d for the simulations that have shown best results in the literature. The data fit well for DNS and DES. Unfortunately, few WR-LES simulations have been performed for cavity-flows. A large variation in N_d is obtained for WM-LES, due to the variety of wall models used. The large uncertainty of r_τ for WM-LES technique suggests that the complexity of the current parametric regression on C_1 and r_τ is insufficient to describe the computational mesh effectiveness in reproducing a given spectral width for WM-LES.

3.3.2 Discretization cost

For the analysis of the discretisation cost of cavity-flows it is necessary to analyse separately the techniques that resolve the inner-layer and the ones that aim to model the effect of the inner dynamics on the outer boundary layer. Techniques like WM-LES and DES resolve only the large scale structures in separated flow regions, hence the computational grid density scales with the outer layer grid density.

Applying the approach of Chapman (1978) to cavity-flows, the near-wall flow can be sub-divided into a carpet of cubes of unit volume $N_{\bar{\delta}^3}$, where $\bar{\delta}$ is an average boundary layer thickness covering the full extent of the solid walls wetted by the fluid. The total number of mesh points in this near wall mesh is the product of the average number of points within a volume of $\bar{\delta}^3$ and the number of cubes that fill the boundary layer:

$$N_c = N_0^3 N_{\bar{\delta}^3} \tag{3.18}$$

Using the same dimensional approach of Section 3.3.1, Equation (3.18) becomes:

$$N_c = N_{\bar{\delta}^3} \left(\delta/D, L/D, L/W, n_{D,x}, n_{D,z}, Re_L \right) N_0^3 \tag{3.19}$$

Using Equation (3.18) and relation $\delta \propto xRe_x^{-0.2}$ for a turbulent boundary layer inflow, the dimensional problem for the grid density of a cavity-flow simulation adopting wall-modelling techniques such as WM-LES and DES is obtained after some algebra (Rona & Monti, 2011) as:

$$N_c = C_2 Re_L^{0.4} \tag{3.20}$$

$$C_2 = \left(\frac{L}{D} \right)^{0.4} \left[2 \frac{L/D}{L/W} \left(1 + \frac{L}{D} + a \right) + n_{D,x} n_{D,z} \right] N_0^3 \tag{3.21}$$

$$a = \begin{cases} 0, & 2D \\ L/W, & 3D \end{cases} \tag{3.22}$$

where $n_{D,x}$ and $n_{D,z}$ are the computational domain streamwise and spanwise dimensions normalized by the cavity depth D and the factor a accounts for the presence of the side walls on a *three-dimensional* cavity-flow domain extent, Figure 1.1(b), and is zero for a *pseudo-two dimensional* cavity-flow simulation, Figure 1.1(a).

	DNS	WM-LES
N_0^3	$1200 - 1500$	$900 - 1300$
N_0^3 (analysis)	$1400 - 1500$	$1200 - 1300$

Table 3.2: Number of points per cube N_0^3 for wall-modelling cavity-flows simulations: range of values obtained from published work and suggested values for optimization analysis.

The new non-dimensional group C_2 accounts for the geometry of the cavity and the overall computational domains.

In wall-resolving techniques, like DNS or WR-LES, most of the computational effort goes into resolving the inner-layer. The main factor in the computational cost is the size of the first row of cells along the walls. For DNS, a scaling law for N_c can be derived as:

$$N_c = C_3 Re_L^{3(1-\alpha/2)} = C_3 Re_L^{2.7} \tag{3.23}$$

$$C_3 = \frac{(D/\delta)^{2.7}}{(L/D)^{2.7} \Delta x^+ \Delta y^+ \Delta z^+} \tag{3.24}$$

For a cavity-flow WR-LES, the number of grid points scales asymptotically as:

$$N_c = C_4 Re_L^{2-\alpha} = C_4 Re_L^{1.8} \tag{3.25}$$

$$C_4 = \frac{(D/\delta)^{2-\alpha}}{(L/D)^{2-\alpha} \Delta x^+ \Delta y^+ \Delta z^+} \tag{3.26}$$

Similairly to C_1, the parameters C_2, C_3 and C_4 are new simulation parameters that enable for different turbulent modelling techniques to identify and class *ceteris paribus* the effectiveness of a simulation in resolving the turbulent scales, given the geometry, the mesh, and the flow parameters.

The grid density of published cavity-flow simulations that use different turbulence models is shown in Figure 3.3. The symbols mark the effective number of grid points in each simulation, which is identified by Table 3.3.

The isolines of C_2 are plotted following Equation (3.20). The isolines of C_3 for DNS and of C_4 for WR-LES are obtained from Equations (3.23) and (3.25), respectively.

Typical DNS simulations lie in the range $10^{-2} < C_3 < 10^{-4}$. For completeness, 2D DNS simulations are included in the graph. For 3D DNS, the state-of-art simulation 14 used 7.5 and 12.2 million cells at a $Re_L = 3 \times 10^3$ and $Re_L = 6 \times 10^3$, respectively. The region of WR-LES simulations $5 \times 10^3 < Re_L < 2 \times 10^5$ shows the dense mesh resolution required to simulate the inner layer dynamics even at a relatively small Reynolds number.

DES simulations are grouped in a range of grid density between 0.8 to 5 millions cells and $10^5 < Re_L < 10^6$. The finest mesh DES is simulation 8, which gives a
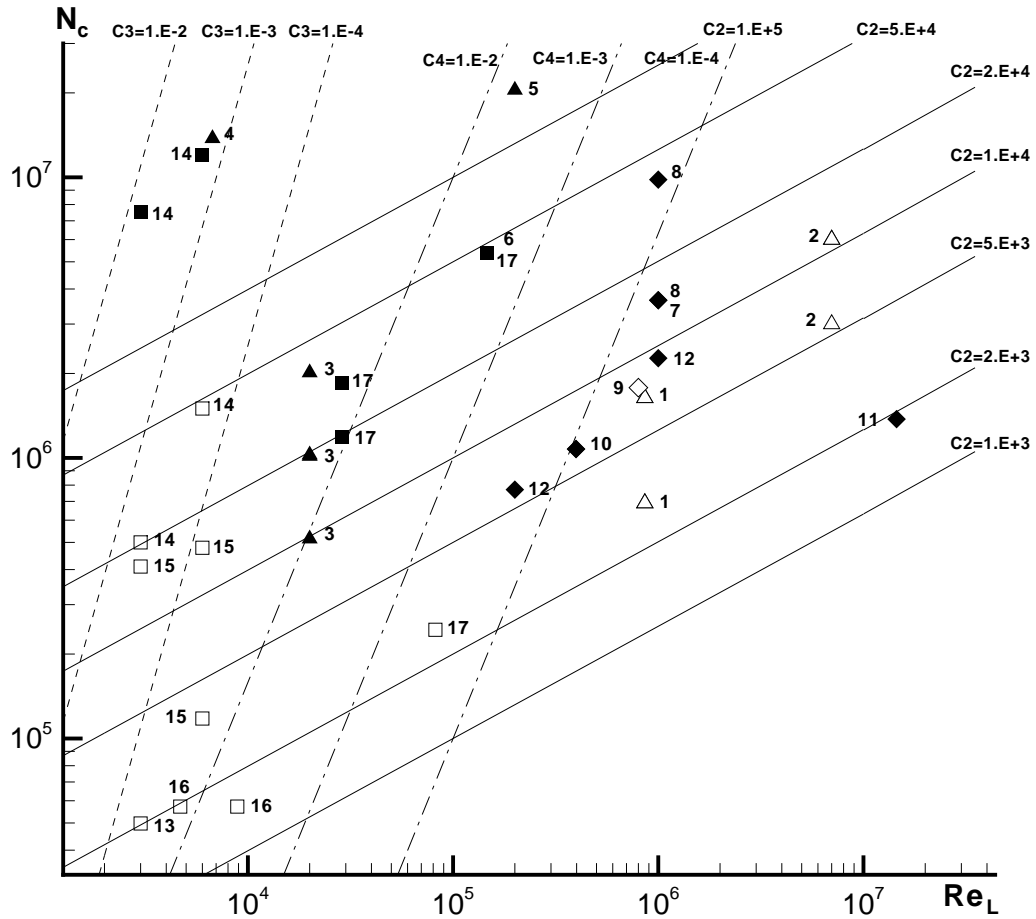
Figure 3.3: Grid density versus Re_L for different turbulence models. ■ 3D and pseudo-3D DNS; □ 2D DNS; ▲ WR-LES; △ WM-LES; ♦ DES; ◇ WM-DES; continuous lines: isolines of C_2 slope $Re_L^{0.4}$ (DES, WM-LES); dotted lines: isolines of C_3 slope $Re_L^{2.6}$ (DNS); dashed-dotted lines: isolines of C_4 slope $Re_L^{1.8}$ (WR-LES).

spatial resolution comparable to that of an LES. The grid resolution requirement of DES is comparable to that of a WM-LES and the reason is that both techniques aim to model the effects of unresolved inner-layer structures on the outer layer and to resolve mixing layer eddies in the separated regions like in an LES. Both DES and WM-LES have therefore a comparable computational mesh density that is associated with resolving the outer layer near solid walls. This shows that the idea of DES as a coarser grid version of LES in massively separated flow regions and other free shear flows

is incorrect and inappropriate as observed by Spalart *et al.* (2006). DES differs from LES only in the RANS portion of boundary layers, where the difference in the required resolution in the spanwise and streamwise directions is wide.

The non-dimensional group C_2 in Equation (3.21) accounts for the geometry of the cavity and the shape of the computational domain. Like in the spectral width analysis of Section 3.3.1, a range of values for the number of points per cube N_0^3 in cavity-flow simulations has been made explicit by calculating the coefficients C_2 for the simulations in the available literature and minimizing the mean square error of N_c from fitting Equations (3.20) and (3.21) to this data.

In Table 3.2 the range of values from past CFD work is presented in the first row while in the second row a set of values with a narrower range are stated. These are used in Section 3.3.3 to estimate the cost of WM-LES and DES.

3.3.3 Simulation complexity

From Equation (3.5), with $N_t \sim T/\Delta t \approx N_c^{1/3}$, the total complexity of a simulation that does not resolve the inner-layer (WM-LES and DES) is:

$$Cost = C_2^{1.3} Re_L^{0.54} N_{RK} \tag{3.27}$$

For a WR-LES, considering the operation cost N_t for time advancement, the complexity is:

$$Cost \propto C_4^{4/3} Re_L^{4/3(2-\alpha)} N_{RK} \approx C_4^{1.3} Re_L^{2.4} N_{RK} \tag{3.28}$$

For DNS, the size of the time step Δt scales as $Re^{\alpha+1/2}$ and the total cost of the simulation is:

$$Cost \propto C_3^{3/2+\alpha} Re_L^{3(1-\alpha/2)} Re_L^{\alpha+1/2} N_{RK} \approx C_3^{1.6} Re_L^{3.3} N_{RK} \tag{3.29}$$

Figure 3.4 presents the computational cost for cavity-flow simulations in which the time advancement is by a single step Runge-Kutta time integration, such that

$$\overline{Cost} = \frac{N_C N_T}{N_{RK}} = N_C N_t \tag{3.30}$$

Hence, the cost estimate in Figure 3.4 from Equation (3.30) must be multiplied by the number of temporal integration stages, such as the number of Runge-Kutta stages,

to estimate the total cost of the simulation. The results in Figure 3.4 are obtained using $N_t \sim T/\Delta t \approx N_c^{1/3}$ and are presented only to give a first estimate of the cost of simulating cavity-flows.

The left y-axis in Figure 3.4 is the cost obtained by Eq. 3.30. The right y-axis is the same cost in CPU time for a single processor scalar computation, based on a IBM Power5 1.9GHz 4.5 Mflop/s processor. The time cost to obtain statistical convergence is estimated to be three times the simulation time advancement cost, which in a cavity-flow simulation is the flow-through time for a fluid particle to traverse once the computational domain in the streamwise direction. The operation count reflects that of a representative second-order method of an in-house CFD solver (Grottadaurea & Rona, 2007, 2008).

For moderate Reynolds numbers, the cost of the computation associated with resolving the inner-layer along solid walls is lower than that to resolve the remainder outer region (Piomelli & Balaras, 2002).

The cost of wall-resolving low Reynolds number flows therefore scales as the cost of resolving the outer layer by a wall-modelling technique. This results in $Cost\,(C_3) = \max\,[Cost\,(C_2)\,,Cost\,(C_3)]$ and $Cost\,(C_4) = \max\,[Cost\,(C_2)\,,Cost\,(C_4)]$ and the isolines for C_3 and C_4 are truncated at the appropriate intercept with C_2 isolines. Figure 3.4 enables to make an *a priori* order of magnitude estimate of the computational cost of a cavity-flow CFD simulation.

Given the cavity shape and boundary layer inflow conditions, the three isolines for a wall-modelling technique (WM-LES, DES), DNS and WR-LES, are determined from Equations (3.21), (3.24) and (3.26). For instance, for a given cavity-flow Reynolds number Re_L, the intercept of the $Re_L =$ constant vertical line with the isoline C_2 (by using Equation (3.21) and the DES value for of Table 3.1) gives an order of magnitude estimate of the total computational cost for a DES simulation. The intercept with the C_3 and C_4 isolines give the cost for the other two turbulence modelling techniques.

If the CFD solver is parallelised, the run time decreases as the number of processors increases. Specifically,

$$RunTime = \frac{N_C N_t N_{RK}}{\mu_P N_P} \tag{3.31}$$

where N_P is the number of processor used and μ_P is the parallelisation efficiency of the
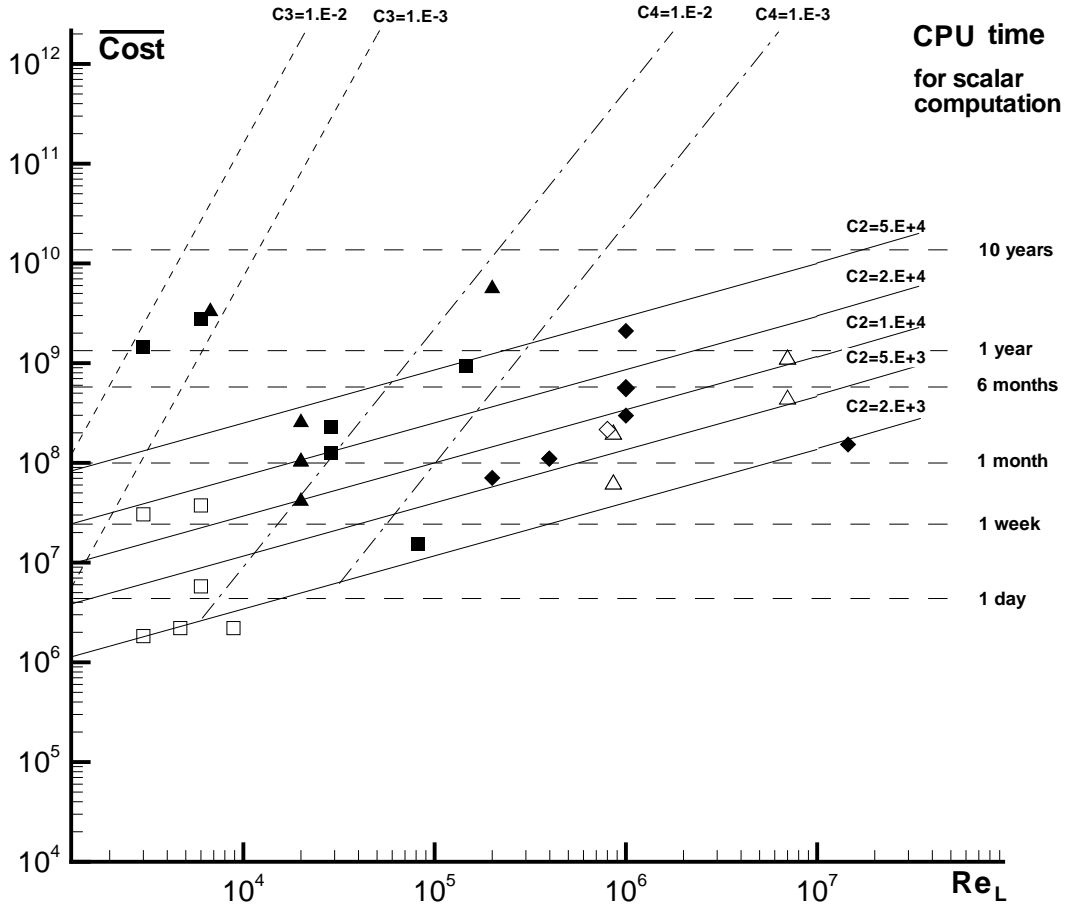
Figure 3.4: Normalized simulation cost versus Re_L for different turbulence models. ■ 3D and pseudo-3D DNS; □ 2D DNS; ▲ WR-LES; △ WM-LES; ♦ DES; ◇ WM-DES; continuous lines: isolines of C_2 slope $Re_L^{0.54}$ (DES, WM-LES); dotted lines: isolines of C_3 slope $Re_L^{3.6}$ (DNS); dashed-dotted lines: isolines of C_4 slope $Re_L^{2.4}$ (WR-LES).

algorithm for N_P processors. Parallelisation reduces the run time, but not the computational cost, which is higher than that of a scalar computation given by Equation (3.5).

Legend tag	Reference
1	Larchevêque *et al.* (2004b)
2	Larchevêque *et al.* (2004a)
3	Suponitsky *et al.* (2005)
4	Chang *et al.* (2006)
5	Rizzetta & Visbal (2003)
6	Gloerfelt *et al.* (2002b)
7	Basu *et al.* (2005)
8	Basu *et al.* (2006)
9	Shieh & Morris (2001)
10	Chang & Park (2004)
11	Arunajatesan *et al.* (2002)
12	Hamed *et al.* (2003)
13	Hamed *et al.* (2001)
14	Bres & Colonius (2007)
15	Rowley *et al.* (2002)
16	Moon *et al.* (2003)
17	Gloerfelt *et al.* (2002b)

Table 3.3: Cavity flow simulations used in Figure 3.2 to 3.4.

Chapter 4

Cavity inlet

This chapter presents a spatially developing boundary layer model that uses the SSTD inflow condition of Section 2.4. This test case is used as precursor simulation to the cavity flow model of Chapter 5. Section 4.1 gives the dimensional and non-dimensional flow parameters that define the boundary layer model. The computational mesh is detailed in Section 4.2, the boundary conditions are reported in Section 4.3 and the results of the scalability performance tests on a HPC cluster are presented in 4.4. LES results and comparison with approximate analytical solutions and experimental results are then given in Section 4.5.

4.1   Flow conditions

The SSTD method is used to generate an LES model of a zero pressure gradient boundary layer developing over a flat plate. The inlet plane free stream Mach number is 0.126 and the time averaged integral length scales of the boundary layer thickness δ_0, displacement thickness δ_0^*, and momentum thickness θ_0 give $Re_{\delta_0} \approx 5200$, $Re_{\delta_0^*} \approx 720$, $Re_{\theta_0} \approx 570$, where the subscript 0 indicates the condition at the computational domain inflow.

4.2   Computational domain geometry and mesh

The computational domain selected for the precursor LES inflow with the SSTD boundary condition is a rectangular prism the size of which is $DS_x \times DS_y \times DS_z = 37\delta_0 \times 7\delta_0 \times 4\delta_0$, where δ_0 is the time-averaged boundary layer thickness at the domain inlet. The selected spanwise size of the domain is large enough to accommodate 8 streaks, the size of each streak being approximately $120 - 140y^+$.

The rectangular prism is discretised by a topologically orthogonal mesh of $N_{cx} \times N_{cy} \times N_{cz} = 154 \times 86 \times 72 \approx 10^6$ cells.

The mesh spacing in the streamwise direction x and in the spanwise direction z is uniform, resulting in a constant spacing $\Delta x \approx 60y^+$ and $\Delta z \approx 14y^+$. In the wall-normal direction, the first four cells are of dimension $\Delta y = y^+ = 1$ to ensure a correct resolution of the boundary layer viscous sub-layer. The cell spacing above the fourth cell is obtained by using two successive constant proportional stretching ratios: $\epsilon_1 = 1.058$ up to the tenth cell and $\epsilon_2 = 1.08$ thereafter. The two ratios were selected as to provide a good compromise between numerical resolution (cells within the boundary layer $N_\delta = 55$) and computational cost. Mesh resolution of the spatially developing boundary layer test case in all directions is comparable with that of the finest WR-LES simulations by Table 3.3.

4.3   Boundary conditions and starting flow conditions

In this simulation, the boundary condition used were: the SSTD boundary condition of Section 2.4 at the inlet of the rectangular prism, a non-slip adiabatic condition for the solid wall of the domain, extrapolation from the inner cells at the outflow boundary, a non-reflecting condition at the upper boundary opposite to the flat plate wall, to minimize spurious reflections of disturbances, and periodic boundary conditions at the lateral boundaries in the spanwise direction of the domain.

The initial velocity field was primed in the streamwise direction by a discrete number of mean profiles stations by Equations (2.44), and considering a $1/7^{th}$ power law growth of the mean profiles, in the same direction. Fully synthetic fluctuations over the mean profiles were sumperimposed by Equations 2.45, 2.46, and using the parameters of Table 2.1. Divergence-free random velocity noise with a maximum amplitude

$u'_{rms}/u_\infty < 4\%$ were also superimposed on the synthetic disturbances, to break the symmetries arising from the the deterministic specification of the inlet fluctuations. The wall-normal mean profile of the turbulent kinetic energy $\bar{k}$ was primed using the $k - \omega$ multiscale model by Wilcox (1988), implemented with the numerical procedure of Wilcox (1981). Further details of the algorithm and model can be found in Wilcox (2002).

4.4 Parallelisation performance

The boundary layer inlet LES simulation was run on the IBM-SP6 cluster of the HPC centre CINECA, Italy.

The cluster offers hardware support for Simultaneous Multi-threading (SMT). In a SMT processor design, multiple instructions from more than one thread can be issued in any given pipeline cycle. Unlike other hardware multi-thread architectures, SMT permits all thread to simultaneously compete for and share processor resources. This is done without great changes to the basic processor architecture, the main addition being only a larger register file to hold data from multiple threads.

Preliminary scalability tests were performed on the nearly 1M cells LES grid to choose the best solution in terms of number of processors and multi-threading mode.

The parameters used for scalability analysis are the code speed-up and the parallelisation efficiency. Let T_0 be the scalar time needed to perform one time step (two Runge-Kutta sub-iterations) using the serial code on a single processor of the cluster, and T_P the time to perform the same operation by the parallelised code on N_P processors. The speed-up S_P is defined as

$$S_P = T_0/T_P \tag{4.1}$$

and the parallelisation efficiency is

$$\mu_P = S_P/N_P \tag{4.2}$$

The result of the scalability performance analysis obtained for the RDD parallelisation algorithm of Section 2.5 is presented in Figure 4.1. The ideal speed-up corresponds to the straight green line $S = N_P$ in Figure 5.2(a).
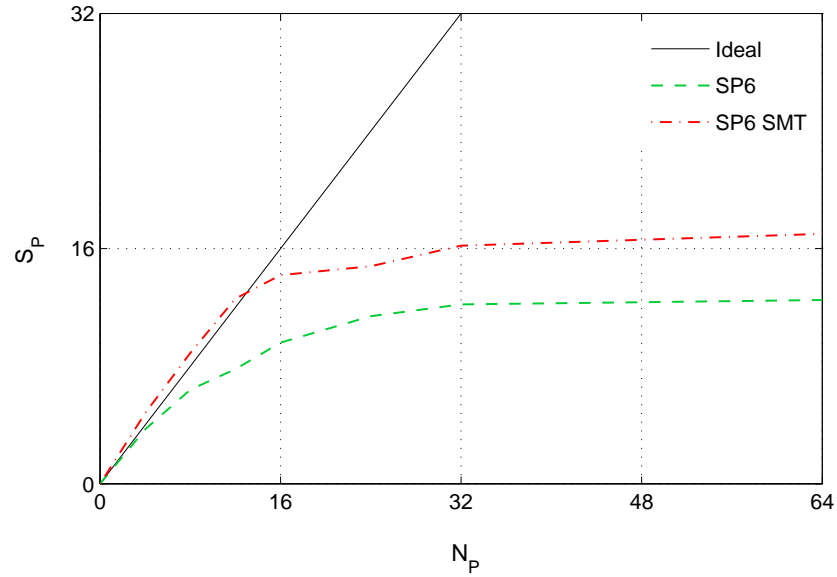
(a)
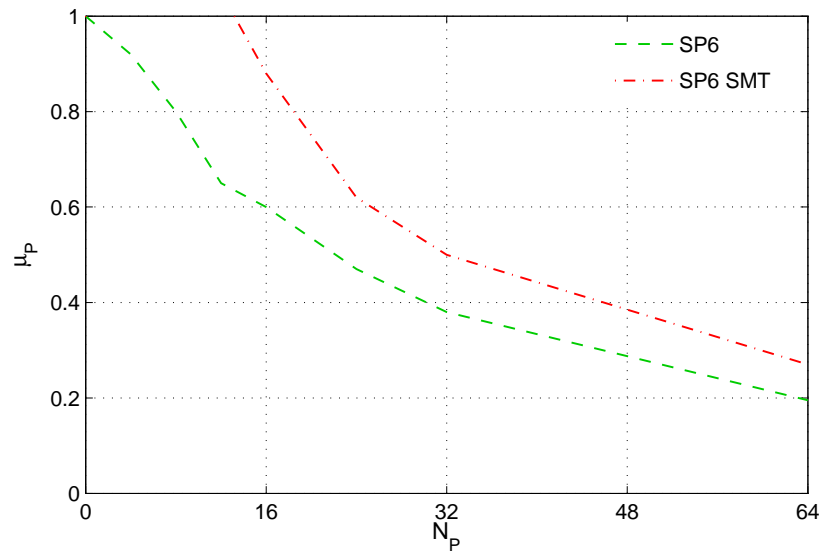
(b)

Figure 4.1: Boundary layer LES with a single block mesh of 1×10^6 cells, scalability performance test on SP6 IBM cluster. (a) Speed-up S_P and (b) parallelisation efficiency μ_P (b) for different numbers of processors N_P.

By increasing the number of processors, the speed-up growth is normally limited by the communication time and by the load balance.

For this test case $S_P > N_P$ up to $N_P = 12$, hence the code shows a super-linear speed-up due to cache aligning. For $N_P > 16$, the ratio of communication versus computation increases to a level where a further reduction in computational time by domain sub-division is not achieved. This is caused essentially by the communication overhead through the communication planes, from sub-dividing a relatively small CFD computational domain into more zones.

The parallelisation efficiency for SMT mode remains higher than that from single threading for any number of processors, as shown in Figure 5.2(b).

From Figures 5.2(a) and 5.2(b), the optimal number of processors, taking into account the available CPU time and wall time constraint on the SP6 IBM machine for this study, was empirically determined as $N_P = 32$ with SPM enabled. In this configuration, the speed-up was $S_{32} \approx 16.2$, the parallelisation efficiency $\mu_{32} \approx 0.5$ and the parallel computation wall time for one time step approximately $T_{32} = 2.1$ seconds. The flow-through time, which is the time required for a fluid particle to get across the computational domain, was equivalent to $220K$ iterations. In a typical LES computation, the initial transient needs at least three flow-through times to complete (Tessicini *et al.*, 2006). Hence, the total CPU time for the simulation running on 32 processors was 13.07×10^3 CPU hours and the wall time 410 hours (≈ 17 days).

4.5   Results

4.5.1   Computational mean velocity profile

At run time, oscillations were generated by the SSTD technique at the inlet section and propagated throughout the LES scheme.

The three flux limiters of Section 2.2 were tested in this LES simulation to assess which limiter exhibited the best oscillatory behaviour. Specifically, it was of interest to determine which limiter allowed the development of physical boundary layer instabilities like streaks for a turbulent boundary layer, while preserving the TVD properties of the scheme.

Non-dimensional velocity profiles of the zero pressure gradient spatially developing boundary layer were extracted at four different streamwise stations, at coordinates $X = 8\delta_0, 16\delta_0, 24\delta_0, 32\delta_0$, to analyse the boundary layer growth and flux limiter performance. The profiles were extracted at three flow-through times, which was estimated sufficient for the initial CFD start up transient to decay. The velocity profiles are time-averaged over the last 10^5 iterations to filter any velocity fluctuations around the mean. The three flow limiters cover the upper and lower ranges of ϕ values satisfying the conditions (2.39) to (2.41). For the Minmod limiter, $\lim_{r \to \infty} \phi(r) = 1$, for the Superbee limiter, $\lim_{r \to \infty} \phi(r) = 2$, and for the Sweby limiter, $\lim_{r \to \infty} \phi(r) = \beta$ with $1 \le \beta \le 2$.

Figure 4.2 shows the non-dimensional velocity from the LES simulations that use the Superbee limiter and the Minmod limiter, which are respectively the upper and lower bounds of ϕ. The normalised mean streamwise velocity u^+ is plotted against the normalised wall-normal distance y^+ for each of the four stations.

Figure 4.2(a) shows that the Superbee limiter is not dissipative enough in the smooth region of flow and this results in over-amplified oscillations and time-averaged values of streamwise velocity higher than that from the law of the wall. On the contrary, Figure 4.2(b) shows the more dissipative Minmod limiter causes a re-laminarisation of the inner layer velocity profile that prevents the boundary layer from growing the overlap region at the correct non-dimensional distance of around $30y^+$ from the wall.

Simulations with different values of $\beta = (1.05, 1.25, 1.3, 1.35, 1.6)$ were run to test the Sweby limiter. The best result is shown in Figure 4.3, obtained for $\beta = 1.3$. A transition region is required for the flow to develop streaks and other distinguishing large-scale structures of a turbulent boundary layer, in agreement with the work on LES inflow conditions by Keating *et al.* (2004). The shape of the first two time-averaged velocity profiles downstream of the inlet plane at $X_1 = 8\delta_0$ (red circles) and $X_1 = 16\delta_0$ (green diamonds) indicates a re-laminarisation of the inner layer velocity profile over the range $0 < X < 16\delta_0$. This re-laminarisation is confirmed by low values of the friction coefficient C_f which are in the range of $1.4 < C_f < 1.8$, whereas a $1/7^{\text{th}}$ power law (turbulent) boundary layer would give C_f in the range $1.9 < C_f < 2.1$ over the Reynolds number range $17500 < Re_x < 36000$. The skin friction coefficient recovers slowly between $X = 16\delta_0$ and $X = 24\delta_0$. From $X = 24\delta_0$, the time-averaged velocity
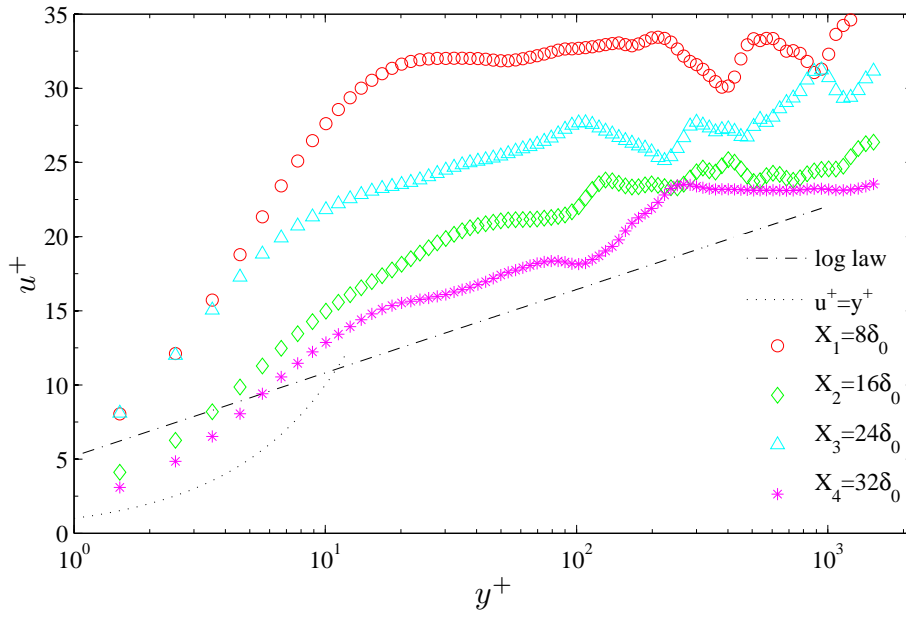
(a)
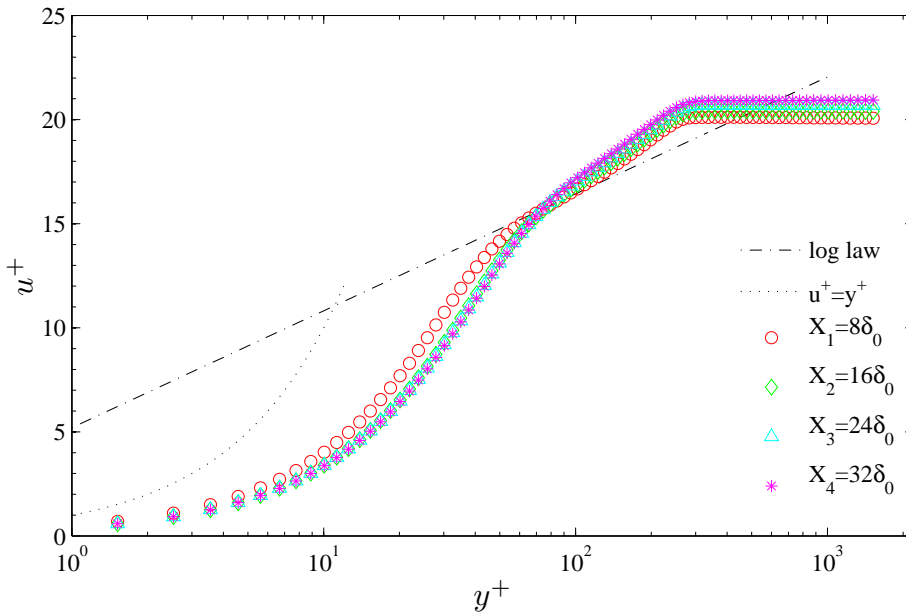
(b)

Figure 4.2: Non-dimensional time-averaged velocity profiles of the zero pressure gradient spatially developing boundary layer at four different streamwise stations, using the (a) Superbee and (b) the Minmod limiters by Roe (1986).
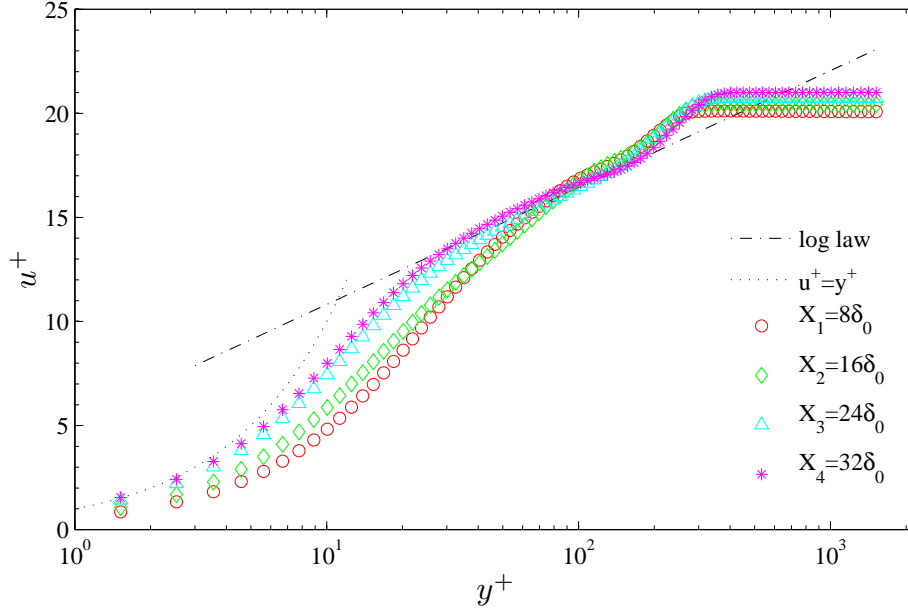
Figure 4.3: Non-dimensional time averaged velocity profiles of the zero pressure gradient spatially developing boundary layer at four different streamwise stations, using the Sweby (1984) limiter with $\beta = 1.3$.

4.5.2 Results validation

Figure 4.4 shows the non-dimensional time-averaged velocity profile from LES (Sweby limiter, $\beta = 1.3$) compared against a range of analytical and experimental results. The LES velocity profile was extracted at $X = 32\delta_0$ from the computational domain inlet, giving a $Re_\delta \approx 7720$, $Re_{\delta^*} \approx 1100$, and $Re_\theta \approx 910$.

In Figure 4.4, the dash-dot line is the Von Kármán (1930) law of the wall, and the continuous straight blue line is the Finley *et al.* (1966) composite velocity profile for $Re_\theta = 930$ that uses the Musker (1979) law of the wall for the inner layer. Circles are the PIV measurements by Haigermoser (2009) at $Re_\theta = 930$ and the squares are the LDV measurements by De Graaff & Eaton (2000) at $Re_\theta = 1420$. There is an appreciable agreement among the numerical, experimental, and analytical velocity profiles across the boundary layer.

Figure 4.5(a) is an enlargement of Figure 4.4 showing the inner layer portion of the boundary layer. The LES predictions show to closely follow the Musker (1979) law across the inner layer up to $y^+ = 20$, indicating that the LES turbulence closure com-
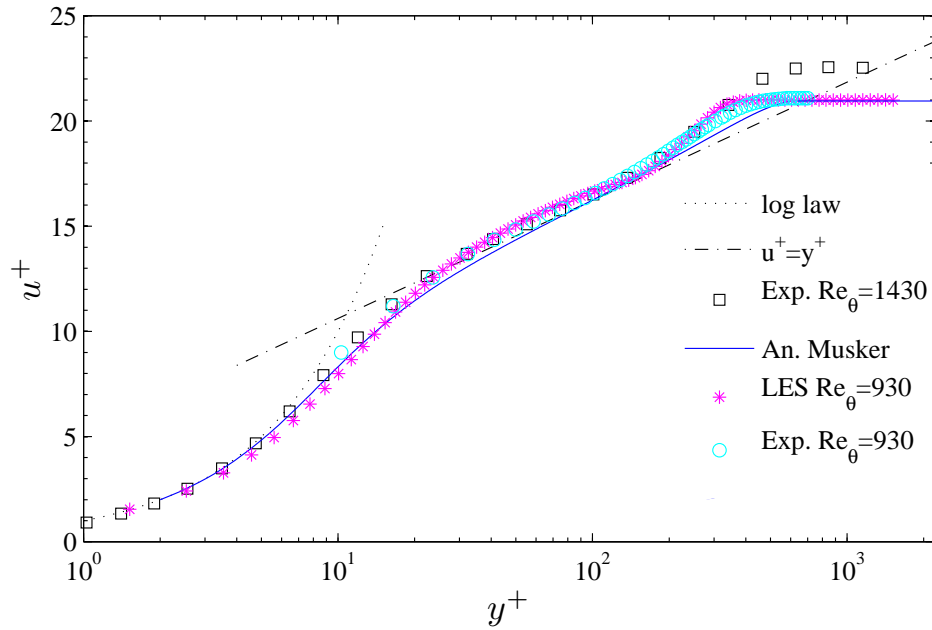
Figure 4.4: Comparison of the LES non-dimensional time-averaged velocity profiles versus analytical and experimental profiles

bined with the dissipative characteristics of the second-order scheme with the Sweby limiter dissipates about the right amount of resolved kinetic energy close to the wall. In the region of transition between viscous sub-layer and the logarithmic overlap region, there is a good match with the experimental results.

Figure 4.5(b) shows an enlargement of the outer portion of boundary layer. The velocity profile predicted by LES exhibits a good agreement with the PIV measurements by Haigermoser (2009) that are a good match with the LES prediction across the full profile.

Similarity with analytical and experimental curves, are further detailed in Figures 4.5(a) and 4.5(b), for the inner and outer regions, respectively.

profile becomes reasonably asymptotic to the viscous law $y^+ = u^+$ (dotted line) and the Von Kármán (1930) law of the wall (dash-dot line).
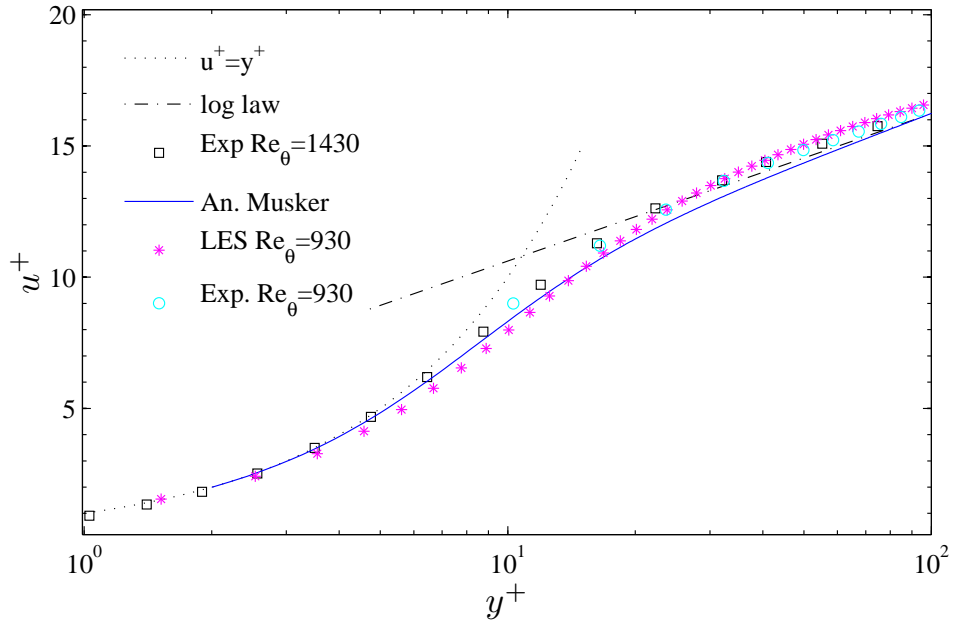
(a)
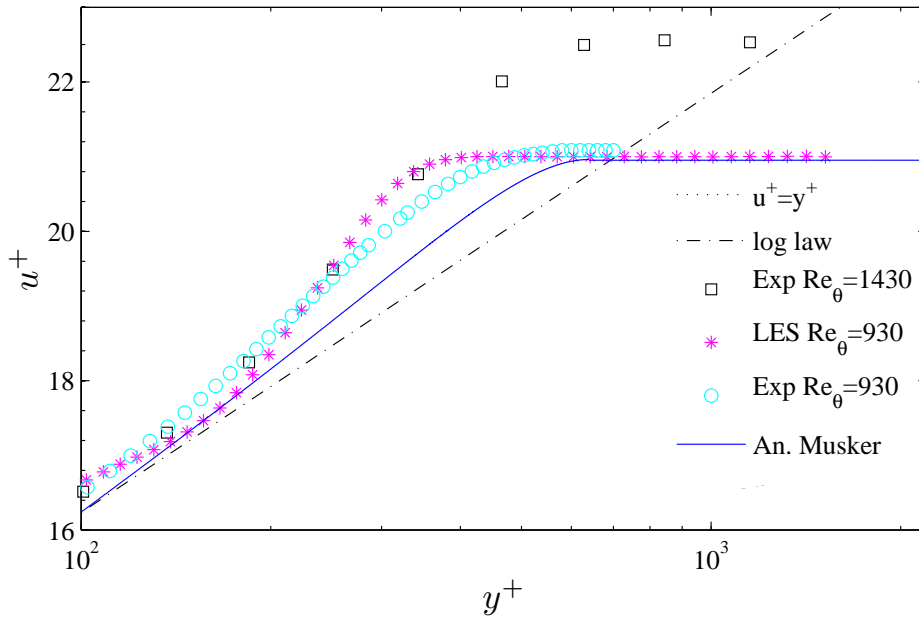
(b)

Figure 4.5: Detail of the inner (a) and outer (b) time-averaged streamwise velocity profiles from LES, experimental, and analytical models.

4.5.3   Unsteady flow

Among the many organized structures observed in near-wall turbulent flows, streaks are considered to be of major importance for their role in the generation of turbulent kinetic energy. Streaks are regions of slowly moving fluid elongated in the direction of the mean flow that are lifted by wall-normal motions from the wall into the higher speed regions, generating organized and coherent structures like hairpin vortices.

Figure 4.6 shows the instantaneous predictions of the streamwise velocity on the $y^+ = 15$ plane at four incremental computational times with constant increment $\Delta t = 1.3$ FT. At the initial time $t = 0$, the flow field is populated only by synthetic fluctuations with small random disturbances, and large periodicity in the streamwise and spanwise directions that are imposed by the initialisation procedure of the computation. After 1.3 FT times the field begins to show self-organized coherent structures, although the velocity field still exhibits a strongly symmetric organization. The streaks the region downstream the re-laminarisation of the flow are not well defined. After 2.6 FT times, the streaks are developed and the initial flow transient is fully extinguished. The higher aspect ratio identifies independent structures with a defined spanwise lengthscale for each streak. At 3.9 FT times, multiple levels of velocity isocontours mark fully developed streaky structures with evidence of fine scale turbulence generation and elongated structures in the streamwise direction.

In Figure 4.7 the three-dimensional turbulent boundary layer field is shown by the Q-criterion by Hunt *et al.* (1988). Since in a boundary layer the gradient of u in the wall-normal-direction is large near the wall, any numerical flow visualization of the turbulence by vorticity isocontours will be overshadowed by the time-averaged velocity gradient effect. The Q-criterion is a vortex identification criterion, defined by the second invariant of the velocity gradient tensor:

$$Q = -\frac{1}{2}(\mathbf{S} : \mathbf{S} - \mathbf{\Omega} : \mathbf{\Omega}) = -\frac{1}{2}\nabla\mathbf{U} : \nabla\mathbf{U} \tag{4.3}$$

Where $\mathbf{S} = \nabla\mathbf{U} + \mathbf{U} \otimes \nabla$ is the rate of strain and $\mathbf{\Omega} = \nabla\mathbf{U} - \mathbf{U} \otimes \nabla$ is the vorticity tensor. When the Q-criterion is positive, it represents locations in the flow where the rotation dominates the strain and shear. At the initial time $t = 0$, the field is populated only by synthetic fluctuations with no momentum transfer in turbulence generation mechanisms. At 1.3 FT times the flow starts to be organized in coherent structures with

T=0   U (m/s)

(a)

T=1.3FT

(b)

T=2.6FT

(c)

T=3.9FT

(d)
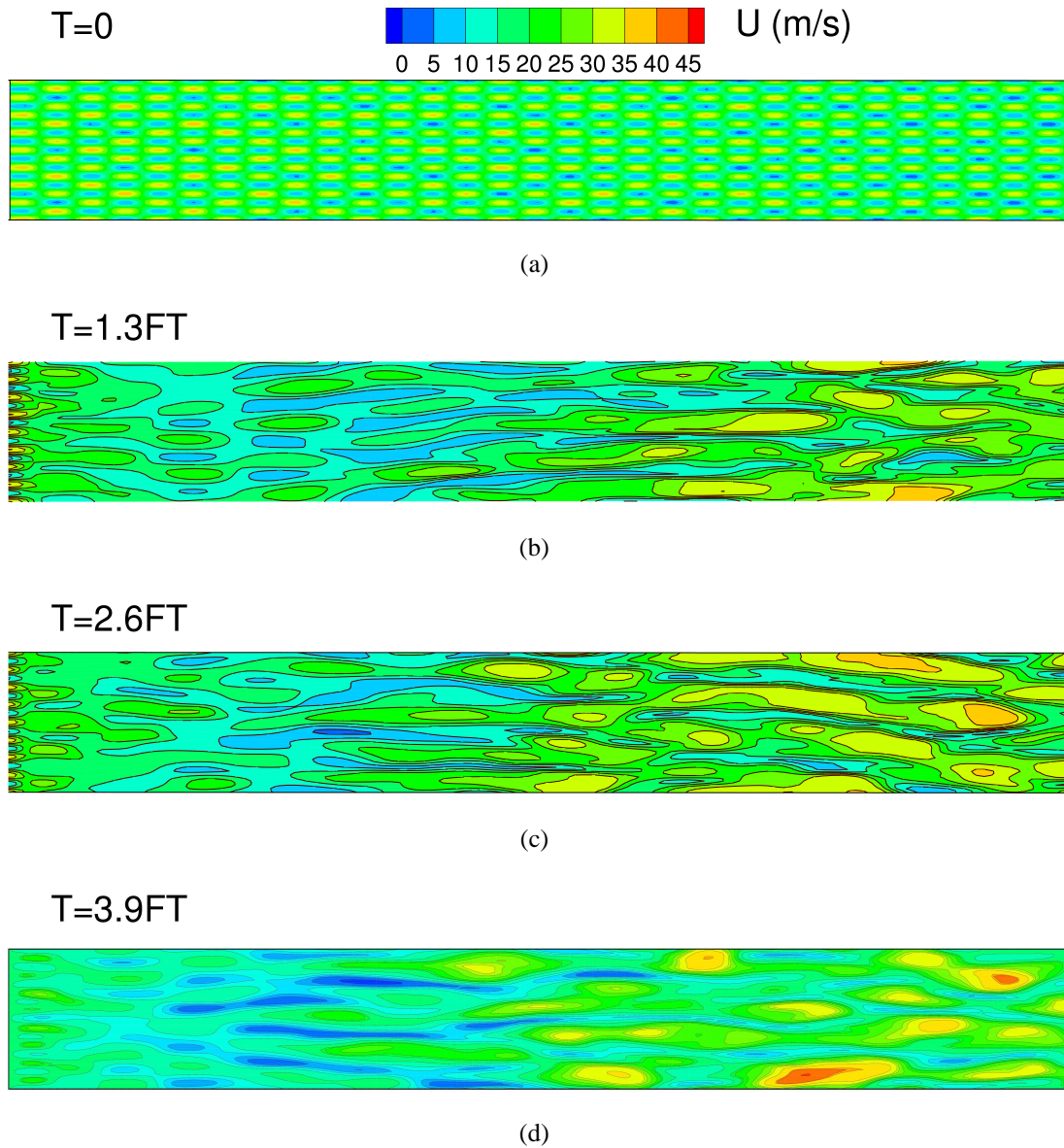
Figure 4.6: Streaks at $y^+ = 15$ slices by isocontours of streamwise velocity (flood + lines)

random motion. After 3 FT times, the turbulence generation mechanism in LES is completely activated. Fine structures can be identified beyond the transition region near the inlet section where synthetic oscillation are generated.

4.5.4 Unsteady flow statistics

The determination of the characteristic spanwise length-scale in a boundary layer can be performed by velocity auto-correlation analysis. Given the streamwise velocity perturbation $u' = u - \langle u \rangle$, the two-point spanwise auto-correlation function is defined as

$$R_{uu}(y, \Delta z) = \langle u'(t, x, y, z)u'(t, x, y, z + \Delta z) \rangle \tag{4.4}$$

Angular brackets denote averaging over time and over the homogeneous directions x and z. Δz in the computation of the discrete auto-correlation is the constant spanwise mesh size.

A common method for estimating the streak spacing is to calculate the streak spanwise lengthscale as $L_u(y) = 2\Delta z_{min}$, where Δz_{min} is Δz at which the minimum of auto-correlation function is found within the first 300 viscous lengths.

A similar analysis can be performed of the spanwise velocity perturbation $v' = v - \langle u \rangle$ from which the two-points spanwise auto-correlation

$$R_{vv}(y, \Delta z) = \langle v'(t, x, y, z)v'(t, x, y, z + \Delta z) \rangle \tag{4.5}$$

estimates the spanwise lengthscale as $nL_v(y) = 2\Delta z_{min}$.

In Figure 4.8, R_{uu} and R_{vv} are plotted at $y^+ = 15$ (continuous line), and $y^+ = 35$ (dashed line). The first minimum in R_{vv} in Figure 4.8(b) is at $\Delta z_{min}|_{y^+=15} = 80y^+$, from which $L_v(15y^+) = 160y^+$. Similarly, $L_v(35y^+) = 230y^+$. A similar result is obtained using the R_{uu} function, although the minima at $y = 35y^+$ is more like plateau and therefore less localised in Δz.

The results found confirmation in literature, where for subsonic boundary layer flows $L_v(15y^+) = 140y^+$, and $L_v(35y^+) = 230y^+$ (Chernyshenko & Baig, 2005; Hu & Sandham, 2001).
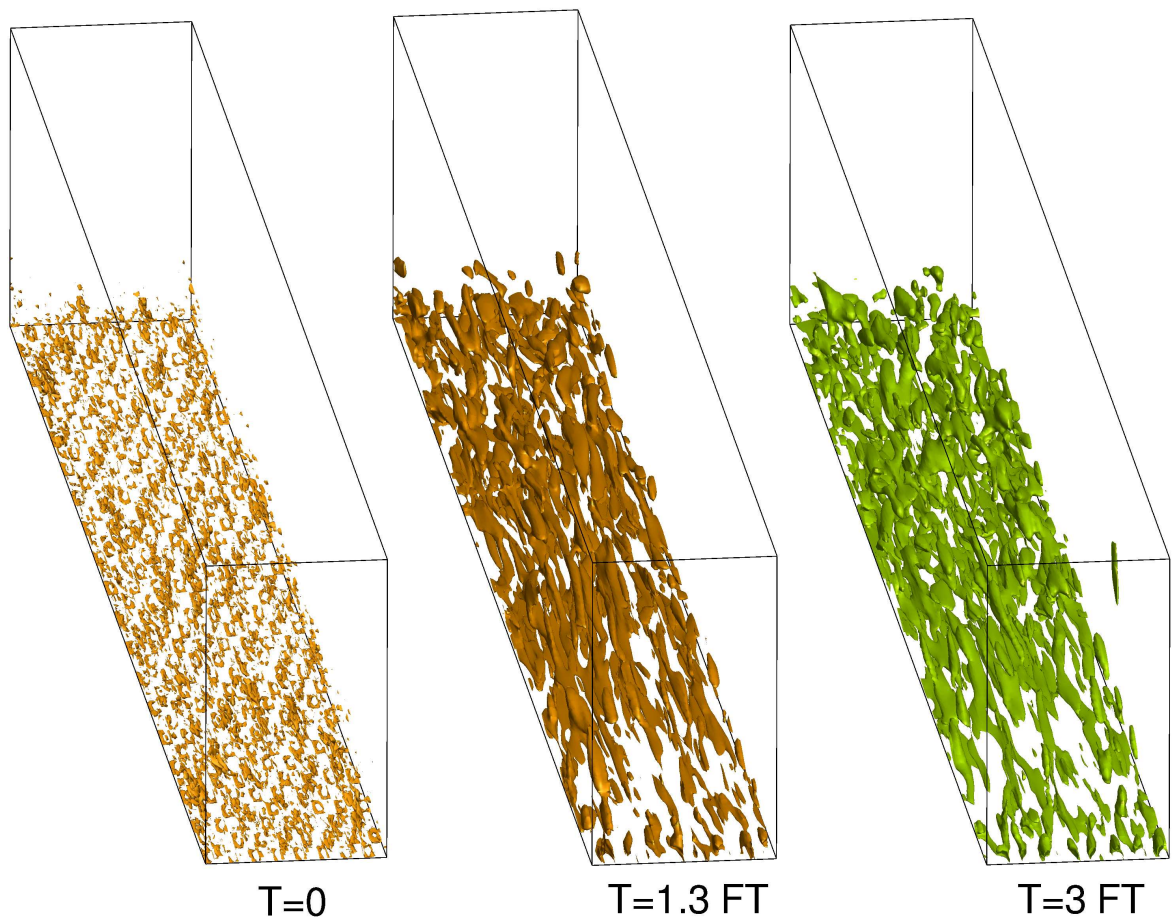
Figure 4.7: Isocontours of vortical structures by Q-criterion at $Q = 2.5 \times 10^6$. Incremental time between two successive frames $\Delta t = 1$ inlet flow through times.
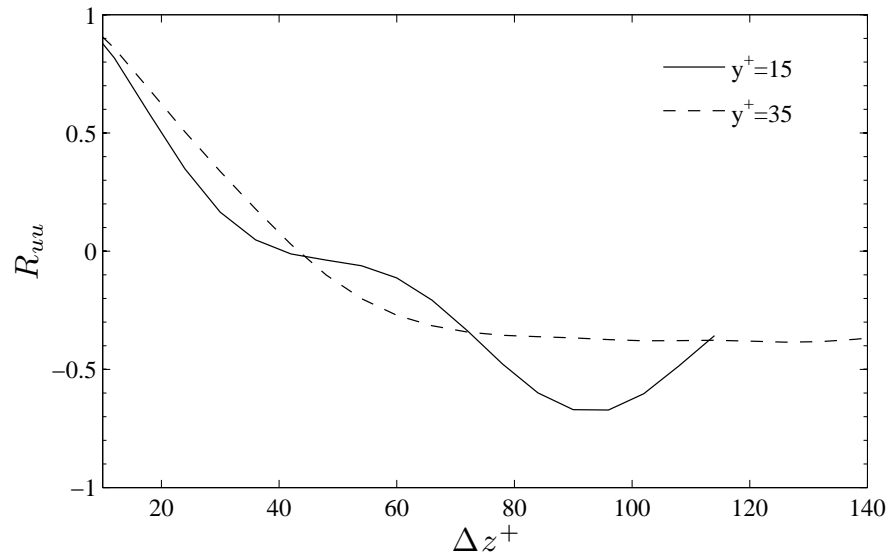
(a)
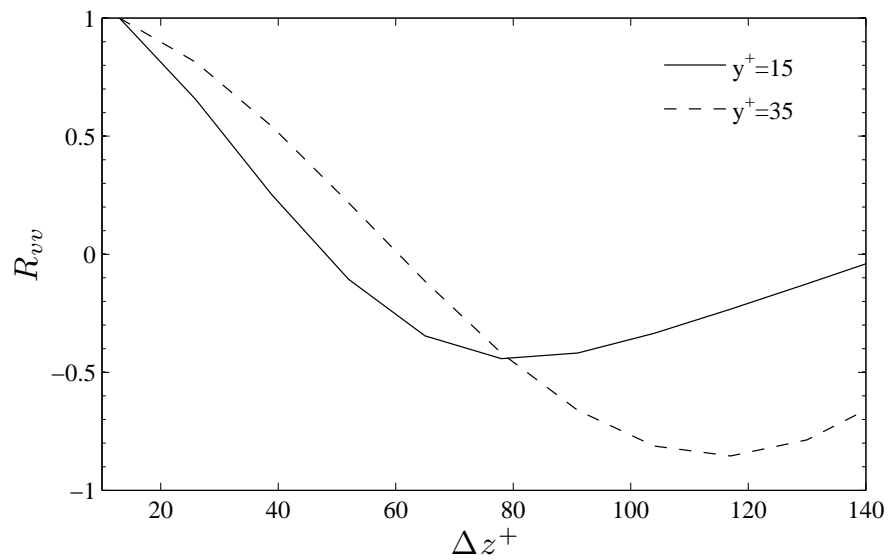
(b)

Figure 4.8: Time-averaged auto-correlation of (a) streamwise velocity perturbations u' and (b) flow-normal velocity perturbations v' at $y^+ = 40$ above the flat plate

Chapter 5

Cavity flow

This chapter reports the CFD model and LES simulation results of a rectangular open cavity-flow at a low Mach number and with a thick inflow boundary layer.

Section 5.1 introduces the flow parameters. In Section 5.2 the computational domain geometry and the mesh are presented, and in Section 5.3 the boundary conditions and the starting flow condition are detailed. This cavity model was designed using the method of Chapter 3 that provided an *a priori* estimate of the computational resources. These estimations are verified *a posteriori* in Section 5.5 from the actual cost of the computation. The scalability performance of the cavity-flow computation is presented in Section 5.4. Finally, the LES simulation results and their comparison with the experimental results of Haigermoser (2009), are detailed in Section 5.6.

5.1   Flow conditions

The flow conditions of the numerical work of this thesis are in dynamic similarity with the experimental work of Haigermoser (2009), based on the Reynolds number. The PIV experiments on a rectangular cavity were formerly used as an idealized geometry test-case to model a real-life automobile bodywork recess by FIAT of a fixture having the typical sizes of a hatch back door cavity at a cruise speed of 140 Km/h (Ribaldone *et al.*, 2005).

The dynamic similarity of the cross-investigation enables the comparison of the numerical LES computation results against the tomographic PIV experiments, throughout this chapter.

Cavity flow parameters	LES	PIV
L/D	4	4
L/W	0.8	0.115
δ_c/D	2	2.11
Re_L	≈ 15500	≈ 16000
M	≈ 0.126	≈ 2.7 E-04
Re_{δ_0}	≈ 5200	-
Re_{θ_0}	≈ 570	-
$Re_{\delta_0^*}$	≈ 720	-
Re_{δ_c}	≈ 7750	≈ 8440
Re_{θ_c}	≈ 920	≈ 900
$Re_{\delta_c^*}$	≈ 1115	≈ 1360

Table 5.1: Cavity-flow conditions and geometrical parameters.

The cavity-flow conditions are summarized in Table 5.1, for the presented LES numerical computation and the PIV work.

5.2   Computational domain geometry and mesh

The computational domain geometry is sketched in Figure 5.1. It is made by four computational blocks: the inlet section (zone 1), a block above the cavity (zone 2), the outlet section (zone 3), and the cavity enclosure (zone 4).

The dimensions of each block are reported in Table 5.2, normalised in terms of the boundary layer thickness at the cavity leading edge δ_c and of the cavity length L. The streamwise dimension of the cavity inflow of $37.7\delta_0$ is slightly larger than the $37\delta_0$ of the inflow test case of Chapter 4, to match the $Re_{\theta_c} \approx 930$ and $Re_L \approx 16000$ inflow conditions of Haigermoser (2009), where δ_0 is the same inlet boundary layer thickness value of Chapter 4. The spanwise and the wall-normal dimensions of blocks 1,2, and 3 are the same of the inflow test case.

The last four columns of Table 5.2 summarize the mesh density in the three directions and the total number of cells. The cavity inlet mesh spacing is the same of the inflow test case of Chapter 4 in the spanwise and wall-normal direction. In the streamwise direction, a constant spacing of $\Delta x^+ \approx 36$ is used for the first 152 cells (up to $X = 22\delta_0$), and a negative stretching ratio of about 5% is used to cluster the cells near the upstream top cavity edge. The dimension of the last cell of the inlet section at the upstream cavity

Zone	DS_x	DS_y	DS_z	$N_{c,x}$	$N_{c,y}$	$N_{c,z}$	$N_{c,tot}$
1	$37.7\delta_0$ $23.6\delta_c$ $11.8L$	$7\delta_0$ $4.4\delta_c$ $2.2L$	$4\delta_0$ $2.5\delta_c$ $1.26L$	196	86	72	$\approx 1.21 \times 10^6$
2	$3.2\delta_0$ $2\delta_c$ L	"	"	128	"	"	$\approx 0.79 \times 10^6$
3	$9.6\delta_0$ $6\delta_c$ $3L$	"	"	"	"	"	"
4	$3.2\delta_0$ $2\delta_c$ L	$0.8\delta_0$ $0.5\delta_c$ $0.25L$	"	"	"	"	"

Table 5.2: Cavity model computational domain dimensions and grid density.
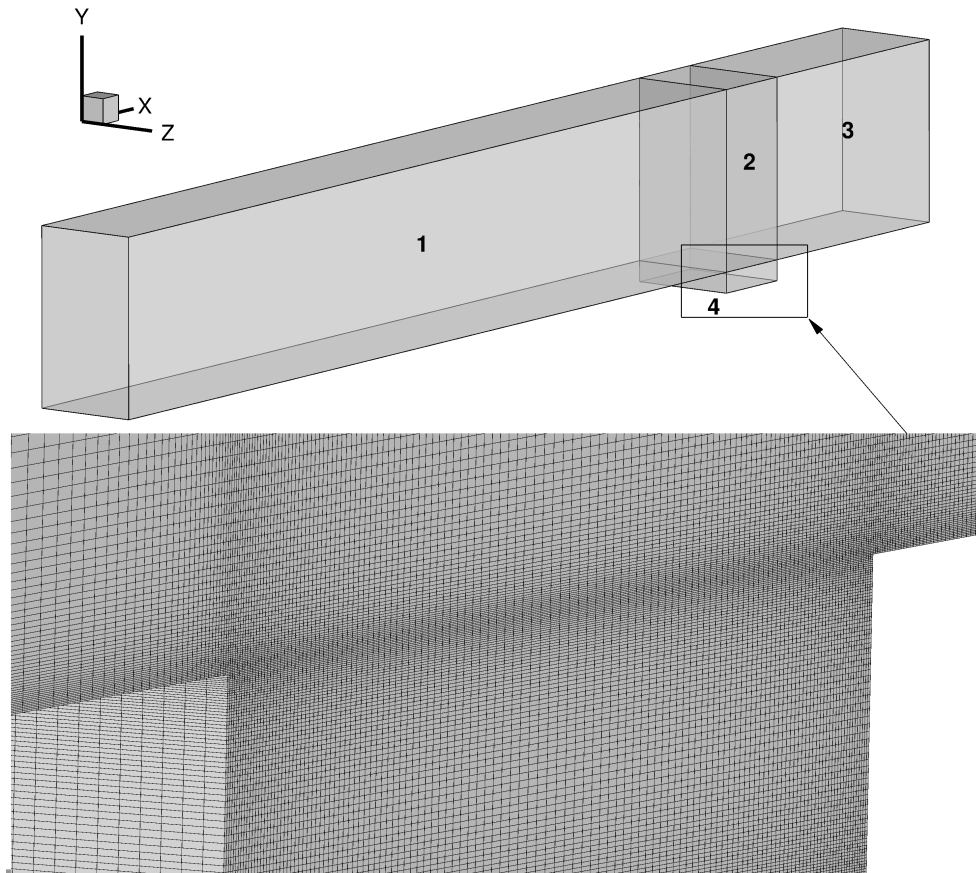
Figure 5.1: Cavity-flow computational domain and detail of the cavity recess.

edge is $\Delta x = 1y^+$. This matches the dimension of the first cell near the upstream bottom cavity edge. An enlargement of the cavity mesh at the intersection of the four cavity blocks around the cavity is also given in Figure 5.1.

A constant stretching ratio of 2.3% is used in the streamwise direction of the cavity from the cavity forward and backward vertical walls towards the centre of the cavity. Similarly, a constant stretching ratio of 3.7% is used in the vertical direction towards the centre of the cavity. Finally, a constant stretching ratio of 2.4% is used in the streamwise direction from the downstream cavity edge to the computational domain outflow. At the downstream top cavity edge, the first cell $\Delta y = 1y^+$.

The total number of cells for the cavity-flow test case is $N_c \approx 3.6 \times 10^6$ cells, with a number of cells in the cavity $N_{c,cav} \approx 0.79 \times 10^6$.

5.3   Boundary conditions and starting flow conditions

The boundary condition used in the cavity-flow simulation at the computational domain inflow (zone 1) is the SSTD boundary condition of Section 2.4. Non-slip adiabatic wall conditions are applied at the solid walls of zones 1, 3 and 4, extrapolation from the inner cells is used at the outflow boundary of zone 3, a non-reflecting condition is used at the upper boundaries of zones 2, 3 and 4, periodic boundary conditions are imposed at the lateral boundaries in the spanwise direction of the domain for zones 1 to 4. Since periodicity was introduced at the lateral boundaries of the cavity domain, the effect of the cavity lateral walls was not modelled and the simulation can be referred to a *pseudo-two dimensional* cavity-flow. Internal connectivities were adopted for the internal boundaries, edges, and corners in the adjoining regions of the computational domain.

The cavity inlet (zone 1) initial velocity field and profile of the turbulent kinetic energy $\bar{k}$, were primed using the same approach as the inflow test case, described in Section 4.3. Zones 2 and 3 were primed using the mean profiles of the outflow boundary of zone 1. In the cavity enclosure, the stagnation flow condition was imposed at the starting time of the computation.

5.4 Parallelization performance

Preliminary scalability tests for the cavity-flow simulation were performed for assessing the CFD scheme MPI parallelisation performance on both the HPC Intel cluster Alice of the University of Leicester, Great Britain, and on the IBM-SP6 IBM cluster of the HPC centre CINECA, Italy. Results of the tests are shown for code speed-up, Equation (5.2(a)), and for parallelisation efficiency, Equation (5.2(b)).

Results of the scalability performance analysis obtained for the RDD parallelisation algorithm of Section 2.5 on the 3.6×10^6 cell LES cavity model are presented in Figure 5.2. The ideal speed-up corresponds to the straight black line $S = N_P$ in Figure 5.2(a). For a number of processors $N_P \lesssim 60$ the speed-up of the SP6 cluster in Simultaneous Multi Thread (SMT) mode is higher than the speed-up achieved by the Alice cluster. For a number of processors $N_P \gtrsim 60$, the Intel cluster Alice reaches an higher speed-up, as also shown by the slope of the dashed blue line.

The better performance of the Intel cluster Alice for a number of processors $N_P \gtrsim 88$ is also confirmed by the higher values of the parallelisation efficiency μ_P, which is higher than the μ_P for the SP6 cluster at $N_P > 88$.

The optimal number of processors, taking into account the expected queue time, CPU time, and wall time constraints on the Alice cluster, was determined as $N_P = 128$. In this configuration, the speed-up was $S_{128} \approx 24.4$, the parallelisation efficiency $\mu_{128} \approx 0.19$ and the parallel computation wall time for one complete Runge-Kutta time integration $T_{128} = 4.1$ seconds. The computational domain flow-through time was equivalent to 0.29×10^6 iterations. Since in a typical LES computation the initial transient needs at least three flow-through times to complete (Tessicini *et al.*, 2006), the total CPU time for the simulation running on 128 processors was 135.3×10^3 CPU hours and the wall time was 1060 hours (≈ 44 days).

The scalar time needed to perform one time step (two Runge-Kutta sub-iterations) using the serial code on a single processor of the cluster in this simulation was $T_0 = 100$ seconds. Hence, the total time to run this simulation on a single processor would have been approximately 3 years.
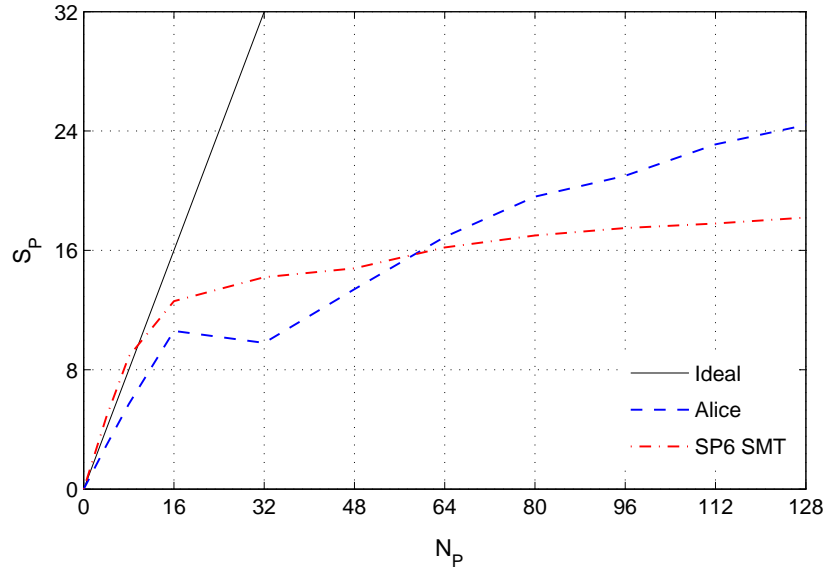
(a)
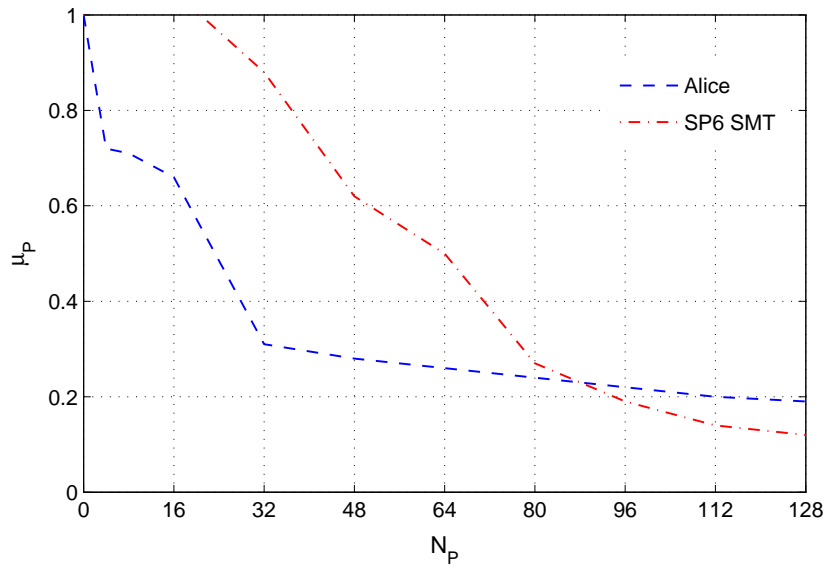
(b)

Figure 5.2: Scalability and parallelisation performance of a four block 3.6×10^6 cells LES cavity model on the HPC Intel cluster Alice and IBM SP6. (a) Speed-up S_P and (b) parallelization efficiency μ_P versus the number of processors N_P.

5.5   Numerical model design predictions

The methodology of Chapter 3 is herein applied to the cavity test case of Section 5.2. The cavity geometry is $L/D = 4$ and $D/\delta = 2.2$. The indicator of the turbulent flow discretization LN_d is first derived from Equations (3.16) and (3.17). The second order scheme determines $PPW = 10.3$ and $r_\tau = 10$, for a spatially resolved WR-LES. The mesh height is so that $n_{D,W-N} = 8.75$ and, from Equation (3.17), $C_1 \approx 0.02$.

At the cavity $Re_L \approx 15500$, for $C_1 \approx 0.02$, Equation (3.16) gives a spectral width of $LN_d \approx 2$. Figure 5.3 shows a verification of this *a priori* estimate of cavity simulation spectral width. At $Re_L = 15500$, the line $C_1 = 0.02$ is vertically intercepted near value $LN_d \approx 2$, in agreement with the value obtained from Equation (3.16).

The analysis is then extended to the cavity-flow mesh density. Since the cavity-flow model uses a WR-LES mesh of $N_c = 3.6 \times 10^6$ cells with a near-wall clustering to $\Delta y^+ \approx 1$, Equation (3.25) is used to obtain $C_4 \approx 0.18$. Figure 5.4 shows where the current $N_c = 3.6 \times 10^6$, $Re_L \approx 15500$ cavity-flow simulation lies with respect to the body of past flow models from the literature in the (Re_L, N_C) plane.

This cavity-flow simulation, marked by an asterisk in Figure 5.4, lies between the clusters of past LES and DNS. This suggests that the coefficients C_3 and C_4 used in Equations (3.24) and (3.26) may not give accurate *a priori* predictions for the current cavity model, as their use implies a degree of extrapolation from the LES and DNS simulation clusters reported in the literature.

A new class of isolines for highly resolved LES cavity-flow simulations might be derived as the number of the WR-LES in literature increases. However, for the time being, the present simulation is the first 3D WR-LES open cavity-flow simulation with a thick inflow boundary layer and mesh sizing between typical LES and DNS values reported in the literature.

Figure 5.5 shows the *a priori* estimate of the current cavity-flow simulation in the context of the cost estimate of previous simulations reported in the literature. In this figure, the current cavity-flow simulation is positioned in a region in-between the typical cost ranges for LES and DNS simulations.

The cost of the present simulation is estimated from Equation (3.30) for $N_C = 3.6 \times 10^6$, which gives $\overline{Cost} \approx 0.56 \times 10^9$.
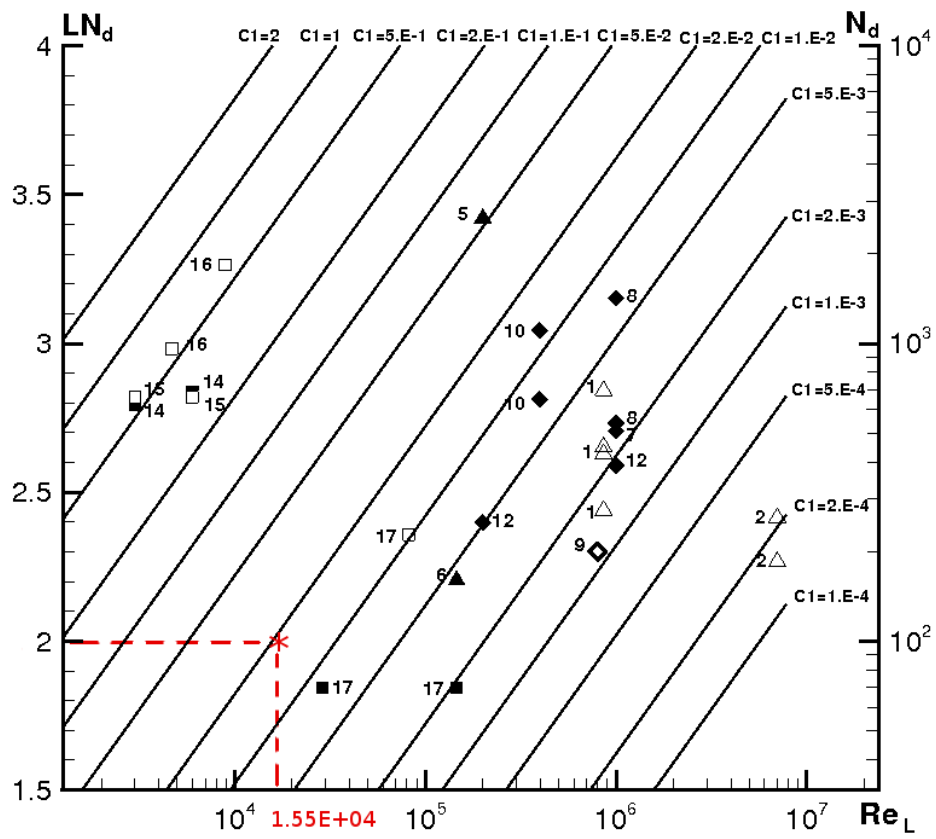
Figure 5.3: *A priori* estimate of the cavity-flow simulation spectral width. Symbols as in Figure 3.2.
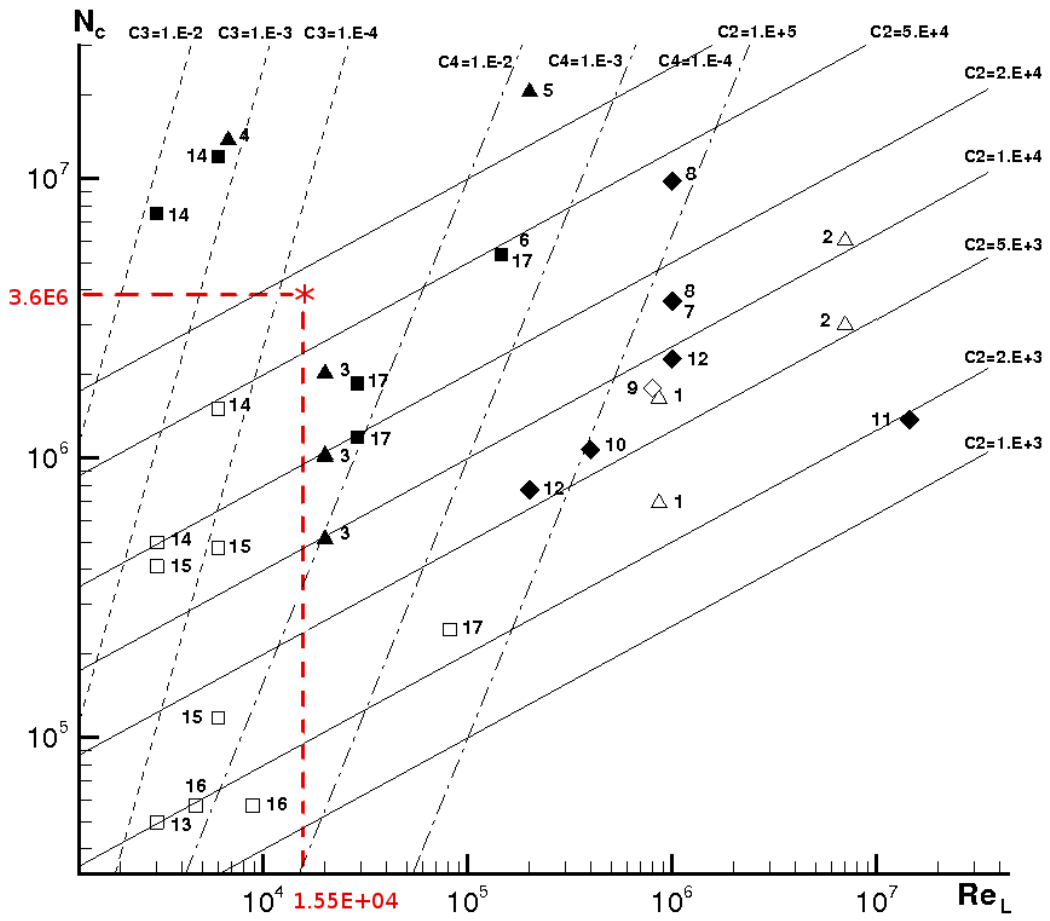
Figure 5.4: Analysis of the cavity-flow grid density. Symbols as in Figure 3.3.
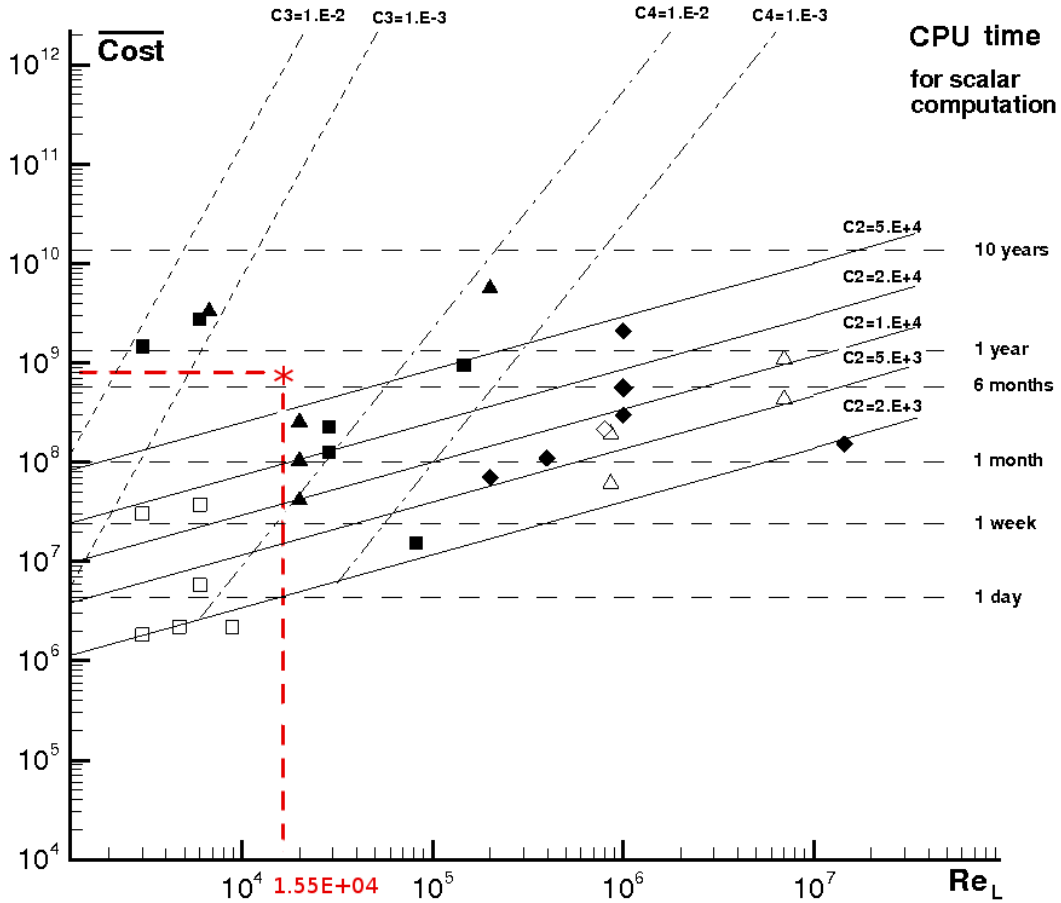
Figure 5.5: Analysis of the cavity-flow grid density. Symbols as in Figure 3.3.

By Equation (3.31), the estimated equivalent run time for a scalar computation of the cavity-flow for $\mu_{128} \approx 0.19$ (Section 5.4, Figure 4.1) is of the order of 262 days $\approx$ 0.7 year, which is in fair agreement with the 0.9 years needed for resolving one flow through time of the cavity-flow WR-LES on a single processors, or the 44 days on 128 processors, using the Alice HPC Intel cluster, reported in Section 5.4.

5.6 Results

In this section, the results of the cavity-flow LES computation are presented and compared against the PIV experiments of Haigermoser *et al.* (2008) and of Haigermoser

(2009). The mean flow field and its statistics are discussed in Sections 5.6.1 and 5.6.2, respectively. The time dependent instantaneous flow fields are shown in Section 5.6.4, and the unsteady flow statistics are detailed in Section 5.6.4. Finally, Section 5.6.5 presents the spectral analysis of the time-resolved flow.

5.6.1 Mean flow field

Figure 5.6 presents the time-averaged velocity field in the vertical x-y plane, in terms of the streamwise velocity vector profiles and velocity streamlines. In Figure 5.6(a), the LES mean streamwise velocity vector field indicates the presence of a large standing vortex that dominates almost the 75% of the cavity length, from $x/L \approx 1$ to $x/L = 4$. This structure is also identified in the PIV The velocity streamlines from the LES numerical predictions in Figure 5.6(c) and PIV experiments in Figure 5.6(d) indicates the location of the centre of the standing vortex at $x/L \approx 3.2$. A secondary weaker counter-re-circulating zone, that was evident in the PIV experiments close to the upstream cavity edge at $x/L \approx 0.4$, appears in the LES results under the form of a lower intensity spiral re-circulation, induced by the velocity field of the primary vortex. This secondary re-circulation was not always reported in previous experiments in literature, like in Grace *et al.* (2004). The impingement of the mean shear layer on the upper part of the front facing step looks more pronounced in the LES results, where a sharp change of direction of the streamlines near the downstream top-cavity edge is visible, as shown in Figure 5.6(c). This is likely to be due to the near wall clustering in the LES providing a higher spatial resolution in this region than PIV, which is limited by the wall light reflections.

Figure 5.7 shows the velocity streamlines of a horizontal x-z plane inside the cavity enclosure at $y/H = -0.5$. The LES simulation predictions are shown in Figure 5.7(a) and the PIV experiments are shown in Figure 5.7(b). In the PIV results, the flow shows a small spanwise velocity component that is attributed to the no-slip wall boundary conditions at the cavity side walls in Haigermoser *et al.* (2008).

In the LES simulation, the presence of spanwise periodic boundary conditions introduces a spanwise velocity component, as evidenced by the orientation of the streamlines at the centre of the cavity enclosure. Two accumulation lines are present, at $x/H \approx 0.2$ and at $x/H \approx 3.2$, respectively. These two lines confirm the presence of the

(a)

(b)

(c)

(d)
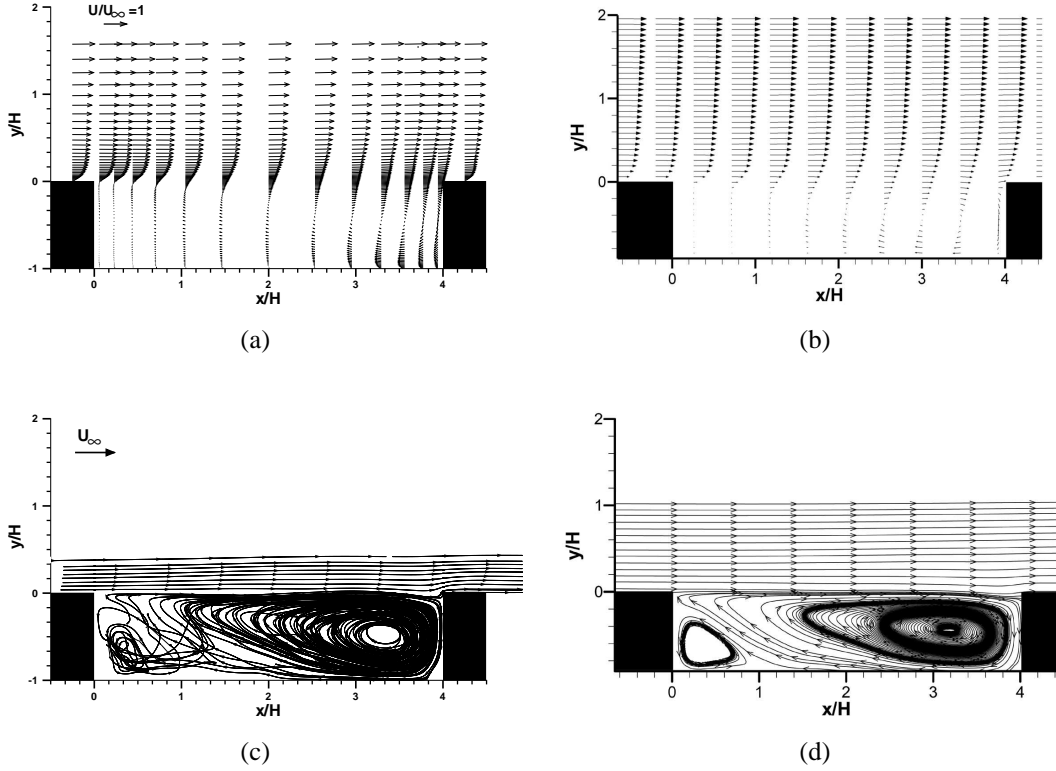
Figure 5.6: Mean field visualizations in the vertical x-y plane. Streamwise velocity vector profile from (a) LES, and (b) PIV experiments by Haigermoser (2009). Velocity streamlines from (c) LES, and (d) PIV experiments by Haigermoser (2009).

primary standing vortex core and of the secondary upstream re-circulation. A result similar to the one from the current LES predictions was obtained by Bissessur *et al.* (2004) from a three-dimensional DES simulations of a rectangular cavity driven by a thin inflow boundary layer.

The time-averaged development of the shear layer along the cavity opening can be described by the vorticity thickness

$$\delta_v(x) = \frac{U_2 - U_1}{(\frac{\partial \bar{U}}{\partial y})_{max}} \tag{5.1}$$

where the cavity external flow velocity $U_2 = U_{\text{inf}}$ and the velocity inside the cavity U_1 is assumed to be equal to zero.

The curve of $\delta_v(x)$ normalized by the momentum thickness θ_c of the incoming bound-

71
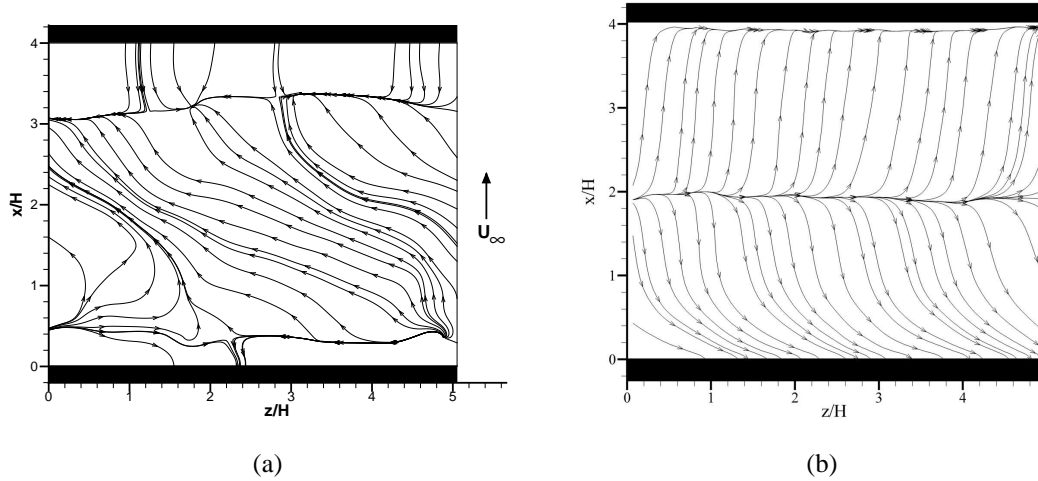
Figure 5.7: Mean field visualizations in the horizontal y-z plane at $y/H = -0.5$. Velocity streamlines from (a) LES and (b) PIV experiments by Haigermoser (2009).

ary layer, is plotted by the red circles in Figure 5.8.

The shape of the vorticity thickness profile is in good agreement with the experimental PIV data, shown by the black stars in Figure 5.8. For both investigations, the growth of $\delta_v(x)$ is linear over most of the length of the cavity. However, the LES results show a steeper growth after the cavity upstream edge, up to $x/H \approx 0.2$. A possible explanation of this higher vorticity thickness growth rate is provided later in Section 5.6.3, where the flow mechanics of the streaks at the upstream cavity edge is detailed. The maximum value of the vorticity thickness is reached at $x/H \approx 3.3$, both for LES and PIV. This maximum for the LES is lower lower by approximately 5% respect the PIV experiments of Haigermoser (2009). As a result, the LES vorticity thickness growth rate calculated from the cavity leading edge to the vorticity thickness maximum value is $\frac{d\delta_v}{dx} \approx 0.28$, while the value obtained from the PIV experiments $\frac{d\delta_v}{dx} \approx 0.30$. These values are driven by the thickness of the incoming boundary layer being large, as typical values thin boundary layers in low Mach number cavity-flows in literature are in the region of $\frac{d\delta_v}{dx} \approx 0.12 - 0.14$ (Ashcroft & Zhang, 2005).

In order to assess the self-similarity of the streamwise velocity profiles across the cavity opening, the non-dimensional variable $\xi = y/(0.5\delta_v)$ is introduced. The non-dimensional velocity profiles $U(\xi)/U_\infty$ are plotted versus ξ in Figure 5.9. The contin-
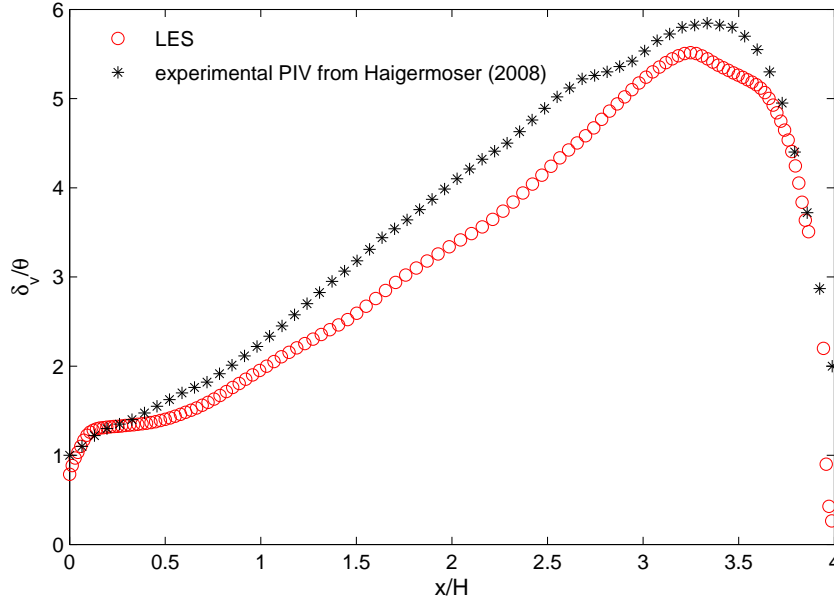
Figure 5.8: Normalised shear layer vorticity thickness as a function of streamwise coordinate x/H.

uous black line represents the streamwise velocity profile analytical law of a canonical free-shear layer

$$\frac{U(\xi)}{U_\infty} = \frac{1}{2}[1 + \tanh(\xi)] \tag{5.2}$$

The outer layer region is near $U(\xi)/U_\infty = 1$. In this region, as the flow goes downstream over the top of the cavity opening, the velocity profile tends to become self-similar, which increases the wake parameter Π in Equation (2.45) in the outer layer. In the inner layer region, near $U(\xi)/U_\infty = 0$, the self-similarity is only approximately reached in the upstream region of the cavity, at $x/H = 0.5$ (green circles) and $x/H = 1.5$ (cyan triangles), since significative velocity values are induced by the bound vortex in the downstream cavity region, as shown by profiles at $x/H = 2.5$ (blue squares) and at $x/H = 3.5$ (magenta crosses).
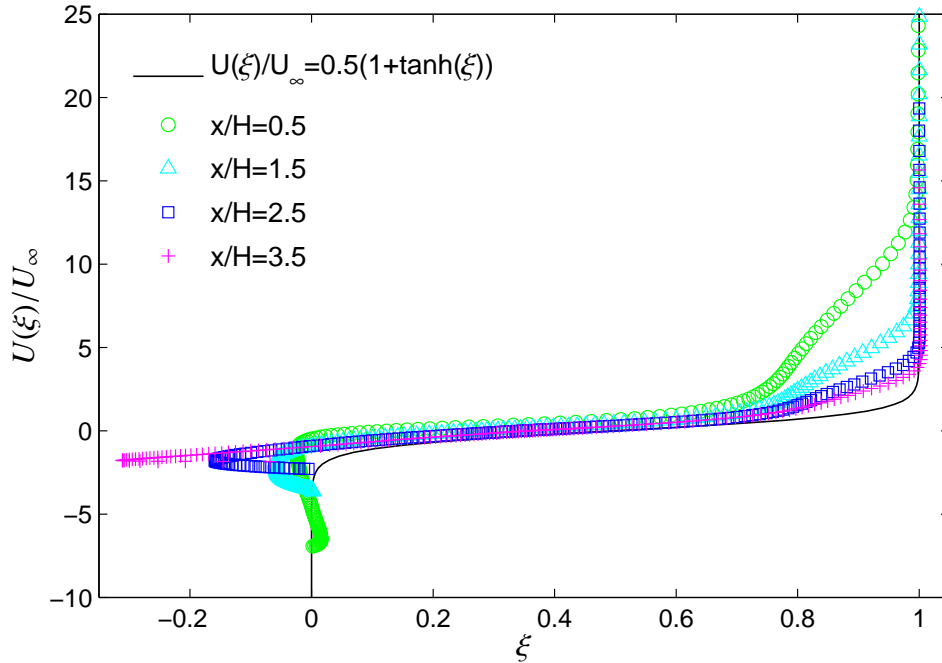
Figure 5.9: Non-dimensional time-averaged streamwise velocity profiles at different streamwise locations, across the rectangular cavity opening.

5.6.2   Mean flow statistics

In order to characterize the spatial scales of the eddies contained in the turbulent shear layer of the cavity, the two-point spatial correlation function $\rho_{u'u'}$ of the streamwise velocity fluctuations u', obtained from the LES simulation, was computed at three reference points on the cavity centreline at $x_{ref}/H = 0.6$, $x_{ref}/H = 2$, $x_{ref}/H = 3$. The results are presented and compared against the PIV experiments by Haigermoser (2009) in Figure 5.10.

Figure 5.10(a) shows that near the upstream top cavity edge, at point $x_{ref}/H = 0.6$, $y_{ref}/H = 0$, the shape of the correlation function is elongated in the streamwise direction, due to the streamwise coherence of the spatial scales in the turbulent boundary layer approaching the cavity mouth. A smaller positive correlation spot is shown at a streamwise distance $2H$ from the reference point, identifying the convection of turbulent structures across the cavity. This is in agreement with the PIV results shown in Figure 5.10(b), in which a broader second region of $\rho_{u'u'} \geq 0.5$ correlation is shown
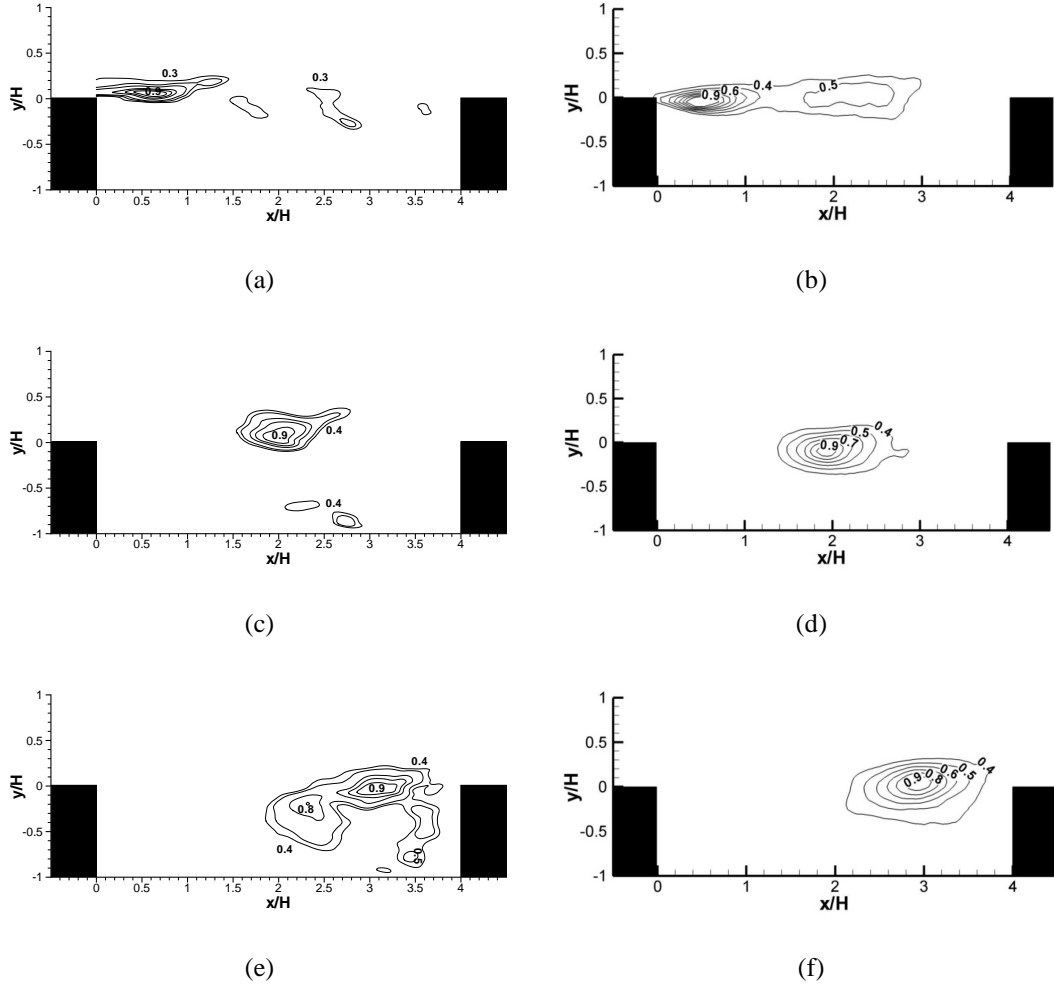
Figure 5.10: Two-point spatial correlation function $\rho_{u'u'}$ computed at three reference points from the LES and PIV time-resolved velocity data. (a) LES, $y_{ref}/H = 0, x_{ref}/H = 0.6$. (b) PIV, $y_{ref}/H = 0, x_{ref}/H = 0.6$. (c) LES, $y_{ref}/H = 0, x_{ref}/H = 2$. (d) PIV, $y_{ref}/H = 0, x_{ref}/H = 2$. (e) LES, $y_{ref}/H = 0, x_{ref}/H = 3$. (f) PIV, $y_{ref}/H = 0, x_{ref}/H = 3$. Contours with constant increments of $\Delta\rho_{u'u'} = 0.1$.

spanning a larger portion of the cavity, up to $x/H = 3$. In the middle of the cavity mouth in Figure 5.10(c), the two-point spatial correlation function $\rho_{u'u'}$ referenced to point $x_{ref}/H = 2, y_{ref}/H = 0$ shows a region of $\rho_{u'u'} \geq 0.5$ that is wider in the wall-normal direction with respect to Figure 5.10(a). This is due to the growth of the shear layer that accommodates thicker self-coherent structures. For the last reference point, $x_{ref}/H = 3, y_{ref}/H = 0$, Figure 5.10(e) shows that the two-points correlation function

$\rho_{u'u'} \geq 0.4$ over the rear half of the cavity, where coherent structures are convected and then feed in the main re-circulation, characterized by the standing vortex.

A more detailed explanation on the dynamics of the turbulent structures into the cavity will be presented in the section dealing with the time-dependent flow field, Section 5.6.3. The PIV experiment results in Figure 5.10(d) and 5.10(f) shown a similar circular region for the function $\rho_{u'u'}$ centred about the same reference points, although the LES simulation evidenced a more irregular shape of the correlation function due to the higher spatial resolution of the non-uniform numerical mesh, as compared to the uniform PIV vector grid.

The two-point correlation function $\rho_{v'v'}$ for the vertical velocity fluctuations v' is presented in Figure 5.11 and compared versus the PIV experiments at the same reference points along the cavity centreline at $x_{ref}/H = 0.6$, $x_{ref}/H = 2$, $x_{ref}/H = 3$. The shape of the $\rho_{v'v'}$ contours is more circular for the three reference points in which the correlation function was computed. This reflects the coherent behaviour of single vortices travelling along the shear layer that was shown in the PIV experiments. The correlation function from LES data shows the presence of correlation regions with a larger extent with respect the PIV results. This behaviour is in a qualitative agreement with the study of Ashcroft & Zhang (2005), in which the variation of the transverse integral length scale in the streamwise direction indicates the linear growth of coherent scales of flow-normal velocity perturbation across the cavity open end. The values of the correlation function $\rho_{v'v'}$ predicted by LES are comparatively lower than the corresponding values from PIV, which is probably due to LES resolving in time and space a greater range of structures than with the PIV. The smaller scales are likely to be less coherent, leading to a lower $\rho_{v'v'}$ in the LES predictions.

The distribution of the mean pressure coefficient $C_P = 2(p - p_0)/(\rho U_e^2)$ in the vertical x-y plane, obtained from LES, is shown in Figure 5.12(a) and compared against the PIV results of Figure 5.12(b). The mean pressure distribution from the PIV data was obtained by integrating numerically the incompressible Reynolds Averaged Navier Stokes (RANS) momentum equation on a PIV $u-v$ velocity plane. The inertia, viscous and Reynolds stress terms were calculated from the measured instant velocity field and the pressure is derived through integrating its gradient, as detailed in Haigermoser (2009). In the LES numerical predictions, a large region of negative C_P is visible, whose peak is at $x/H \approx 3$ and $y/H \approx 0.4$, in correspondence of the standing vortex
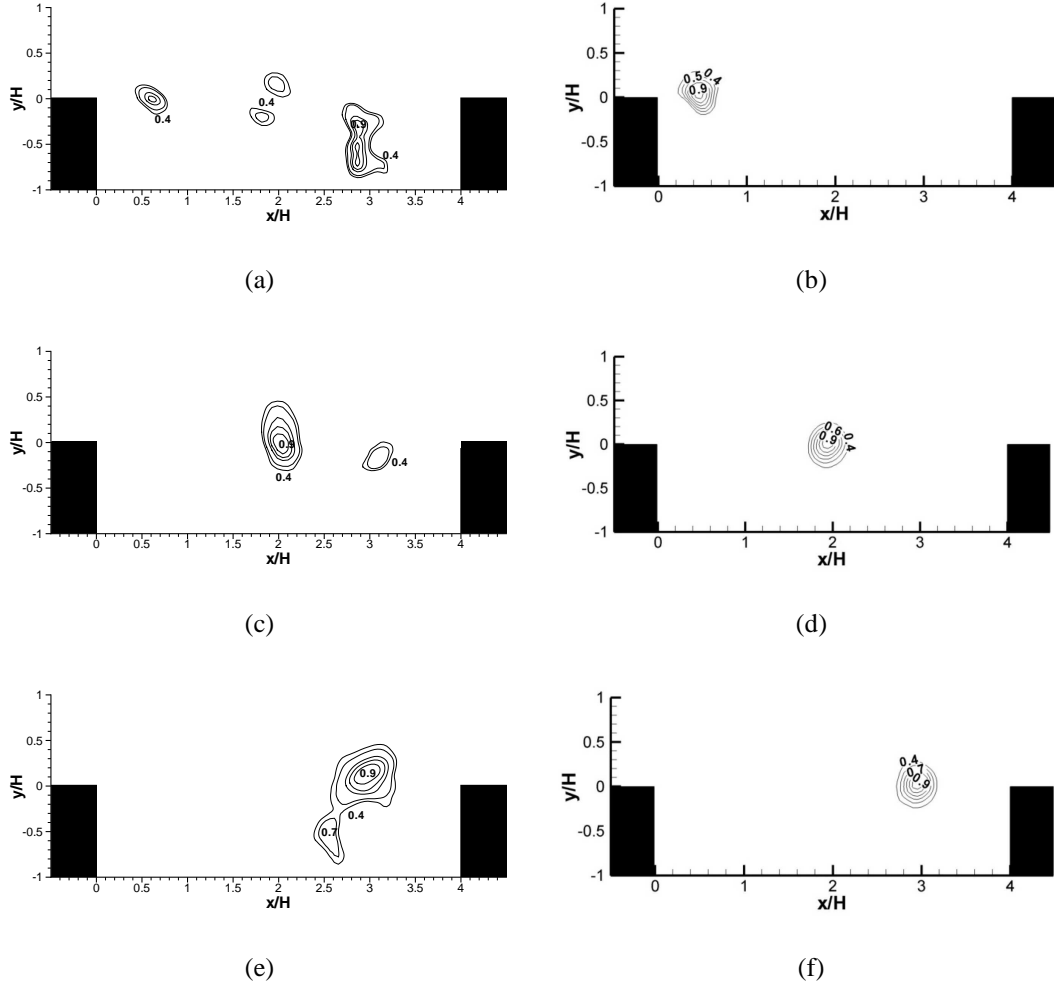
Figure 5.11: Two-point spatial correlation function $\rho_{v'v'}$, computed at three reference points from the LES and PIV time-resolved velocity data. (a) LES, $y_{ref}/H = 0, x_{ref}/H = 0.6$. (b) PIV, $y_{ref}/H = 0, x_{ref}/H = 0.6$. (c) LES, $y_{ref}/H = 0, x_{ref}/H = 2$. (d) PIV, $y_{ref}/H = 0, x_{ref}/H = 2$. (e) LES, $y_{ref}/H = 0, x_{ref}/H = 3$. (f) PIV, $y_{ref}/H = 0, x_{ref}/H = 3$. Contours with constant increments of $\Delta\rho_{v'v'} = 0.1$.

core. Positive values of C_P are visible close the forward facing step. C_P maxima are predicted at the downstream top cavity edge, where the shear layer impinges, and at the cavity downstream bottom edge. Finally, a region of negative C_P is visible downstream of the cavity downstream edge, which results from the local flow acceleration during the mass ejection phase of the unsteady cavity-flow. There is a good qualitative agreement between numerical and experimental results for the mean pressure coeffi-
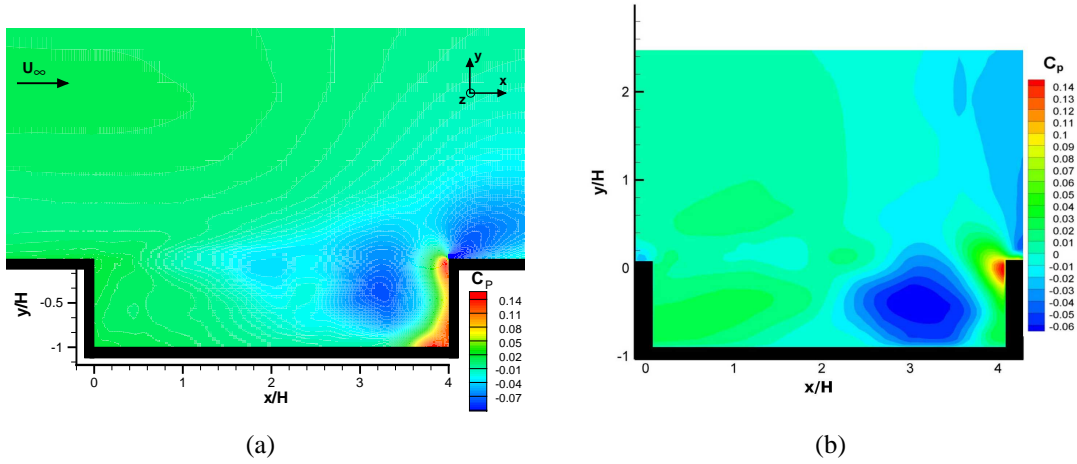
Figure 5.12: Time-averaged pressure coefficient C_P from (a) LES, and (b) PIV experiments by Haigermoser (2009).

cient. The peak of negative pressure is located at the same position in LES and PIV. The only qualitative difference between Figures 5.12(a) and 5.12(b) is in the presence of a C_P maximum that appears only in the LES predictions at the downstream bottom cavity edge.

The mean pressure drag per unit spanwise length can be approximated by:

$$\bar{D} \approx \int_{d.w.} p \cdot dl - \int_{u.w.} p \cdot dl \tag{5.3}$$

where the pressure is integrated along the upstream vertical wall (u.w.) and the downstream vertical wall (d.w.), and computed numerically at a distance $y^+ = 30$ from the walls. The computed mean drag coefficient is $\overline{C_D} = 2\bar{D}/\rho U^2 H = 0.056$. The perfect agreement of the experimental value $\overline{C_D} = 0.056$ obtained from PIV experiments by Haigermoser (2009) is likely to be a fortuitous result, given the difference in predicted pressure iso-levels in Figure 5.12.

5.6.3   Unsteady flow field

The study of the time-dependent unsteady flow fields in this section gives a contribution to the understanding of the flow mechanisms governing the dynamics of the shear layer and the evolution of the coherent structures embedded in the thick boundary layer across the cavity opening, such as convected vortices developing from instabilities,
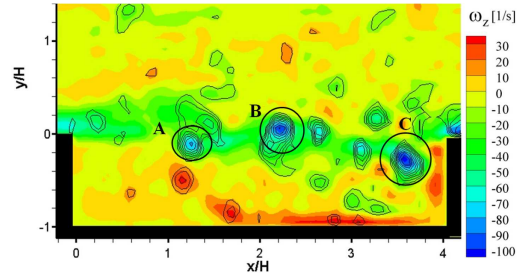
(a)
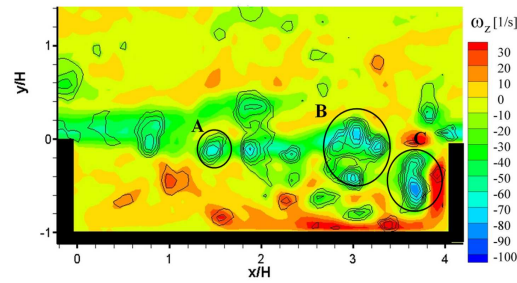
(b)
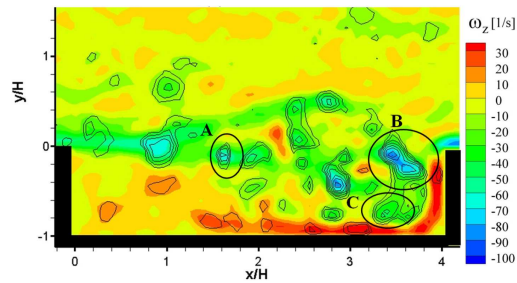
(c)
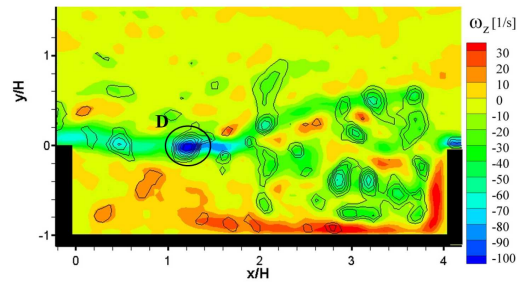
(d)

Figure 5.13: Experimental PIV spanwise vorticity ω_z fields on the vertical x-y plane from Haigermoser (2009).

vortex stretching, vortex pairing, and vortex breakdown. In the literature of cavity-flow at low Mach number and with a thick incoming turbulent boundary layer, the time-resolved tomographic PIV experiments of Haigermoser *et al.* (2008) displayed the dynamics of the different scale vortical structures, detecting the flow complexity connected with the dynamics of the motions in the shear layer and in the main re-circulation zone. The shear layer containing the vortical structures across the cavity opening was observed to have an intermittent behaviour. A detailed analysis of the spanwise vorticity ω_z field and vortical identification of the structures in a vertical x-y plane was performed. The flow visualizations are shown in Figure 5.13. The images correspond to four different time intervals during a complete cavity-flow through time cycle. From observing the time-dependent flow, Haigermoser *et al.* (2008) postulated that the shear layer is populated by two different types of structures. The first structures are vortices formed by the shear layer instabilities, influenced by the incoming turbulent boundary layer. The second type of structures are three-dimensional structures randomly distributed in space and time, originating from the turbulent boundary layer.

The level of detail in space and time of the fine LES computation of this thesis allows one to further understand the origin and the relationship between the type of structures observed in the tomographic PIV experiments. Figure 5.14 presents a sequence of the spanwise vorticity ω_z fields in a vertical x-y plane at six different time steps (equivalent to 0.6 cavity-flow through times) from the LES computation. In Figure 5.14(a), two "swiss roll" eddies, normally present in a typical free shear layer flow like the one of Figure 1.2, are identified by the black outlines. The first structure spans from $x/H =$ 0.8 to $x/H = 1.8$ and the second structure, which is more elongated, spans from $x/H =$ 1.8 to $x/H = 3.2$. In Figure 5.14(b), the structure B of the first roll, that lies in the region above the cavity, moves in the streamwise direction with higher velocity with respect to vortex A, that remains almost in the same position. This is due to structure B being exposed to a higher speed mean flow outside the cavity than structure A. At the same time, a strain region with negative spanwise vorticity C pushes structure B in the wall-normal direction. Both structures D and E from the second roll move toward the main cavity re-circulation. In Figure 5.14(c), vortices A and B are completely separated by the negative vorticity core C. The two rolls D and E are entrained into the standing vortex. In Figure 5.14(d), vortex B has moved further in the streamwise and
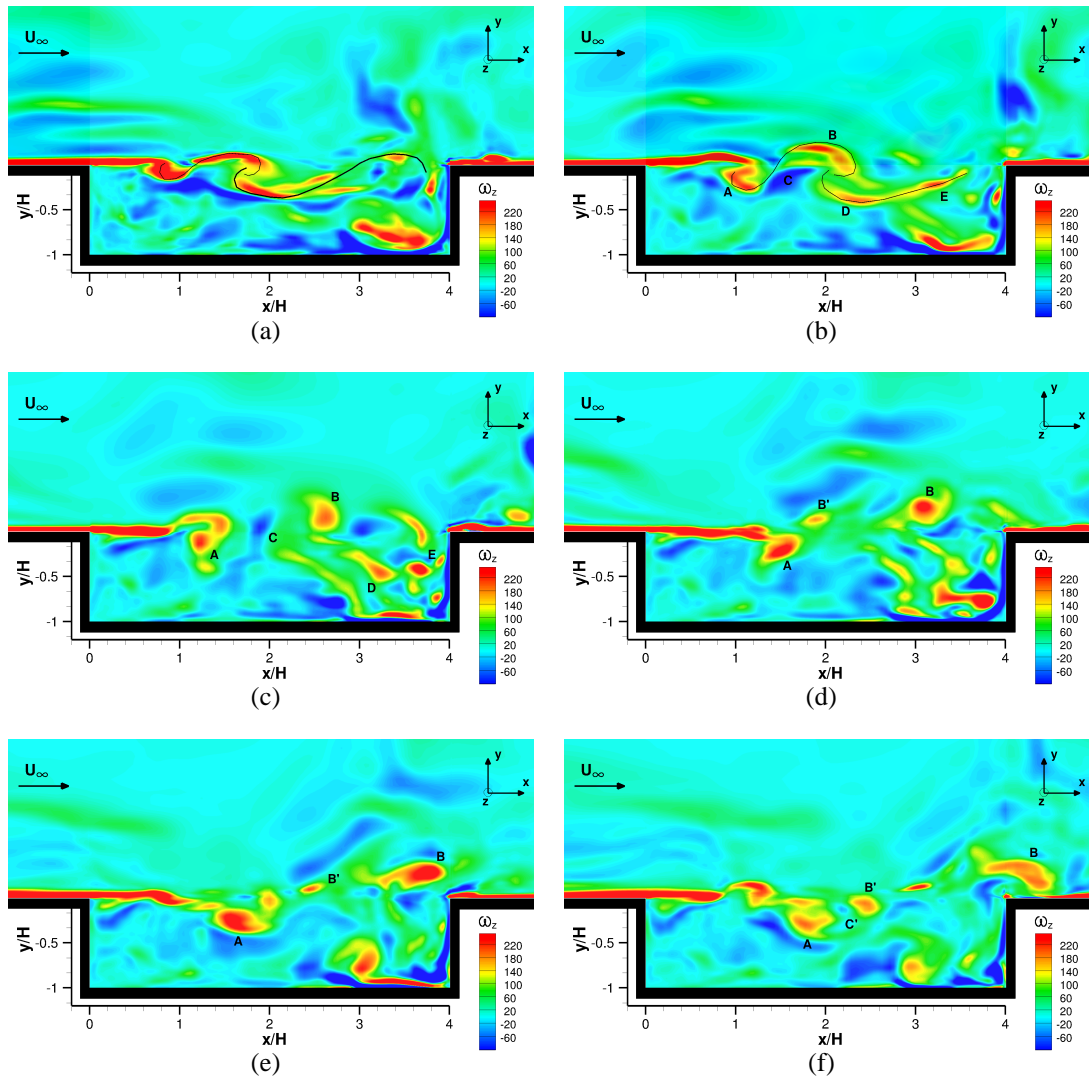
Figure 5.14: Spanwise vorticity ω_z distribution from LES on the vertical x-y plane at increasing computational times. Time increment between two frames is $\Delta t = 0.1$ of the cavity-flow through time.

wall-normal direction. In the region marked with B' a core with positive spanwise vorticity is being convected from the cavity inflow. In Figure 5.14(e), vortex B is being ejected out of the cavity. In the region B' there are alternating positive and negative vorticity cores. In Figure 5.14(f), vortex B has been ejected completely out of the downstream top cavity edge. A new pattern similar to the one of Figure 5.14(b) is noticeable, with a "swiss roll "that is made by the positive vorticity B', a strained vortex C', and the lower vortex A which has moved very slowly during the whole cycle, due to it being confined in a stagnation region between the primary standing vortex and the secondary induced re-circulation located close to the upstream bottom cavity edge.

The analysis of the time-dependent ω_z field confirms the presence of vortices that are generated by the shear layer vortical instabilities and three-dimensional structures, as already pointed out by the PIV tomographic experiments of Haigermoser *et al.* (2008). However, the spatial and temporal resolution of the LES computation enables us to identify the dynamics of coherent flow patterns in the cavity shear layer, which explains the so far undefined coexistence of the two type of structures in the enclosure. The structures can be associated to the approaching boundary layer streaks developing in the downstream region of the cavity and being perturbed by the Kelvin-Helmothz instability. The main field re-circulations shown in Section 5.6.1 determine regions of low and high convection speed that tilt, separate, and convect the vortices initially belonging to coherent patterns toward different paths, depending on their stochastic initial position.

The process shown in Figure 5.14 explains why vortices that are created from the shear layer instabilities at the upstream cavity edge are not always entrained into the cavity, but can either pass over or impinge the top edge of the cavity forward facing step. This explains the intermittent behaviour of mass injection and ejection inside and outside the cavity and the related pressure fluctuation along the cavity walls, which is mainly responsible for noise emission.

The evolution of the longitudinal streaks contained in the turbulent boundary layer approaching the cavity, introduced in Chapter 4, is investigated in the LES results. Figure 5.15 shows a time sequence of the wall-normal vorticity ω_y fields on the horizontal plane at $y/H = 0.05$, at four different time steps (equivalent to 0.4 cavity-flow through times). The flow direction in Figure 5.15 is from bottom to top, as indicated

by the U_∞ arrow. In Figure 5.15(a) the streak A is approaching the cavity. Three-dimensional vortical structures of higher ω_y magnitude, labelled as B and C, convect across the cavity opening downstream of a streak. In Figure 5.15(b) the streaky structures A reaches the cavity upstream edge. The regions of positive ω_y value B and C, in Figure 5.15(a) stretch and tilt in Figure 5.15(b). This confirms the process of vortex shedding, strain and separation presented in the analysis of the spanwise vorticity ω_z in the region $1 < x/H < 2$ of Figure 5.14(a), at the same computational time step.

In Figure 5.15(c), the streak A has gone over the upstream top cavity edge. The head of the streak enlarges its core, and tilts it in the wall-normal direction, as shown by the increase in the ω_y value in Figure 5.15(c) compared to Figure 5.15(b) This excites the shear layer Kelvin-Helmotz type instability that is convectively amplified from this point onwards. A qualitative explanation of this process is presented in the sketch in Figure 5.16 using a potential-flow idealisation. The streak couple is represented by two opposite vortices V1 and V2. Upstream of the cavity leading edge, the resulting effect of the upstream bulkhead on the vortices can be modelled by the method of images using the vortices of the same intensity and opposite sign V3 and V4 located symmetrically about the horizontal wall. At this condition the vortex V1 is subject to three induced velocities U2, U3, and U4, generated by vortices V2, V3, and V4, respectively. The resultant induced velocity varies in time but can be taken as being null, resulting in the streaks being aligned in the streamwise direction, as shown in Figure 5.15 at $x/H < 0$. In the region downstream of the cavity upstream edge, the induced velocity contribution from vortices V3 and V4 is absent. At this condition, vortex V1 is only subject to the vorticity field of V2. The induced velocity U2 lifts V1 in the positive wall-normal direction and initiates the instability that is amplified in the cavity enclosure. The flow dynamics shown above is confirmed by the experimental tomographic PIV results of Haigermoser *et al.* (2008) presented in Figure 5.17.

The sequence of images reproduce the flow organization comprised by low and high speed streaks and vorticity strips at the flanks of them. The conclusion from both the comparison of numerical and experimental results is that thick turbulent boundary layer coherent structures are convected into the shear layer, where the observed streamwise vorticities in PIV is the consequence of the tilting, breakdown, stretching, and pairing interaction in the cavity opening, as identified by the current LES.
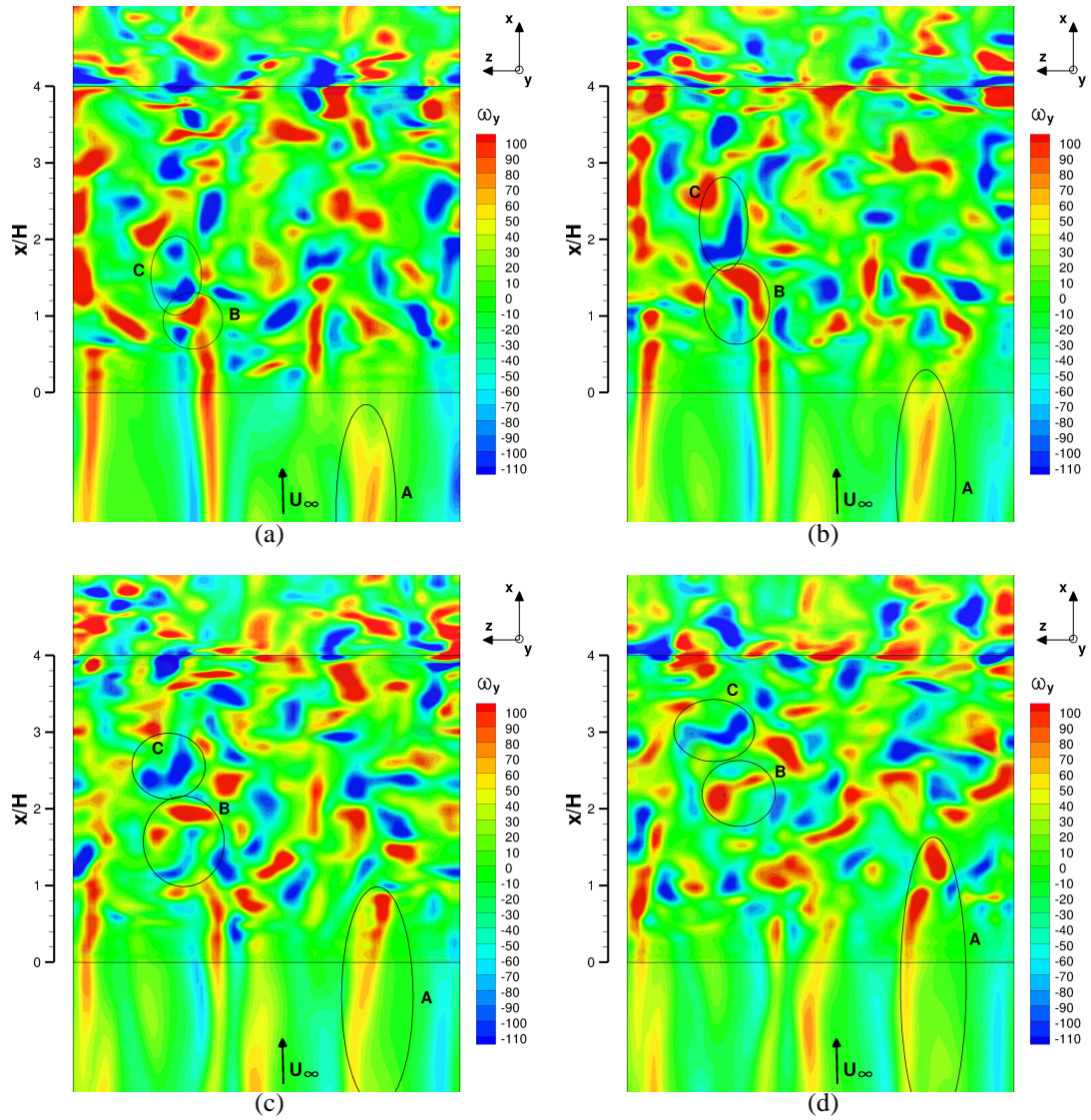
Figure 5.15: Time sequence of wall-normal vorticity ω_y distribution from LES at the horizontal x-z plane $y/H = 0.05$. Incremental time between successive frames $\Delta t = 0.1$ of the cavity-flow through time.

Figure 5.18 shows a snapshot of the vorticity field in the cavity enclosure by the Q vortex identification criterion (Hunt *et al.*, 1988). The vortical structures identified in the iso-vorticity levels of Figures 5.14 and 5.15 are herein rendered in three dimensions. The streamwise bulges in the iso-Q surfaces upstream of the cavity leading edge are associated to the streaks in the approaching turbulent boundary layer. Zones of low streamwise momentum can be identified between streaks, which are likely to be due to the presence of hairpin vortices in the boundary layer. A similar pattern was identified in the PIV experiments of Gottero & Onorato (2000), in which the flow field in the buffer layer of a flat plate was characterised by a streaky configuration, where elongated low speed bands alternate with higher speed regions. The mutual interaction of these quasi-streamwise vortices, convected at different velocities in the near wall region, was related to the presence of localized regions characterized by ejections or sweeps. The structures in the cavity opening can therefore be associated to the hairpin structures existing in the approaching turbulent boundary layer, being convected in the turbulent shear layer and travelling far downstream the cavity upstream edge. Figure 5.19 shows an equivalent flow visualization from the PIV measurements by Haigermoser (2009), in which the iso-surfaces of the absolute vorticity and the horizontal streamwise velocity iso-levels confirm, from a qualitative viewpoint, the predicted flow pattern of Figure 5.18 and supports its interpretation.
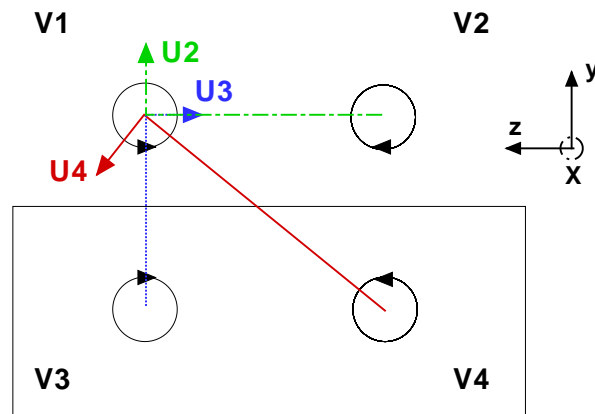
Figure 5.16: Potential-flow description of a streak pair above the upstream cavity bulkhead.
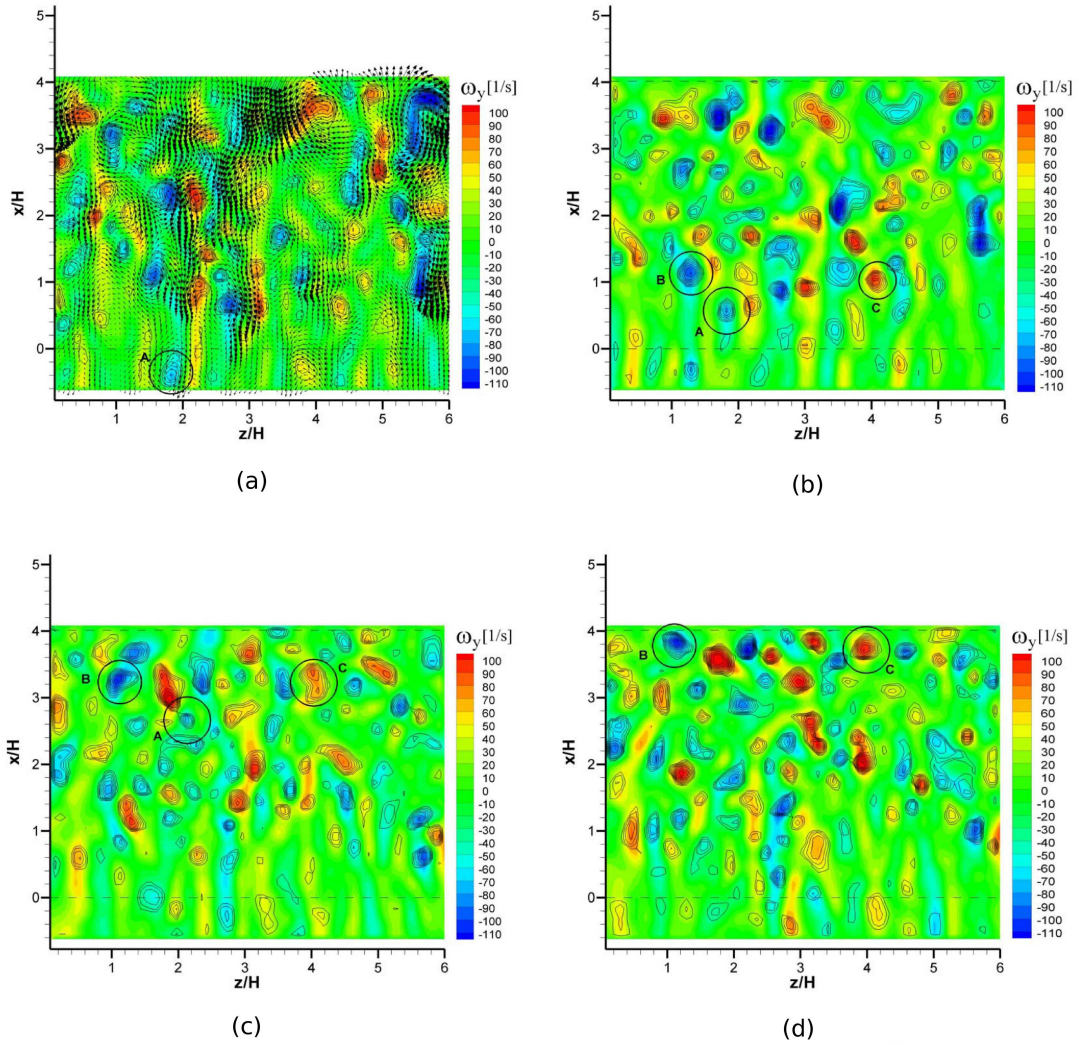
Figure 5.17: Time-sequence of wall-normal vorticity ω_y distribution from PIV on a horizontal x-z plane, from Haigermoser (2009).
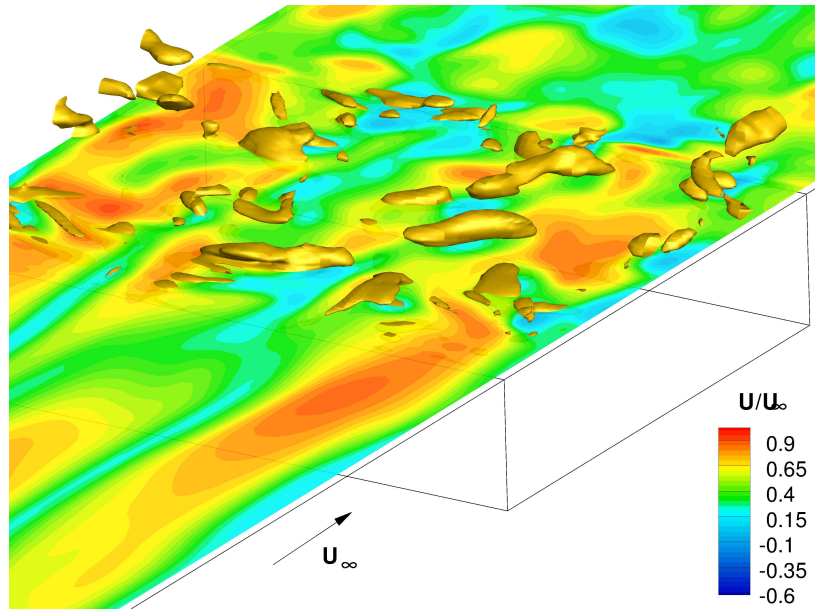
Figure 5.18: Snapshot of *Q*-criterion iso-vorticity surface at $Q = 1.2E+09$, and streamwise velocity slice in the x-z plane. LES computation at time $T = 3$ flow through times.
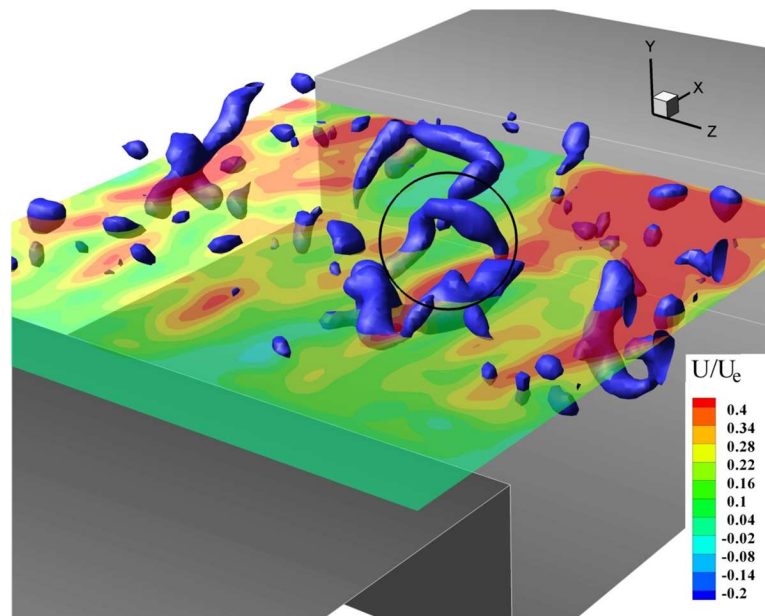
Figure 5.19: Snapshot of absolute vorticity iso-surfaces and streamwise velocity slice in the x-z plane. PIV experiments from Haigermoser (2009). $U_e = U_\infty$.
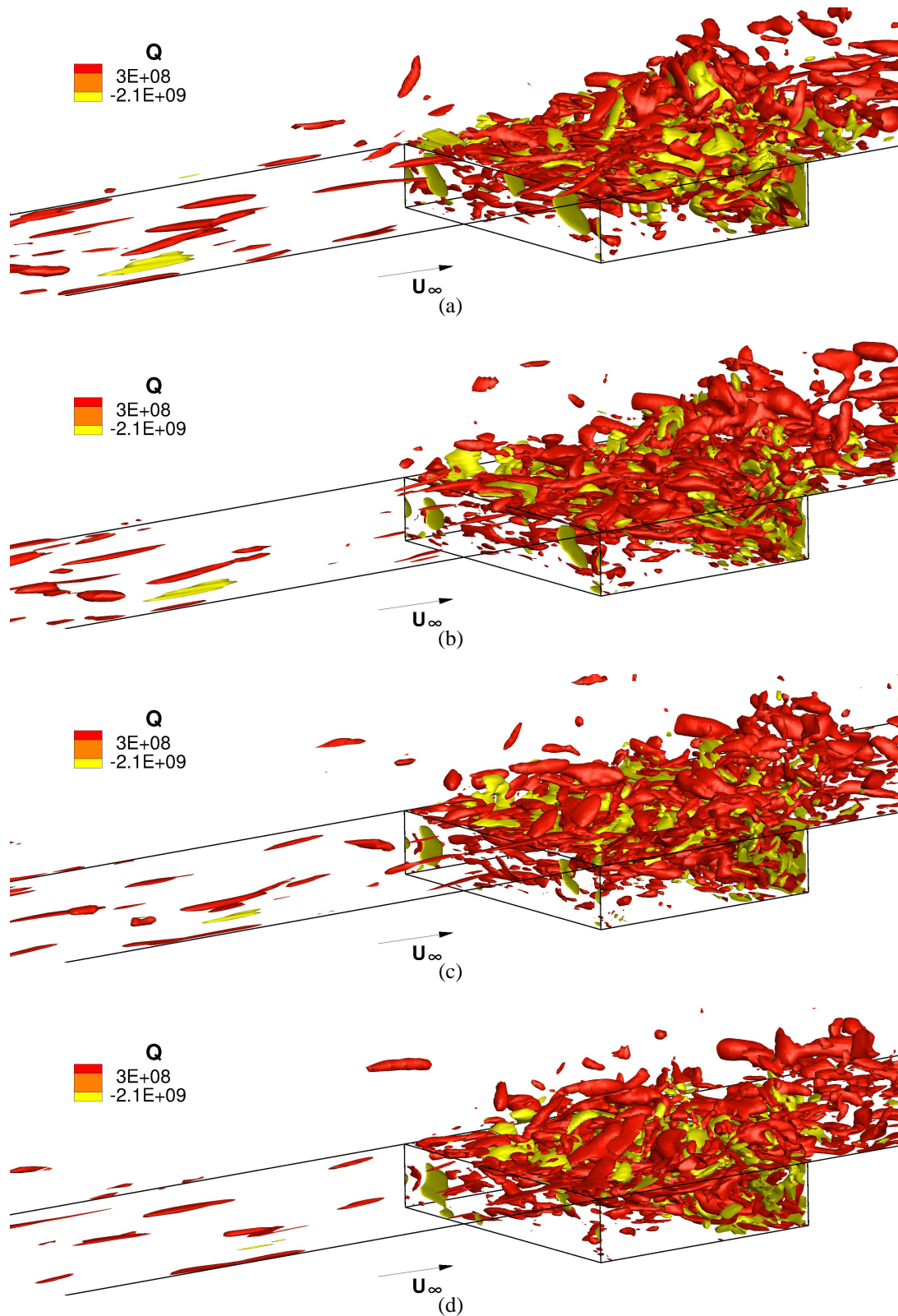
Figure 5.20: Vortex identification by the Q-criterion. Time sequence of iso-contours at $Q = 3.3E + 08$ and $Q = -3E + 09$. The incremental time between two successive frames $\Delta t = 0.1$ cavity-flow through times.

The process of mass injection and ejection into and out of the cavity can be further appreciated in Figure 5.20, where the iso-surfaces of positive and negative vorticity intensity, related to the vortical structures convected in the cavity, are identified by the Q-criterion at the values $Q = 3.3E + 08$ and $Q = -3E + 09$, respectively. The instantaneous flow fields are taken at an incremental time $\Delta t = 0.1$ cavity-flow through times. In the regions in which $Q > 0$ vorticity dominates strain. Regions in which $Q < 0$ are dominated by strain. The intermittent mass flow across the cavity opening is generated as result of the opposite actions of vorticity and strain regions, in which the turbulent scales resulting from the instability processes of vortex interaction, stretching and merging are combined.

5.6.4 Unsteady flow statistics

An auto-correlation analysis allows one to investigate the evolution of the turbulent structures across the cavity opening. Lilley (1996) demonstrated that the value of the longitudinal velocity correlation function relates to the space-time properties of turbulence and to the corresponding acoustic power spectrum function. This assumption follows the more general theory of Lighthill (1952) and Lighthill (1992), in which the the acoustic radiated sound power is determined by the fourth-order space-retarded time covariance. Relationship with the fourth-order space-retarded time covariance gives then an information on the noise sources rather than the output prediction of the noise source itself.

The spanwise auto-correlation function R_{uu} is computed by Equation (4.5) at a distance $y^+ = 15$ from the cavity centreline, for three traverse velocity fluctuations arrays at the streamwise coordinates $x/H = [0.4, 2, 3.6]$. The results from LES are presented in Figure 5.21.

In the thick boundary layer cavity inflow, the streak spacing dictates the spanwise correlation of the velocity fluctuations, with an associated integral length scale proportional to the streak spacing. This is shown in Figure 5.21(a), where the integral length scale $L_u(y) = 2\Delta z_{min} \approx 170$ reasonably matches with the streak spacing distance of $160y^+$ obtained in Section 5.6.4.

Above the cavity, in the upstream portion of the enclosure, streaks spacing breaks down into smaller and less coherent structures, as evidenced by the reduction of $L_u(y) \approx 90$

in Figure 5.21(b). This would lead to a decrement in the acoustic emission, according to the integral formulation of Lilley (1996). However, in the rearmost portion of the cavity above the bound vortex, L_u increases. This correlates with an observed elongation of the wall-normal vorticity ω_y peaks in the spanwise direction in Figure 5.15. This greater spanwise coherence, which by itself would lead to a more effective acoustic emission, is counteracted by the presence of strong negatively correlated velocity fluctuations, indicated by the $R_{uu} \approx -0.5$ minimum in Figure 5.21(c). The positive and negative areas of velocity correlation would emit sound with opposite phase, leading to a dipole-type cancellation in the upstream direction. This supports previous observations for sound measured from three-dimensional cavities being of lower intensity respect to modelled

two-dimensional cavity-flow emissions, in which the the vortex roller hits the downstream cavity edge as a phase-coherent velocity perturbation.

5.6.5   Spectral analysis

To perform a spectral analysis of the time-resolved LES velocity, the predicted velocity history was extracted at the streamwise coordinates $x/H = 1.4$ and $x/H = 2.7$, at a height $y^+ = 80$ and at half of the cavity spanwise dimension $z/W = 0.5$. Velocity values were stored at each time step of the LES computation. From the three velocity components, the spectra of the turbulent kinetic energy were computed using the FFT algorithm by Frigo & Johnson (2005). The TKE power spectral density is plotted versus the Strouhal number $St = fH/U_\infty$ in Figure 5.22. The drop-off of both spectra at $St = 6$ is due to the start of the numerical dissipation of the mesh resolution at the high enf of the frequency domain.

Both spectra do not display a clearly identifiable spectral peak above the broadband level, which suggests that no tonal instability is present in this flow. This is in agreement with the absence of Rossiter tones for a cavity-flow with a thick incoming boundary layer reported by Haigermoser *et al.* (2008). In the region near the cavity forward facing step (continuous blue line), the TKE shows a lower average power spectral density than the one contained in the rearmost region of the cavity (dashed red line). This confirms the amplification of modes of the incoming turbulent scales across the cavity opening by Kelvin-Helmotz type convective amplification mechanism. Whereas in a
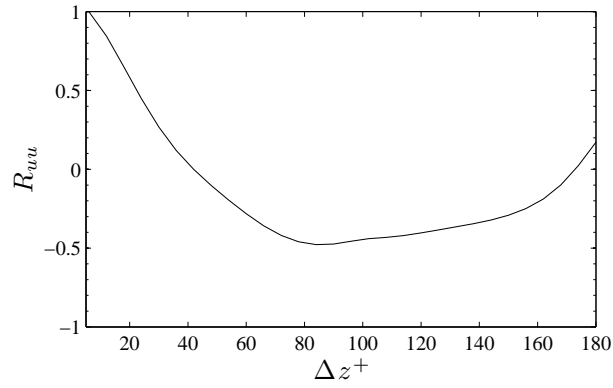
(a)
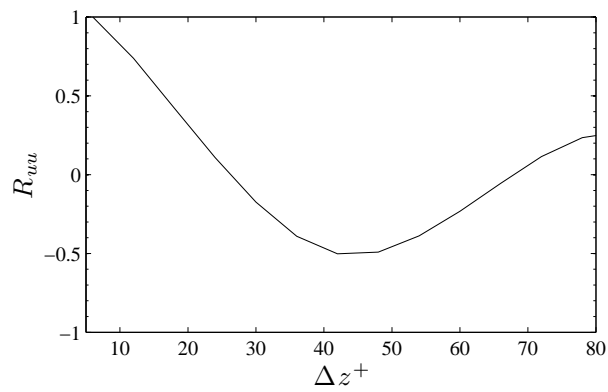
(b)
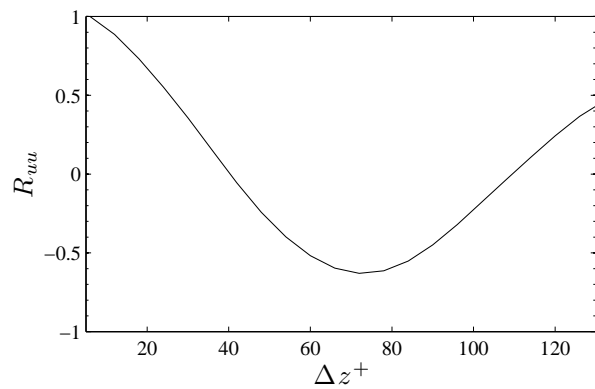
(c)

Figure 5.21: Time-averaged auto-correlation of streamwise velocity perturbations u' at $y^+ = 15$ and streamwise coordinates (a) $x/H = 0.4$, (b) $x/H = 2$, and (c) $x/H = 3.6$.
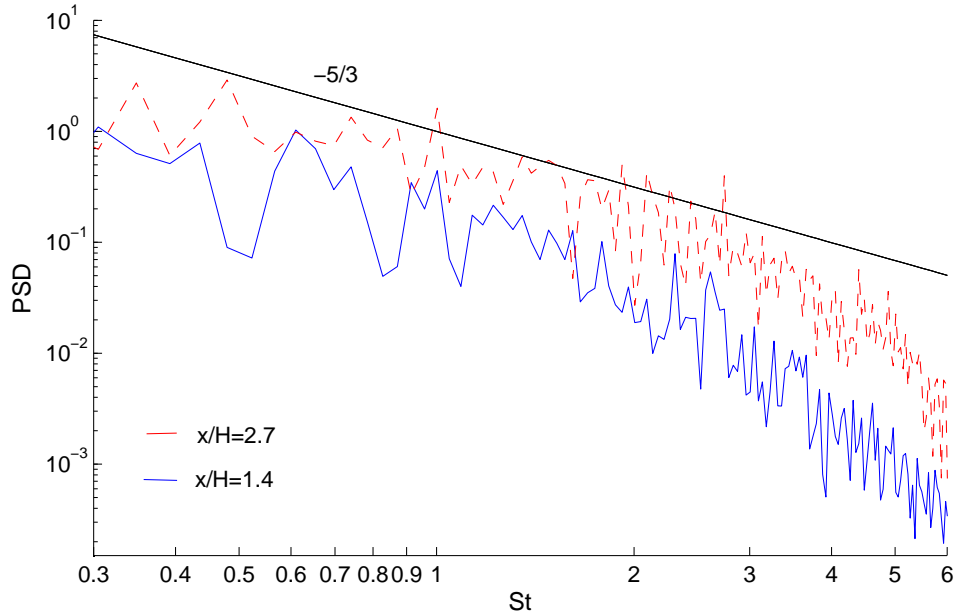
Figure 5.22: TKE Power Spectral Density at coordinates $x/H = 1.4$, $y^+ = 80$, $z/W = 0.5$ (continuous line), and $x/H = 2.7$, $y^+ = 80$, $z/W = 0.5$ (dashed line) from LES.

cavity-flow with a thin inflow boundary layer this amplification is selective, encouraging the the growth of selected modes (Alvarez *et al.*, 2004), in a cavity-flow driven by a thick boundary layer the amplification appears to be more broadband.

The classical energy cascade mechanism from decaying isotropic turbulence is more established at the back of the cavity, where the velocity spectrum better approximates the established $-5/3$ logarithmic decay rate of kinetic energy trough the inertial subrange, shown by the reference $-5/3$ slope in Figure 5.22 (black line). In this region, the decay is responsible for the dispersion of the kinetic energy from the structures the wavelength of which matches that of the Rossiter cavity resonance, to structures that do not take part in self-excitation.

Chapter 6

Conclusion

6.1 Designing and costing cavity flow CFD models

A time-dependent CFD model of the flow of over open cavity of a length to depth ratio $L/D = 4$, with a thick incoming boundary layer ($\delta/D \simeq 2.2$), at Mach 0.126, was used to study the noise and drag sources of automobile bodywork recesses.

The modelling process was explicited through a multi-variate dimensional analysis of the CFD parameters (Rona & Monti, 2011). This analysis enables to estimate *a priori* the computational cost and the spatial and temporal resolution in the cavity flow simulation. In this thesis, the CFD method selected to provide the best trade-off between computational cost and flow time and space resolution was a wall-resolved Large Eddy Simulation (WR-LES).

The CFD solver used is an explicit finite-volume, multi-block, structured, Runge-Kutta time integration scheme that uses a Recursive Domain Decomposition (RDD) parallelisation algorithm (Grottadaurea, 2009) to run on High Performance Computing platforms. The parallelisation algorithm was optimized in this work for the LES rectangular cavity flow test case. Scalability tests to assess the optimum number of processors for the simulations were performed and the results compared against the theoretical cost of the simulation obtained by the multivariate dimensional analysis model.

The cavity flow model was set up to match in Reynolds dynamic similarity the PIV experiments of Haigermoser *et al.* (2008).

The computational cost predicted by the *a priori* cost estimator is an effective tool for sizing up a cavity CFD computation in view of the computational resources available

and the spatial and temporal resolution requirements for the modeller. In literature, Basu *et al.* (2006) studied the dependence of the simulation cost on the turbulence closure approach and on the spatial and temporal discretisation for a unique cavity flow model, but this dependence has never been quantified parametrically for a broader class of unsteady cavity flows with different geometrical characteristics and flow parameters.

6.2   Cavity thick inflow boundary layer by LES

The time-resolved boundary layer for the cavity CFD simulation was generated by means of a Time-Dependent Synthetic-Stochastic (TDSS) inlet boundary condition, to mimic the time-dependent amplitude and phase information of the turbulent structures in the spatially developing thick boundary layer approaching the cavity. The method is based on the work by Sandham *et al.* (2003), subsequently extended to supersonic flow by Li & Coleman (2010). In this application, velocity fluctuations in space and time about the mean velocity profile are emulated by five synthetic velocity Fourier modes. Stochastic velocity random fluctuations were superimposed on the synthetic modes in order to break the symmetries deriving from the deterministic specification of the Fourier modes. The importance of a correct definition of the mean velocity profile at the computational domain inflow required the use of a numerical method by Rona & Monti (2012) that uses a new mixing length blending function.

In the precursor spatially developing boundary layer simulation, three flux limiters were used to compare the dissipative behaviour and select the best limiter to resolve the large-scale cavity flow motion. These are the SuperBee and MinMod limiters by Roe (1986), and the Sweby (1984) limiter. LES computation results shown that the Superbee limiter is not dissipative enough in the smooth region of flow, causing amplifying numerical oscillations and time-averaged values of streamwise velocity higher than that from the law of the wall. The Minmod limiter caused a re-laminarisation of the inner layer velocity profile that prevented the boundary layer from growing a logarithmic overlap region at the correct non-dimensional distance of around $30y^+$ from the wall. The best results were obtained with the Sweby limiter with the Sweby coefficient $\beta = 1.3$. A transition region was required for the flow to develop streaks and other distinguishing large-scale structures of a turbulent boundary layer, in agreement

with the boundary layer LES model by Keating *et al.* (2004). Non-dimensional velocity profiles were compared against the PIV measurements by Haigermoser (2009) and the Musker (1979) law of the wall for the inner layer. An appreciable agreement was found among the numerical, experimental, and analytical velocity profiles across the boundary layer. Instantaneous predictions of the streamwise velocity on a horizontal plane at distance $y^+ = 15$ to the wall displayed fully developed streaky structures with evidence of fine-scale turbulence generation and elongated structures in the streamwise direction. These structures were confirmed by the *Q*-criterion vortex visualisation. The characteristic spanwise length-scale in the boundary layer was determined by velocity auto-correlation analysis. The two-points spanwise auto-correlation function of the streamwise velocity fluctuations R_{uu} and of the wall-normal velocity fluctuations R_{vv}, determined the characteristic spanwise length scale $L_v(15y^+) = L_u(15y^+) \approx 160y^+$, in agreement with the typical streak spacing results reported in literature.

The use of time-dependent Synthetic-Stochastic inflow technique is a novel aspect in the context of cavity flow simulations. The method has shown to yield a fast transition to a fully developed turbulent flow, to resolve correctly the three-dimensional energy-carrying eddies in the thick boundary layer inflow, and to match the statistical information of these structures at the cavity inflow. These aims were pursued as a stringent requirement to correctly predict the turbulent scales and large eddies evolution across the cavity opening, and to model the shear instabilities from the cavity leading-edge onwards.

6.3   Three-dimensional rectangular cavity model

The influence of the flow structures produced by the LES inflow generation techniques on the instabilities in the cavity enclosure was studied in the LES cavity flow model and compared against the PIV experiments of Haigermoser *et al.* (2008,2009).

The optimization of the original Recursive Domain Decomposition (RDD) MPI parallelization algorithm by Grottadaurea & Rona (2008), was essential for running the wall-resolved LES testcase of 3.6 million cells.

The mean flow field from the LES indicates the presence of a large standing vortex that dominates almost 75% of the cavity length, and a secondary re-circulation, that appears in the LES results in the form of a weaker spiral re-circulation. The shape of

the vorticity thickness profile δ_v is in good agreement with the one form PIV measurements, however, the LES computation predicted a higher vorticity thickness growth rate near the forward facing step, where optical access in the PIV experiments was limited. This newly identified leading edge effect is likely due to a newly described unsteady flow mechanism of the streaks in the region of the cavity near the upstream edge.

The non-dimensional streamwise velocity shows a greater self-similarity in the outer layer, whereas in the inner layer, self-similarity is only approximately reached in the downstream cavity region, due to the presence of the bound vortex. The main vortex convection across the cavity opening was interpreted through the evaluation of two-point spatial correlation function of the velocity fluctuations $\rho_{u'u'}$, $\rho_{v'v'}$, and the mean pressure coefficient C_p. There was an appreciable agreement between the LES predictions and PIV experiments for the two-point spanwise auto-correlations and the predicted pressure cavity drag coefficient $\overline{C_D} = 0.056$ matched the one from the numerical integration of RANS equation by Haigermoser (2009) to two significant figures.

The study of the unsteady flow field was supported by the high level of detail in space and time obtained from the fine wall-resolved LES computation. Different visualizations of the instantaneous flow field, in terms of the spanwise vorticity ω_z and of the wall-normal vorticity ω_y enabled an explanation of the concurrence of vortical structures generated by the shear layer Kelvin-Helmotz type instability and of three-dimensional streak-related structures, as already identified in the PIV tomographic experiments of Haigermoser *et al.* (2008). It is thought that the structures are subject to the combined effect of the Kelvin-Helmotz type instability, vortex pairing interaction, hairpin vortex lift-up momentum of the approaching streaks, and induced velocity field of the standing vortex. The combined effects tilt, stretch and separate the vortices initially belonging to a coherent streak pattern, into smaller and less coherent structures. These structures are convected toward different paths and entrained into the cavity or ejected out of the cavity in a higher free-stream velocity field, depending on stochastic variations in their starting initial condition as they form over the cavity leading edge. The induced velocity of a streak pair approaching the cavity upstream edge was modelled with inviscid potential-flow theory. This simple model was found to qualitatively predict the visible tilt of the hairpin vortex heads in the upstream region of the cavity enclosure, which acts as the trigger for the Kelvin-Helmotz type convected instability.

The process of mass injection and ejection into and out of the cavity was further appreciated in flow visualizations obtained by the Q-criterion, where intermittent mass flow is generated as result of the opposite actions of vorticity and strain regions containing the turbulent scales.

The velocity auto-correlation analysis allowed to investigate the evolution of the turbulent structures across the cavity opening and to relate the value of the longitudinal velocity correlation function to the space-time properties of turbulence and to corresponding noise sources (Lilley, 1996). In the cavity upstream region the streak spacing becomes irregular. This leads to a reduction in the longitudinal velocity two-point correlation which, according to Lilley (1996), is expected reduce the emission of the sound generated aerodynamically. A greater spanwise coherence in the rearmost portion of the cavity is counteracted by the presence of strong negatively correlated velocity fluctuations. This is expected to generate a dipole-type directivity in the transverse direction.

The absence in the power spectral density analysis of clearly identifiable spectral peaks above the broadband level suggested that no tonal instability is present in the flow. A lower average power spectral density was registered in the region near the cavity forward facing step, than the one contained in the rear region of the cavity. This confirms the convection amplification across the cavity of the modes related to the turbulent scales contained in the approaching thick boundary layer. The broadband noise by Kelvin-Helmotz type convective amplification mechanism in thick boundary layer cavity flow differs from the Rossiter mode tonal noise, which results from the selective amplification in a cavity flow of one or two main frequencies in the kinetic energy spectrum of a thin incoming boundary layer.

The detailed understanding of the flow dynamics of the instability amplification mechanism and its relationship with the noise sources in a cavity flow with a thick boundary layer represents a contribution to the advancement of the state-of-the-art in this field. The level of detail in space and time of the predictions obtained by the LES computation enhanced the understanding of the cavity flow physics to the case of relatively low values of L/θ at low Mach numbers. The PIV experiments of Haigermoser *et al.* (2008,2009) have shown the concurrence of vortical and randomly distributed structures in the shear layer, but were limited by the low acquisition rate, the wall light reflection and the lower spatial resolution of the uniform PIV vector grid, as compared

to the non-uniform numerical mesh. In the present work it was possible to understand the process of creation and evolution of these structures across the cavity opening, from the initial condition of coherent streak patterns approaching the cavity leading edge. Amplification of the incoming turbulent scales energy modes across the cavity opening by Kelvin-Helmotz type convective amplification mechanism was shown for cavity flows with a thick inflow, as opposed to the selective amplification mechanism of cavities with a thin boundary layer inflow. Evidence of this mechanism was provided by investigating the flow dynamics of the resolved scales in space and time by LES. The results also explaines the intermittent behaviour of mass injection and ejection inside and outside the cavity and the related pressure fluctuation along the cavity walls, which are mainly responsible for noise emission.

6.4   Future Work

Further research is required to advance the state-of-the art knowledge on the generation and propagation of noise generated aerodynamically in cavities with thick boundary layers. This enhanced understanding, enabled by the CFD approach, could be of significant help towards reducing automotive noise emission level and enhance the driver's comfort. Toward this direction, the far-field propagation of the near-field noise sources identified in the present work can be studied by acoustic analogy.

Rona & Spisso (2007) and Ghillani (2012) have been developing a high-order finite-difference scheme as an upgrade of the flow solver used in this work. The high-order method allows to reduce dispersion and dissipation errors on structured meshes compared to the second-order accuracy of the scheme used in this work. The high-order method could be used to model, at the equivalent computational cost of the LES of the present study, a computational domain including the cavity near field and up to a few acoustic wavelengths of the lowest relevant spectral band.

The cavity flow model developed in this thesis can be extended to a range of cavity geometries and flow regimes. The results obtained could be used to perform a sensitivity analysis of the quantitative results in this thesis on the geometry and flow conditions.

Another important challenge is to control the physical mechanism of momentum transfer into and out of the cavity identified in this thesis, by applying passive control devices. An experimental PIV study on passive cavity flow control was conducted

by Vesely (2009). Different flow devices like fences, ramps, spoiler, and rods were selected to suppress the momentum transfer into and out of the cavity and the associated noise radiation. A numerical investigation could confirm the experimental results as well as giving an insight into the physics of effective noise suppression devices. The space and time resolution of the LES or DNS computations could improve the understanding of the flow mechanisms that influence the flow oscillations, their amplification, the noise sources, and cavity drag reduction, in order to improve the geometry of passive flow control devices for real-life engineering applications.

Alternative HPC techniques such as MPI - Open MP hybrid algorithms, that lends to less tuning and customization than the RDD MPI algorithm, could be further investigated in a computational research framework for future works.

Appendix A

Asymptotic matching of the inner and outer velocity profiles

To describe the mean velocity profile in a turbulent boundary layer, similarity solutions are sought in the inner and the outer regions. In the inner region, the mean streamwise velocity u scales with the wall friction velocity u_τ and with the viscous length scale $l = \nu_l/u_\tau$, so that

$$\frac{u}{u_\tau} = f(y^+) \tag{A.1}$$

where $y^+ = yu_\tau/\nu_l$ is the inner scaling non-dimensional wall-normal distance. In outer region, the velocity profile is described by the velocity defect law

$$\frac{u_\infty - u}{u_\tau} = f(\eta) \tag{A.2}$$

where $\eta = y/\delta$ is the outer scaling non-dimensional wall-normal distance, u_∞ is the free-stream velocity, ν_l is the laminar kinematic viscosity, y is the wall-normal distance and δ is the boundary layer thickness, which is taken as the wall-normal distance at which $u = u_\infty$.

Based on the existence of an overlap region between the inner and the outer regions, Coles (1956) proposed the following additive law of the wall and law of the wake in non-dimensional form:

$$u^+ = \frac{1}{\kappa}\ln y^+ + B + \frac{\Pi}{\kappa}f(\eta)$$
$$f(\eta) = 1 - \cos(\pi\eta) \tag{A.3}$$

A. ASYMPTOTIC MATCHING OF THE INNER AND OUTER VELOCITY PROFILES

where $u^+ = u/u_\tau$ is the normalized streamwise velocity, Π is the wake parameter, κ the von Kármán constant, and B the logarithmic law constant.

The wake parameter was determined (Coles, 1956) as

$$\Pi = \kappa/2 \left(u^+_\infty - \kappa^{-1} \ln Re_\tau - B \right) \tag{A.4}$$

where $Re_\tau = \delta u_\tau / \nu_l$ is the boundary layer Reynolds number and $u^+_\infty = u_\infty / u_\tau$ is the normalized free-stream velocity.

Let

$$f(\eta) = A_1 \eta^2 + A_2 \eta^3 \tag{A.5}$$

be a cubic polynomial approximation to $f(\eta)$ in Equation (A.3). Substituting the boundary conditions

$$u|_{y=\delta} = u_\infty \tag{A.6}$$

and

$$\left. \frac{\partial u}{\partial y} \right|_{y=\delta} = 0 \tag{A.7}$$

in Equation (A.3), with $f(\eta)$ from Equation (A.5), gives $A_1 = 6 [1 + 1/(6\Pi)]$ and $A_2 = -4 [1 + 1/(4\Pi)]$, with Π defined by Equation A.4. The law of the wake of Equation (A.3) then becomes

$$u^+ = \underbrace{\overbrace{\frac{1}{\kappa} \ln y^+ + B}^{\text{Log-law of the wall}} + \frac{1}{k} \eta^2 (1 - \eta)}_{\text{Pure wall flow}} \underbrace{+2 \frac{\Pi}{\kappa} \eta^2 (3 - 2\eta)}_{\text{Pure wake component}} \tag{A.8}$$

To evaluate Equation (A.8), the following parameters are taken: $\kappa = 0.41$ and $B = 5.0$. Equation (A.8) is validated over a relatively wide range of momentum thickness based Reynolds number $Re_\theta = u_\infty \theta / \nu_l$ in the work of Rona & Monti (2012).

Appendix B

Relationship between spectral width and grid density

Further considerations are required to express the relationship between the maximum wavenumber, $k_{j,\mathrm{max}}$, and the minimum grid spacing $\Delta x_{j,\mathrm{min}}$.

Given a generic n^{th} order numerical scheme, the modified wavenumber $K(k\Delta x)$ approximates in the discrete computational domain the non-dimensional wavenumber $k\Delta x$ in the continuous space. The accuracy of a numerical method at various scales is illustrated by its ability to approximate the derivative of a single Fourier mode e^{ikx} (Moin & Mahesh, 1998).

Modified wavenumber curves are plotted in Figure B.1.(a) for numerical schemes of different order n, where the continuous straight line corresponds to the wavenumber relation for an exact differentiation. The minimum number of points per wavelength, *PPW*, that are required to resolve a given wavenumber is associated to the maximum acceptable relative error $|\varepsilon(k\Delta x)|$ from the spatial discretization (Colonius & Lele, 2004). Figure B.1.(b) shows $|\varepsilon(k\Delta x)|$ for numerical schemes of different order n.

$$\varepsilon(k\Delta x) = \frac{K(k\Delta x) - k\Delta x}{k\Delta x} \tag{B.1}$$

Let 5% be a representative maximum relative error accepted in a typical engineering application. From Figure B.1.(b), the intercept of the $|\varepsilon(k\Delta x)| = 5E - 2$ line with the error distribution for each scheme determines the *PPW*. Table B.1 shows the results for the more commonly used finite difference schemes.

B. RELATIONSHIP BETWEEN SPECTRAL WIDTH AND GRID DENSITY

Table B.1: Point per wavelength (PPW) required for a maximum absolute relative error $|\varepsilon(k\Delta x)| = 5\%$ for various finite difference schemes.

Scheme	$PPW\big|_{|\varepsilon(k\Delta x)|=5\%}$
2nd order Explicit	10.3
4th order Explicit	5.8
6th order Explicit	4.1
4th order Compact	4
6th order Compact	2.9

On uniform meshes, the scheme PPW links the minimum wavenumber resolved with the uniform mesh size by

$$k_{j,\max} = \frac{2\pi}{PPW\left(\Delta x_{j,\min}\right)} \tag{B.2}$$

Most simulations, however, use mesh stretching functions and these needs to be accounted for to determine $k_{j,\max}$.

Given a uniform grid in a generic direction j, the uniform spacing variable is:

$$\xi_i = (i-1)/(I-1), i = 1, ..., I \tag{B.3}$$

where i is the spatial index of the mesh point and I is the total number of points in the stretching direction. The clustered point coordinates are obtained by applying a stretching function $s_i = s(\xi_i)$ such that $0 \leqslant s(\xi) \leqslant 1$, to generate the point coordinate in the arc length parameter $x(\xi_i)$. Examples of common clustering functions used in past cavity CFD works are the exponential stretching (Equation (B.4)), the hyperbolic tangent (Equation (B.5)) and the Gaussian (Equation (B.6)) stretching functions:

$$x(\xi) = \frac{e^{c\xi} - 1}{e^c - 1} \tag{B.4}$$

$$x(\xi) = 1 + \frac{\tanh c (\xi - 1)/2}{\tanh c/2} \tag{B.5}$$

$$x(\xi) = \frac{1 + erf(\xi)}{2} \tag{B.6}$$

where c is the stretching factor coefficient.

B. RELATIONSHIP BETWEEN SPECTRAL WIDTH AND GRID DENSITY

From Equations (B.4) and (B.6), the minimum grid spacing results $\Delta x_{j,\min} = x(\xi_i)|_{i=1}$ and the minimum wavelength $\lambda_{j,\min} = x(\xi_i)|_{i=PPW}$. It follows that, on a stretched conformal structured mesh the maximum wavenumber resolved numerically in the j-direction is

$$k_{j,\max} = \frac{2\pi}{\lambda_{j,\min}} = \frac{2\pi}{x(\xi_i)|_{i=PPW}} \tag{B.7}$$

In the case of a uniform grid Equation (B.7) reduces to:

$$k_{j,\max} = \frac{2\pi}{\lambda_{j,\min}} = \frac{2\pi}{PPW\left(\Delta x_{j,\min}\right)} = \frac{2\pi}{PPW x(\xi_i)|_{i=1}} \tag{B.8}$$

The number of mesh points required to simulate a structure of lenght $\lambda_{j,\max}$ in the j-direction depends on the grid spacing Δx_j. The highest $N_{c,j}$ requirement $\widehat{N_{c,j}}$ is obtained when the grid spacing is uniform and is:

$$\widehat{N_{c,j}} = \frac{\lambda_{j,\max}}{\Delta x_{j,\min}} \tag{B.9}$$

If a clustering function is adopted, such as in the large velocity gradient region near the solid walls, the number of mesh points required becomes much smaller and can be expressed through a functional $\Im_j(s_1(\xi), s_2(\xi), ..., s_n(\xi))$ that consider the different stretching functions adopted along the domain in the direction j:

$$N_{c,j} = \frac{\lambda_{j,\max}}{\Delta x_{j,\min}\Im_j} \tag{B.10}$$

However, if an average mesh spacing $\overline{\Delta x_j}$ for the first PPW points is considered, it is possible to obtain uniform mesh equivalent $N_{c,j}$ for the stretched mesh case. From Eq. B.8,

$$\overline{\Delta x_j} \cdot PPW = \lambda_{j,\min} \tag{B.11}$$

which gives a general relationship between $N_{d,j}$ and $N_{c,j}$:

$$N_{d,j} = \frac{DS_j}{PPW\overline{\Delta x_j}} = \frac{N_{c,j}}{PPW} \tag{B.12}$$
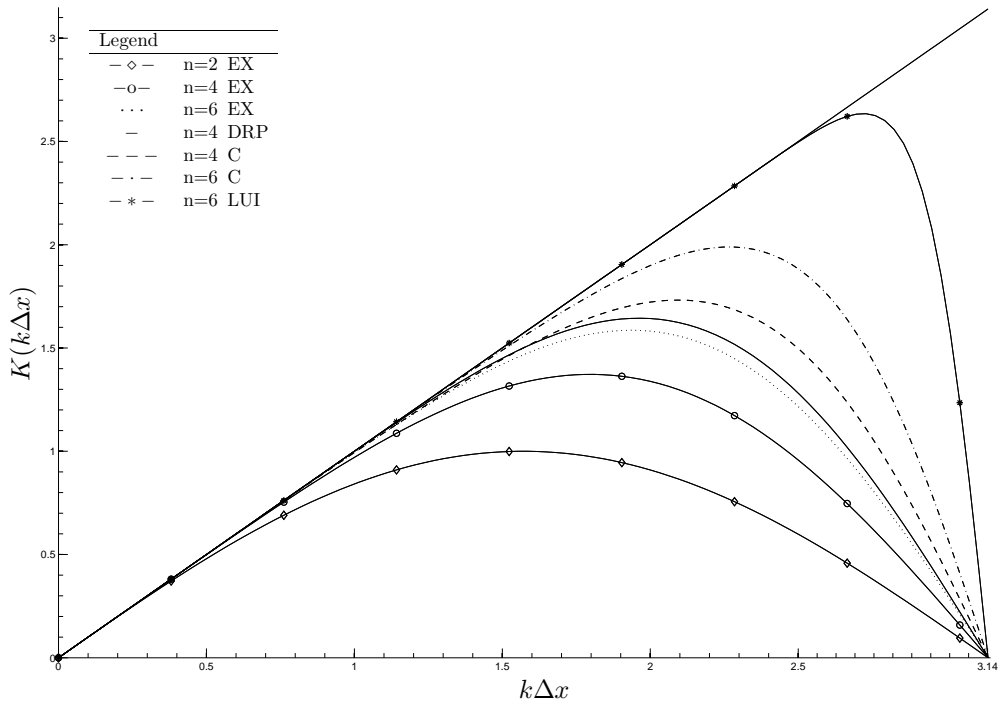
(a)
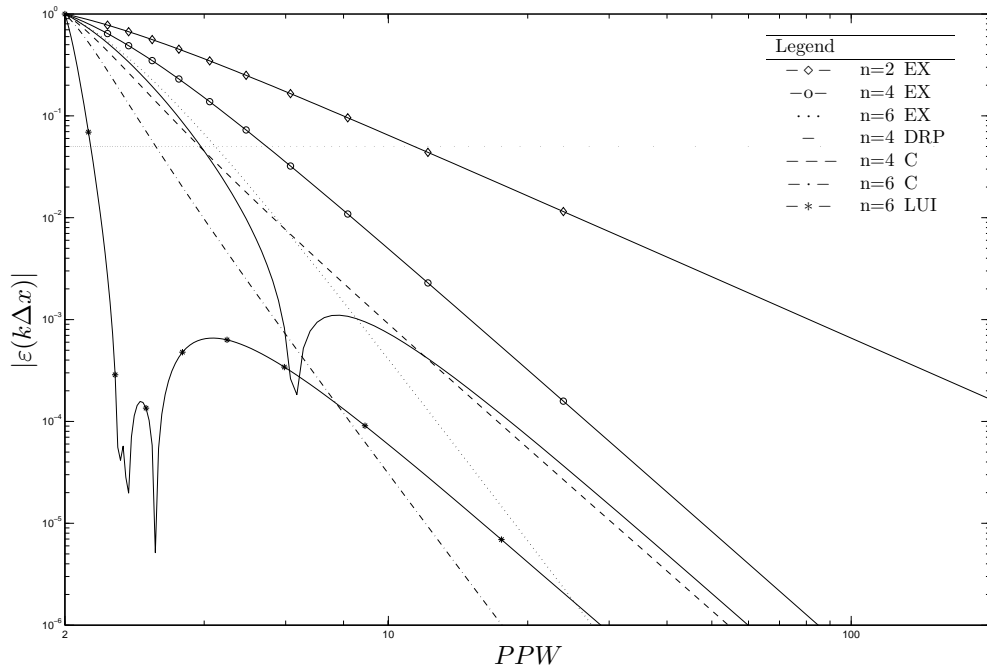
(b)

Figure B.1: (a) Modified wavenumber curves (continuous straight line: exact differentiation). (b) Minimum number of points per wavelength, PPW associated to the maximum acceptable relative error $|\varepsilon(k\Delta x)|$ from the spatial discretization. Legend, n: scheme order, EX: Explicit, C: Compact, DRP: Dispersion-Relation-Preserving Finite Difference Tam & Web (1993), LUI: Pentadiagonal compact Lui & Lele (2001)

References

ALVAREZ, J.O., KERSHEN, E.J. & TUMIN, A. (2004). A theoretical model for cavity acoustic resonances in subsonic flow. *AIAA paper*, **2485**.
Referenced on page: 92

ARUNAJATESAN, S. & SINHA, N. (2001). Unified Unsteady RANS-LES Simulations of cavity flowfields. Conference paper 2001-0516, AIAA, Reno, NV, United States, 39th AIAA Aerospace Sciences Meeting and Exhibit.
Referenced on page: 8

ARUNAJATESAN, S. & SINHA, N. (2003). Hybrid rans-les modeling for cavity aeroacoustics predictions. *International Journal of Aeroacoustics*, **2**, 65–93.
Referenced on page: 8

ARUNAJATESAN, S., SHIPMAN, J. & SINHA, N. (2002). Hybrid RANS-LES simulation of cavity flow fields with control. Conference paper 2002-1130, AIAA, Reno, NV, United States, 40th AIAA Aerospace Sciences Meeting and Exhibit.
Referenced on page: 8, 44

ASHCROFT, G. & ZHANG, X. (2005). Vortical structures over rectangular cavities at low speed. *Physics of Fluids*, **17**.
Referenced on page: 72, 76

BASU, D., HAMED, A. & DAS, K. (2004). Assessment of hybrid turbulence models for unsteady high speed separated flow predictions. Conference paper 2004-0684, AIAA, Reno, NV, United States, 42nd AIAA Aerospace Sciences Meeting and Exhibit.
Referenced on page: 8

BASU, D., HAMED, A. & DAS, K. (2005). DES and Hybrid RANS/LES models for unsteady separated turbulent flow predictions. Conference paper 2005-0503, AIAA, Reno, NV, United States, 43rd AIAA Aerospace Sciences Meeting and Exhibit.
Referenced on page: 8, 44

BASU, D., HAMED, A., DAS, K., LIU, Q. & TOMKO, K. (2006). Comparative analysis of hybrid turbulence closure models in the unsteady transonic separated flow simulations. Conference paper 2006-0117, AIAA, Reno, NV, United States, 44th AIAA Aerospace Sciences Meeting and Exhibit.
Referenced on page: 8, 29, 44, 94

BATTEN, P., GOLDBERG, U. & CHAKRAVARTHY, S. (2004). Interfacing statistical turbulence closures with large-eddy simulation. *AIAA Journal*, **42**, 485–492.
Referenced on page: 12

BERNARDINI, M. (2008). private communication. Tech. rep., Università La Sapienza.
Referenced on page: 27

BISSESSUR, P., CHEN, X.X. & ZHANG, X. (2004). Numerical investigation of subsonic 2D/3D cavity flows. Conference paper 2004-683, AIAA, Reno, NV, United States, 42nd AIAA Aerospace Sciences Meeting and Exhibit.
Referenced on page: 71

BRES, G. & COLONIUS, T. (2007). Three-dimensional linear stability analysis of cavity flows. Conference paper 2007-1126, AIAA, Reno, NV, United States, 45th AIAA Aerospace Sciences Meeting and Exhibit.
Referenced on page: 8, 44

CHANG, K. & PARK, S. (2004). Hybrid RANS/LES simulation of deep cavity flow. Conference paper 2004-53, AIAA, Reno, NV, United States, 42nd AIAA Aerospace Sciences Meeting and Exhibit.
Referenced on page: 8, 44

CHANG, K., CONSTANTINESCU, G. & PARK, S. (2006). Analysis of the flow and mass transfer processes for the incompressible flow past an open cavity with a laminar and a fully turbulent incoming boundary layer. *Journal of Fluid Mechanics*, **561**,

113–145.

Referenced on page: 8, 44

CHAPMAN, D. (1978). Computational aerodynamics development and outlook. *AIAA Journal*, **17**, 1293–1313.

Referenced on page: 33, 33, 38

CHARWAT, A., ROOS, J., DEWEY, F. & HITZ, J. (1961). An investigation of separated flows. Part I: The pressure field. *Journal Aerospace Science*, **28**, 457–470.

Referenced on page: 6

CHEN-CHUAN FAN, T. (2002). *Hybrid Reynolds-Averaged / Large-Eddy Simulations of ramped-cavity and compression ramp flow-fields*. Degree of master of science, Raleigh, North Carolina.

Referenced on page: 18

CHERNYSHENKO, S. & BAIG, M. (2005). Streaks and vortices in near-wall turbulence. *Philosophical Transaction of the Royal Society*, **363**, 1097–1107.

Referenced on page: 57

COLES, D. (1956). The law of the wake in the turbulent boundary layer. *J. Fluid Mech.*, **1**, 191–226.

Referenced on page: 26, 100, 101

COLONIUS, T. (2001). An overview of simulation, modeling, and active control of flow/acoustic resonance in open cavities. *Progress on Aerospace Sciences*, **40**, 365–416.

Referenced on page: 8

COLONIUS, T. & LELE, S. (2004). Computational aeroacoustics: progress on nonlinear problems of sound generation. *Progress in Aerospace Sciences*, **40**, 365–416.

Referenced on page: 8, 102

COURANT, R., FRIEDRICHS, K. & LEWY, H. (1928). Über die partiellen differenzengleichungen der mathematischen physik. *Mathematische Annalen*, **100**, 32–74.

Referenced on page: 24

COUSTEIX, J. & MAUSS, J. (2007). *Asymptotic analysis and boundary layers*. Springer-Verlag, Berlin Heidelberg.

Referenced on page: 26

DAHLSTRÖM, S. & DAVIDSON, L. (2003). Hybrid RANS/LES employing interface condition with turbulent structure. In I. Begell House, ed., *Turbulence, Heat and Mass Transfer*, vol. 4, 689–696, K. Hanjalić, Y. Nagano and M. Tummers.

Referenced on page: 17

DEARDORFF, J.W. (1970). A numerical study of three-dimensional turbulent channel flow at large Reynolds numbers. *Journal of Fluid Mechanics*, **41**, 453–480.

Referenced on page: 10

DE GRAAFF, D. & EATON, J. (2000). Reynolds-number scaling of the flat-plate turbulent boundary layer. *Journal of Fluid Mechanics*, **422**, 319–346.

Referenced on page: 52

EL-DOSOKY, M.F.F. (2009). *Analytical and CFD methods investigating shrouded blade tip leakage*. Phd thesis, faculty of science, University of Leicester.

Referenced on page: 22

FINLEY, P., POE, K. & POH, C. (1966). Velocity measurements in a thin turbulent water layer. *La Houille Blanche*, **21**, 713–721.

Referenced on page: 52

FRIGO, M. & JOHNSON, S.G. (2005). The design and implementation of fftw3. *Proceedings of the IEEE*, **93**, 216–231.

Referenced on page: 90

GERMANO, M., PIOMELLI, U., MOIN, P. & CABOT, W.H. (1991). A dynamic subgrid-scale eddy viscosity model. *Physics of Fluids A*, **3**, 1760–1765.

Referenced on page: 10

GHARIB, M. & ROSHKO, A. (1987). The effect of flow oscillations on cavity drag. *Journal of Fluid Mechanics*, **177**, 501–530.

Referenced on page: 8

GHILLANI, P. (2012). *Aeroacoustic simulation of a linear cascade by a prefactored compact scheme*. Ph.D. thesis, University of Leicester.
Referenced on page: 98

GHOSAL, S. & MOIN, P. (1995). The Basic Equations for the Large Eddy Simulation of Turbulent Flows in Complex Geometry. *Journal of Computational Physics*, **118**.
Referenced on page: 9

GLOERFELT, X., BOGEY, C. & BAILLY, C. (2002a). LES of the noise radiated by a flow over a rectangular cavity. DGLR Report 2002-03, DLR, Göttingen, Germany, proceedings of the International Workshop on LES for Acoustics.
Referenced on page: 8

GLOERFELT, X., BOGEY, C., BAILLY, C. & JUVÉ, D. (2002b). Aerodynamic noise induced by laminar and turbulent boundary layers over rectangular cavities. Conference paper 2002-2476, AIAA, Breckenridge, Colorado, United States, 8th AIAA/CAES Conference.
Referenced on page: 8, 44

GOTTERO, M. & ONORATO, M. (2000). Low-speed streak and internal shear layer motions in a turbulent boundary layer. *Eur. J. Mech. B - Fluids*, **19**, 23–36.
Referenced on page: 85

GRACE, S. (2001). An overview of computational aeroacoustics techniques applied to cavity noise prediction. Conference paper 2001-0510, AIAA, Reno, NV, 39th AIAA Aerospace Sciences Meeting & Exhibit.
Referenced on page: 7

GRACE, S., DEWAR, W. & WROBLEWSKI, D. (2004). Experimental investigation of the flow characteristics within a shallow wall cavity for both laminar and turbulent upstream boundary layers. *Experiments in Fluids*, **36**, 791–804.
Referenced on page: 70

GROTTADAUREA, M. (2009). *Aerodynamics and near-field acoustics of a subsonic cylindrical cavity flow by parallel CFD*. Ph.D. thesis, University of Leicester.
Referenced on page: 25, 28, 93

GROTTADAUREA, M. & RONA, A. (2007). Noise sources from a cylindrical cavity. Conference paper, AIAA/CEAS Aeroacoustics Conference13th, Rome, Italy.

Referenced on page: 42

GROTTADAUREA, M. & RONA, A. (2008). The radiating pressure field of a turbulent cylindrical cavity flow. Conference paper 2008-2852, AIAA, Vancouver, Canada, 14th AIAA/CEAS Aeroacoustics Conference.

Referenced on page: 42, 95

HAIGERMOSER, C. (2009). *Investigation of cavity flows using advanced optical methods*. Ph.D. thesis, Politecnico di Torino.

Referenced on page: 1, 4, 5, 52, 53, 60, 60, 61, 69, 71, 72, 72, 74, 76, 78, 78, 79, 85, 86, 87, 95, 95, 96, 97

HAIGERMOSER, C., VESELY, L., NOVARA, M. & ONORATO, M. (2008). A time-resolved particle image velocimetry investigation of a cavity flow with a thick incoming turbulent boundary layer. *Physics of Fluids*, **20**.

Referenced on page: 3, 4, 4, 4, 5, 8, 69, 70, 80, 82, 83, 90, 93, 95, 96, 97

HAMED, A., BASU, D. & DAS, K. (2001). Direct Numerical Simulations of high speed flow over cavity. Conference paper, Air Force Office of Scientific Research, Arlington, Texas, United States, 3rd AFOSR International Conference on DNS/LES (TAICDL).

Referenced on page: 8, 44

HAMED, A., BASU, D. & DAS, K. (2003). Effect of Reynolds number on the unsteady flow and acoustic fields of a supersonic cavity. Conference paper 2003-45473, ASME, Honolulu, Hawaii, United States, 4th ASME JSME Joint Fluids Engineering Conference.

Referenced on page: 8, 44

HAMED, A., BASU, D. & DAS, K. (2004). Numerical simulations of fluidic control for transonic cavity flows. Conference paper 2004-0429, AIAA, Reno, NV, United States, 42nd AIAA Aerospace Sciences Meeting and Exhibit.

Referenced on page: 8

HIRSCH, C. (1988). *Numerical computation of internal and external, Vol. 2: computational methods for inviscid flows*, vol. 2. A Wiley-Interscience Publication.
Referenced on page: 20

HU, Z. & SANDHAM, N.D. (2001). Dns databases for turbulent couette and poiseuille flow. Tech. Rep. 01/04, AFM Research group, SES, University of Southampton, UK.
Referenced on page: 57

HUNT, J., WRAY, A. & MOIN, P. (1988). Eddies, stream, and convergence zones in turbulent flows. Tech. Rep. CTR-S88, Center for Turbulence Research.
Referenced on page: 55, 85

ICAO, I.C.A.O., ed. (2005). *Environmental Protection, Aircraft Noise Annex 16*, vol. I. 4th. ed.
Referenced on page: 1

JARRIN, N., BENHAMADOUCHE, S., LAURENCE, D. & PROSSER, R. (2006). A synthetic-eddy method for generating inflow conditions for Large-Eddy Simulations. *International Journal of Heat and Fluid Flow*, **27**, 585–593.
Referenced on page: 13

KEATING, A., PIOMELLI, U., BALARAS, E. & KALTENBACH, H.J. (2004). A priori and a posteriori tests of inflow conditions for large-eddy simulation. *Physics of Fluids*, 4696–4712.
Referenced on page: 11, 50, 95

KIM, W. & MENON, S. (1995). A new dynamic one-equation subgrid-scale model for large eddy simulation. Tech. rep., AIAA.
Referenced on page: 11

LARCHEVÊQUE, L., SAGAUT, P., LÊ, T. & COMTE, P. (2004a). Large Eddy Simulation of a compressible flow in a three-dimensional open cavity at high Reynolds number. *Journal of Fluid Mechanics*, **516**, 265–301.
Referenced on page: 8, 44

LARCHEVÊQUE, L., SAGAUT, P., MARY, I. & LABBE, O. (2004b). Large-Eddy Simulation of a compressible flow past a deep cavity. *Physics of Fluids*, **15**, 193–210.
Referenced on page: 8, 44

LARCHEVÊQUE, L., SAGAUT, P. & LABBE, O. (2007). Large-Eddy Simulation of a subsonic cavity flow including asymmetric three-dimensional effects. *Journal of Fluid Mechanics*, **577**, 105–126.
Referenced on page: 8

LE, H., MOIN, P. & KIM, J. (1997). Direct Numerical Simulation of turbulent flow over a backward-facing step. *Journal of Fluid Mechanics*, **330**, 349–374.
Referenced on page: 12

LI, N., BALARAS, E. & PIOMELLI, U. (2000). Inflow conditions for large eddy simulations of mixing layers. *Physics of Fluids*, **12**.
Referenced on page: 12

LI, Q. & COLEMAN, G.N. (2010). *DNS of an oblique shock wave impinging upon a turbulent boundary layer*, 81. 01, Kluwer Academic.
Referenced on page: 13, 25, 94

LIGHTHILL, M. (1952). On sound generated aerodynamically. i. general theory. *Proc. R. Soc. Lond*, **211**, 564–587.
Referenced on page: 89

LIGHTHILL, M. (1992). An estimate of the covariance of an estimate of the covariance of txx without using statistical assumptions, see. *Lilley, G. M. On the noise radiated from a turbulent high speed jet, Appendix 1, in Computational Aeroacoustics (Hardin, J.C., and Hussaini, M.Y., eds.), Springer-Verlag, New York.*.
Referenced on page: 89

LILLEY, G.M. (1996). The radiatiated noise from isotropic turbulence with applications to the theory of jet noise. *Journal of Sound and Vibration*, **190**, 463–476.
Referenced on page: 89, 90, 97

LILLY, D.K. (1992). A proposed modification of the Germano subgrid-scale closure method. *Physics of Fluids*, **4**, 633–635.

Referenced on page: 11

LIU, Y., TUCKER, P.G. & KERR, R.M. (2008). Linear and nonlinear model large-eddy simulations of a plane jet. *Computers & Fluids*, **37**, 439–449.

Referenced on page: 16

LUI, C. & LELE, S.K. (2001). Direct numerical simulation of spatially developing, compressible, turbolent mixing layers. *AIAA paper*.

Referenced on page: 105

LUND, T.S., WU, X. & SQUIRES, K.D. (1998). Generation of Turbulent Inflow Data for Spatially-Developing Boundary Layer Simulations. *Journal of Computational Physics*, **140**, 233–258.

Referenced on page: 11

MANNA, M. (1992). *A three dimensional high resolution compressible flow solver*. Phd thesis, faculty of applied science, Université Catholique de Louvain.

Referenced on page: 21, 22

MCMULLAN, W.A. & PAGE, G.J. (2011). Large eddy simulation of a controlled diffusion compressor cascade. *Flow Turbulence Combustion*, **86**, 207–230.

Referenced on page: 18

MOIN, P. & MAHESH, K. (1998). DIRECT NUMERICAL SIMULATION: A tool in turbulence research. *Annual Review of Fluid Mechanics*, **30**, 539–578.

Referenced on page: 102

MOON, Y., SEO, J., KOH, S. & CHO, Y. (2003). Aeroacoustic tonal noise prediction of open cavity flows involving feedback. *Journal of Computational Mechanics*, **31**, 359–366.

Referenced on page: 8, 44

MURRAY, N. & UKEILEY, L. (2004). Low-dimensional estimation of cavity flow dynamics. Conference paper 2004-681, AIAA, Reno, Nevada, 42nd AIAA Aerospace

Sciences Meeting and Exhibit.

Referenced on page: 7

MUSKER, A. (1979). Explicit expression for the smooth wall velocity distribution in a turbulent boundary layer. *AIAA Journal*, 655–657.

Referenced on page: 27, 52, 95

NICOUD, F. & DUCROS, F. (1999). Subgrid-scale modelling based on the square of the velocity gradient tensor. *Journal of Flow, Turbulence and Combustion,*, 183–200.

Referenced on page: 10

PIOMELLI, U. & BALARAS, E. (2002). Wall-layer models for Large Eddy Simulation. *Annual Review of Fluid Mechanics*, **34**, 349–374.

Referenced on page: 32, 42

PIROZZOLI, S., BERNARDINI, M. & GRASSO, F. (2008). Characterization of coherent vortical structures in a supersonic turbulent boundary layer. *Journal of Fluid Mechanics*, 205–231.

Referenced on page: 3, 4, 13

RIBALDONE, E., CASTELLUCCIO, V. & MARCHESE, P. (2005). Experimental and numerical study of tonal noise in flow-excited cavities. Tech. rep., CRF-FIAT Research Centre, Vehicles NVH.

Referenced on page: 1, 60

RIZZETTA, D. & VISBAL, M. (2003). Large-Eddy Simulation of supersonic cavity flowfields including flow control. *AIAA Journal*, **41**, 1452–1462.

Referenced on page: 8, 44

ROCKWELL, D. & NAUDASCHER, E. (1978). Review - self-sustaining oscillations of flow past cavities. *ASME, Transactions, Journal of Fluids Engineering*, **100**, 152–165.

Referenced on page: 6

ROE, P.L. (1981). Approximate riemann solvers, parameter vectors and difference schemes. *J. Comput. Phys.*, **43**, 357–372.

Referenced on page: 20

Roe, P.L. (1986). Characteristic-based schemes for the Euler equations. *Annual Review of Fluid Mechanics*, **18**, 337–365.
Referenced on page: 21, 51, 94

Rona, A. & Monti, M. (2011). Regressing the size and cost of turbulent cavity flow simulations. *Journal of Algorithms & Computational Technology*, **5**, 383–412.
Referenced on page: 2, 4, 30, 34, 38, 93

Rona, A. & Monti, M. (2012). On the generation of the mean velocity profile for turbulent boundary layers with pressure gradient under equilibrium conditions. *The Aeronautical Journal*, **116**.
Referenced on page: 25, 26, 94, 101

Rona, A. & Spisso, I. (2007). Implementation of a high-order finite difference scheme to model wave propagation. Conference paper 2007-3487, AIAA/CEAS Aeroacoustics Conference13th, Rome.
Referenced on page: 98

Rossiter, J. (1964). Wind-tunnel experiments on the flow over rectangular cavities at subsonic and transonic speeds. Technical Report 3438, Aeronautical Research Council Reports and Memoranda.
Referenced on page: 7

Rowley, C., Colonius, T. & Basu, A. (2002). On self-sustained oscillations in two-dimensional compressible flow over rectangular cavities. *Journal of Fluid Mechanics*, **455**, 315–46.
Referenced on page: 8, 44

Sagaut, P. (2002). *Large Eddy Simulation for incompressible flows*. Springer.
Referenced on page: 11, 30

Sandham, N., Yao, Y. & Lawal, A. (2003). Large-eddy simulation of transonic flow over a bump. *International Journal of Heat and Fluid Flow*, **24**, 584–595.
Referenced on page: 3, 4, 13, 25, 26, 27, 94

SHIEH, C. & MORRIS, P. (2001). Comparison of two- and three-dimensional turbulent cavity flows. Conference paper 2001-0511, AIAA, Reno, NV, United States, 39th AIAA Aerospace Sciences Meeting and Exhibit.
Referenced on page: 8, 44

SMAGORINSKY, J. (1963). General circulation experiments with the primitive equations. *Mon. Weather Review*, **91**.
Referenced on page: 10

SPALART, P., DECK, S., SHUR, M., SQUIRES, K., STRELETS, M. & TRAVIN, A. (2006). A new version of Detached-Eddy Simulation, resistant to ambiguous grid densities. *Theoretical and Computational Fluid Dynamics*, **20**, 181–195.
Referenced on page: 41

SPALART, P.R. (1988). Direct simulation of a turbulent boundary layer up to Re_theta = 1410. *Journal of Fluid Mechanics Digital Archive*, **187**, 61–98.
Referenced on page: 11

SPALART, P.R. & WATMUFF, J.H. (1993). Experimental and numerical study of a turbulent boundary layer with pressure gradients. *Journal of Fluid Mechanics*, **249**, 337–371.
Referenced on page: 11

SPILLE, A. & KALTENBACH, H.J. (2001). Generation of turbulent inflow data with a prescribed shear-stress profile. *Third AFOSR Conference on DNS and LES*, **.**
Referenced on page: 13

SUPONITSKY, V., AVITAL, E. & GASTER, M. (2005). On three-dimensionality and control of incompressible cavity flow. *Physics of Fluids*, **17**.
Referenced on page: 8, 44

SWEBY, P. (1984). High resolution schemes using flux limiters for hyperbolic conservative laws. *SIAM Journal of Numerical Analysis*, **21**, 995–1011.
Referenced on page: 21, 21, 21, 22, 52, 94

TAM, C.K.W. & WEB, J.C. (1993). Dispertion-relation-preserving finite-difference schemes for computational acoustics. *Journal of Computational Physiscs*, **107**, 262–281.
Referenced on page: 105

TESSICINI, F., TEMMERMAN, L. & LESCHZINER, M.A. (2006). Approximate near-wall treatments based on zonal hybrid rans-les methods for les at high reynolds numbers. *International Journal of Heat and Fluid Flow*, **27**, 789–799.
Referenced on page: 49, 64

TOWNSEND, A.A. (1976). *The Structure of Turbulent Shear Flow*. Cambridge University Press, Cambridge, U.K., 2nd edn.
Referenced on page: 16

UK DEPARTMENT FOR TRANSPORT (2003). The future of Air Transport, White Paper and the Civil Aviation Bill. Tech. rep., UK Department for Transport.
Referenced on page: 1

VAN LEER, B., THOMAS, J., ROE, P. & NEWSOME, R. (1987). A comparison of numerical flux formulas for Euler and Navier-Stokes equation. In AIAA, ed., *AIAA 8th Computational Fluid Dynamics Conference*, 87-1104, 36–41.
Referenced on page: 20

VESELY, L. (2009). *Investigation of flow in the proximity of walls at very low Reynolds number using PIV measurement techniques*. Ph.D. thesis, Politecnico di Torino.
Referenced on page: 99

VON KÁRMÁN, T. (1930). T. mechanische aehnlichkeit und turbulenz. Tech. rep., Third international congress on applied mechanics, Stockholm, Sweden.
Referenced on page: 52, 53

WAGNER, C.A., HUTTL, T. & SAGAUT, P. (2007). *Large-eddy simulation for acoustics*. Cambridge University Press, United Kingdom.
Referenced on page: 11

WHITE, F. (1991). *Viscous fluid flow*. McGraw-Hill Series in Mechanical Engineering, 2nd edn.

Referenced on page: 32

WILCOX, D. (1981). Algorithm for rapid integration of turbulence model equations in parabolic regions. *AIAA Journal*, **19**, 248–251.

Referenced on page: 47

WILCOX, D. (1988). Reassesment of the scale determining equations for advanced turbulent models. *AIAA Journal*, **26**, 1299–1310.

Referenced on page: 47

WILCOX, D. (2002). *Turbulence modeling for CFD*. D C W Industries, 2nd edn.

Referenced on page: 17, 47

YAKHOT, V., ORSZAG, S., THANGAM, S., GATSKI, T. & SPEZIALE, C. (1992). Development of turbulence models for shear flows by a double expansion technique. *Physics of Fluids A*, **4**, 1510–1520.

Referenced on page: 11

YAO, H., COOPER, R. & RAGHUNATHAN, S. (2004). Numerical simulation of incompressible laminar flow over three-dimensional rectangular cavities. *Journal of Fluids Engineering*, **126**, 919–927.

Referenced on page: 8

YOSHIZAWA, A. (1986). Statistical theory for compressible shear flows with the application of subgrid modelling. *Physics of Fluids A*, **29**, 2152–2163.

Referenced on page: 16

YOU, D. & MOIN, P. (2007). A dynamic global-coefficient subgrid-scale eddy-viscosity model for large-eddy simulation in complex geometries. *Physics of Fluids*, **19**, 065110.

Referenced on page: 11

ZHANG, X., RONA, A. & EDWARDS, J. (1998). The effect of trailing edge geometry on cavity flow oscillation driven by a supersonic shear layer. *The Aeronautical Journal*,

102, 129–136.

Referenced on page: 3